REMOTE SENSING OF WASTEWATER CONTAMINATION IN COASTAL AREAS: A CASE STUDY OF CONCEIÇÃO LAGOON, BRAZIL
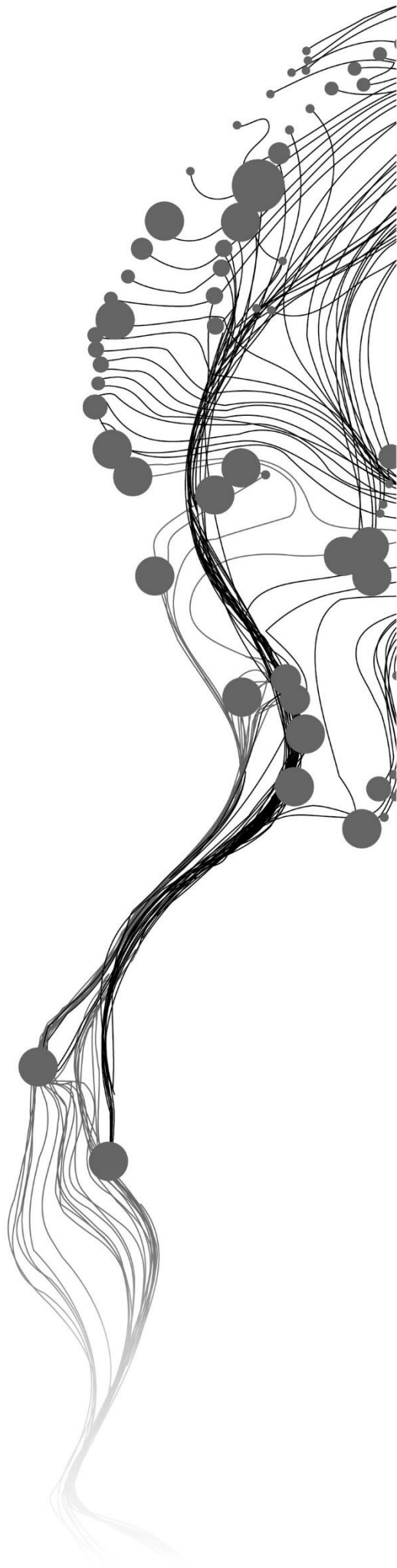
AMANDA DE LIZ ARCARI
July, 2022

SUPERVISORS:
Dr. Ir. S. Salama
Prof. Dr. D. Van der Wal

REMOTE SENSING OF WASTEWATER CONTAMINATION IN COASTAL AREAS: A CASE STUDY OF CONCEIÇÃO LAGOON, BRAZIL

AMANDA DE LIZ ARCARI
Enschede, The Netherlands, July, 2022

Thesis submitted to the Faculty of Geo-Information Science and Earth Observation of the University of Twente in partial fulfilment of the requirements for the degree of Master of Science in Geo-information Science and Earth Observation.
Specialization: Water Resources and Environmental Management

SUPERVISORS:
Dr. Ir. S. Salama
Prof. Dr. D. Van der Wal

ADVISOR
MSc. Juliana Tavora

THESIS ASSESSMENT BOARD:
Dr. Ir. R. Van der Velde (Chair)
Dr. L. Terres de Lima (External Examiner, LG Sonic)

ABSTRACT

One of the major sources of pollution affecting coastal water bodies in urbanized watersheds is related to poorly treated or untreated wastewater discharge. The excess of nutrients, organic matter and pathogens cause an overall deterioration of water quality and impair valuable ecosystem services. The detection of wastewater pollution is therefore essential for the sustainable management of coastal resources and remote sensing can provide the means for monitoring at extended spatial scales and high temporal frequencies.

This study investigated the utility of optical remote sensing in detecting wastewater spills in Conceição Lagoon, a coastal lagoon in Southern Brazil that suffers from recurrent problems of wastewater contamination. Inherent Optical Properties (IOPs) derived from Sentinel-2 MSI imagery using the 2SeaColor model were used to characterize a representative wastewater plume. Modal analysis was applied to capture the spatial dynamic of the plume with respect to the background water, whereas the temporal features were captured by temporal standardization. This combination allowed the formulation of a novel Wastewater Contamination Index (WCI).

The WCI consists of the standardized anomalies of a linear combination of IOPSs, namely: diffuse attenuation coefficient of photosynthesis available radiation, $k_d(\text{PAR})$ (a quasi-IOP), the absorption coefficient of phytoplankton green pigment Chlorophyll-a, $a_{chla}(440)$, the absorption coefficient of detritus and coloured dissolved organic matter, $a_{dg}(440)$, and backscattering of suspended particulate matter, $b_{b\,spm}(440)$. The weigths of the linear combination are constructed from the eigenvectors of the IOPs Spatial Principal Component Analysis (PCA) during a wastewater outfall event. Results showed that wastewater optical signal is mostly characterized by $b_{b\,spm}(440)$ and $k_d(\text{PAR})$, with a relative importance of approximately 40% each to the WCI. This can be associated to the elevated concentration of suspended solids in wastewater and its effect on water transparency. Despite dissolved organic matter being also characteristic of wastewater, $a_{dg}(440)$ showed a secondary role in the description of the wastewater plume, with a weight of 15%. The lowest influence on WCI came from $a_{chla}(440)$, with 8%. This was expected, as algal blooms would be a post-effect following nutrient enrichment from wastewater and depending on other environmental conditions.

The WCI was applied to 139 Sentinel-2 images from 2019 to 2021 to detect specific outfall events and examine their spatio-temporal patterns. With the aid of photographic records, meteorological, water quality and hydrodynamics data, it was possible to find agreement between high WCI values and four wastewater outfalls in Conceição Lagoon. The spatio-temporal analysis of WCI did not indicate significant recurrent patterns of wastewater pollution in the area, highlighting the irregular nature and unpredictability of wastewater outfalls.

TABLE OF CONTENTS

LIST OF FIGURES

LIST OF TABLES

1.   INTRODUCTION

Coastal environments are highly complex systems with distinct dynamics, high productivity, and rich biodiversity, providing thereby a wide range of valuable ecosystem services (Turner, 2015). Because of these services, coastal areas are historically associated with intense human occupation and, as a consequence, anthropogenic pressures and environmental degradation are often observed (Lopez y Royo et al., 2009). One of the major disturbances affecting coastal water bodies is related to poorly treated or untreated wastewater discharge (Fraschetti et al., 2006; Raj, 2013). This can be caused by irregular connections of sewage to the stormwater network, leaks and overflows from the sewerage system itself, or bad performance of the wastewater treatment plant and outfall pipe. The excess of organic matter and nutrients in wastewater that enters the aquatic systems can cause an increase in the trophic state, algal blooms, and eventually, oxygen depletion from their decay, resulting in an overall deterioration of water quality and ecological imbalance (El Mahrad et al., 2020). Untreated wastewater effluents can therefore negatively affect the chain of services and goods and could result in irreversible damage to marine ecosystems. Furthermore, climate change can contribute to the issue of wastewater discharge in coastal areas, as extreme rainfall events and sea-level rise are projected to increase in frequency and intensity in the coming decades (IPCC, 2018). This makes wastewater treatment plants (WWTP), typically located at low elevations such as coasts, more prone to flooding and overflows (Hummel et al., 2018). As a consequence, the exposure of coastal areas to wastewater contamination tends to escalate.

Conceição Lagoon, located in Florianópolis, southern Brazil, is a subtropical semi-enclosed coastal lagoon that is widely used by the local population for fishing, recreation, sports practice and is considered a major tourist attraction (Martini et al., 2006). Due to disordered urban sprawl and deficient sanitation, the water body has been subject to persistent nutrient and organic matter loading from sewage discharge, which has led to a process of eutrophication, with recurrent algal blooms and hypoxia/anoxia conditions (Cabral et al., 2019; Silva et al., 2017). This is a chronic situation with its characteristics and impacts studied by several researchers over the last years, who indicate the critical need for spatial-temporal monitoring of the water body (Cabral et al., 2019). Recent acute events, such as the rupture of the disposal pond of a WWTP in January 2021 and its severe consequences to the lagoon's ecosystem, have evidenced the urgency of integrated monitoring and management to prevent further damage and support recovery actions (Odreski et al., 2021).

The detection of wastewater plumes and their dispersion is of paramount importance for the sustainable management of coastal resources (Hafeez et al., 2019). Once it is accomplished, efforts can be efficiently invested in sealing the source, restoring affected areas, protecting vulnerable species, and preventing human intoxication by direct or indirect contact (i.e. bathing, swimming, ingestion of aquaculture products, etc.). Customarily, the monitoring of such pollution events is conducted with in-situ measurement campaigns, but these lack the combined spatial coverage, temporal resolution, and agility that are required for an adequate response in the intricate scenario that is observed in most coastal environments (Kratzer et al., 2014).

In this respect, satellite observation emerges as a necessary complement that provides near-real-time monitoring at extended spatial scales and high temporal frequencies, especially in the case of recently developed sensors (El Mahrad et al., 2020; Trinh et al., 2017). Satellite observations are moving towards operational monitoring of key spectral and biophysical features (Groom et al., 2019), which can be associated with water pollution. For example, reduced surface roughness caused by the presence of oil, or surfactants can be detected by active microwave sensors (radar), temperature differences are captured by thermal sensors, and variation of water-leaving reflectance caused by a higher concentration of chlorophyll-a, organic matter, or suspended material, can be tracked with optical sensors (Trinh et al., 2017). There have been a few studies on the detection of wastewater using data from different types of sensors, such as Synthetic Aperture Radar (SAR) (DiGiacomo et al., 2004) and optical multispectral images (Ayad et al., 2020; Bondur et al., 2020). Some other studies have made use of a combination of earth observation data for the indication of these pollution events. Marmorino et al. (2010) analysed airborne hyperspectral and infrared imagery to detect sewage discharge on the south coast of Florida, USA, where high levels of coloured dissolved organic matter (CDOM) and lower sea surface temperature (SST) were found to be associated with the effluent of wastewaters. In Southern California, USA, Gierach et al. (2017) assessed the capability of thermal, ocean color, and SAR products to detect wastewater plumes during an outfall diversion event. They found it to be related to lower SST and reduced radar backscattering. For another outfall diversion event at the same location, Trinh et al. (2017) could associate wastewater discharge to lower SST and increased chlorophyll-a concentration as derived from Landsat 8 sensors.

Studies on remote sensing of wastewater pollution conducted so far have mainly focused on the identification of the different spectral signals produced by wastewater plumes that can be captured by sensors (Bondur et al., 2020; Gierach et al., 2017; Trinh et al., 2017) and how these can be different from stormwater runoff and ambient waters (Ayad et al., 2020; DiGiacomo et al., 2004). Nonetheless, the combination of these spectral signals to constitute one single indicator of wastewater presence has not been explored yet. In this context, high spatial and temporal resolution imagery, coupled with hydro-optical models, dimensionality reduction methods and spatio-temporal analysis, provide an opportunity for the development of a method for more operational identification of wastewater plumes. Still, challenges arise from the reduced scale of the discharges, the strong influence of meteorological conditions, interaction with other local phenomena (i.e. seasonal phytoplankton blooms), and the optical complexity of waters (Gancheva et al., 2020).

In this study, the utility of optical remote sensing in detecting wastewater spills in Conceição Lagoon is investigated. Inherent Optical Properties (IOPs) derived from Sentinel-2 MSI imagery are used to characterize a representative wastewater plume in the area and derive the Wastewater Contamination Index (WCI). The WCI is intended to capture the spatial differences between wastewater plumes and ambient waters, and spot anomalous conditions across time. Spatio-temporal analysis further allows the assessment of potential recurring patterns of pollution in the area and characterize their drivers.

1.1. RESEARCH OBJECTIVES AND QUESTIONS

The main objective of this research is <u>to investigate the utility of optical remote sensing in detecting wastewater spills in Conceição Lagoon.</u>

The sub-objectives and their related research questions (RQ) are the following:

<u>Sub-Objective 1:</u>

To build a consistent time-series of inherent optical properties (IOPs) of Conceição Lagoon waters from Sentinel-2 imagery.

RQ1.1: How do the IOPs derived from in-situ reflectance spectra compare with the ones derived from Sentinel-2 imagery?

RQ1.2: How do the IOPs derived from in-situ reflectance spectra and Sentinel-2 imagery compare with in-situ concentration of water constituents?

<u>Sub-Objective 2:</u>

To formulate an index that optimally captures spatial and temporal dynamics of wastewater plumes.

RQ2.1: What is the optimal linear combination of IOPs that captures most of the spatial dynamics of a wastewater spill?

<u>Sub-Objective 3:</u>

To detect potential wastewater spills in Conceição Lagoon between 2019 and 2021.

RQ3.1: Can the WCI produce a distinguishable signal in association with wastewater spills in Conceição Lagoon?

<u>Sub-Objective 4:</u>

To identify the main spatio-temporal patterns of the WCI in Conceição Lagoon.

RQ 4.1: Where do we have hotspots of WCI throughout time?

RQ 4.2: Are the spatial-temporal patterns of the WCI related to other environmental variables?

2.   LITERATURE REVIEW

2.1.   REMOTE SENSING OF WATER POLLUTION

Remote sensing has the potential to provide comprehensive and frequent information on key spectral and biophysical features that could be associated with water pollution. For instance, reduced surface roughness caused by the presence of oil or surfactants can be detected by active microwave sensors (radar), temperature differences are captured by thermal sensors, and variation of water-leaving reflectance caused by a higher concentration of chlorophyll-a, organic matter, or suspended material, can be tracked with optical sensors (Trinh et al., 2017).

This setting has encouraged the development of a few studies using remote sensing for the detection of pollution hazards in coastal areas, which are mainly represented by contaminated urban stormwater runoff and discharge of treated or untreated wastewater. One of the oldest studies on the subject is from DiGiacomo et al. (2004), in which they used space-borne SAR data to detect stormwater runoff, wastewater and natural hydrocarbon seepage in the Southern California Bight, USA. According to the authors, these occurrences have in common the release of surfactants that damp the surface and reduce radar backscattering, appearing darker in the SAR imagery. Although the study identified 10 dB differences the between the plumes and the background of unpolluted waters, the shadow caused by natural phenomena forms a great challenge in radar observations (Krestenitis et al., 2019).

Other subsequent studies made use of optical remote sensing to identify stormwater and/or wastewater plumes. Nezlin and DiGiacomo (2005) were able to define a threshold for the normalized water-leaving radiation (nLw) at 555 nm (associated with suspended sediments concentration) derived from SeaWiFS to delineate stormwater plumes in southern California. Nezlin et al. (2008) found that nLw at wavelengths 531-551 nm from MODIS were the most adequate to identify stormwater plumes because its high concentrations of suspended material and CDOM provided a larger nLw difference between plume and no-plume. Bondur et al. (2018) used colour indices derived from optical multispectral images to detect anomalies that were caused by wastewater discharged from submerged outfalls in the Black Sea. In their study, the index defined as the product of the green and blue bands ($I = G * B$) was the most useful for identifying wastewater plumes, with higher values associated with wastewater. Ayad et al. (2020) were able to classify and differentiate stormwater and wastewater plumes based on the surface reflectance in the visible and NIR bands of RapidEye imagery using hierarchical cluster and principal component analysis. They observed that overall the highest reflectance values were seen in stormwater plumes, then wastewater followed with slightly lower spectra and clean water with the lowest reflectance. The researchers also verified that turbidity and CDOM were higher in stormwater, followed by wastewater and clean water.

There have also been studies that combined different remote sensing data for the indication of water pollution events. For instance, Marmorino et al. (2010) analysed airborne hyperspectral and infrared imagery to detect sewage discharge on the south coast of Florida, USA, where high levels of CDOM (obtained via empirical algorithm) and lower sea surface temperature (SST) were found to be associated with wastewater that was discharged via a submerged pipe. In southern California, USA, Trinh et al. (2017) used Landsat 8 OLI and TIRS sensors to monitor the effects of a wastewater diversion event in

2015, when secondary treated wastewater (no nutrient removal) was discharged through a shorter outfall pipe. During the diversion, a higher concentration of chlorophyll-a derived from OLI was observed as well as lower SST (around 1°C colder than ambient water), which the authors related to the surfacing of wastewater. For the other 2 outfall diversion events at the same location, Gierach et al. (2017) explored the advantages of a multi-sensor approach, using a combination of thermal, optical and SAR products to detect the surfacing wastewater plumes. In this case, lower SST and reduced radar backscattering were associated with the plumes. Optically derived chlorophyll-a concentration did not provide a detectable feature during the events, which could be associated with the short duration of the outfall, chlorination of the effluent, or strong dilution. This muffled response from chlorophyll-a was also observed by Seegers et al. (2017), who related it to a strong water column mixing detected using an autonomous underwater vehicle.

From a monitoring point of view, the creation of an index that summarizes the different remotely-sensed signals of water pollution could be especially useful for the identification of plumes, but this has not yet been explored in the literature.

2.2. SPATIO-TEMPORAL ANALYSIS OF EARTH-OBSERVATION DATA

Earth Observation (EO) products provide multitemporal geospatial data that can contribute to a better comprehension of a system's dynamics over space and time (Koehler and Kuenzer, 2020; Xia et al., 2018). Spatio-Temporal Analysis comprises the complex task of extracting the underlying patterns that could explain the spatial and temporal variability of the analysed feature with physical meaning and in an interpretable manner (Bueso et al., 2020).

One way of investigating spatio-temporal patterns is temporal decomposition, which has long been used for time-series analysis (West, 1997). It consists of separating the time-series into 3 components, namely the trend, the seasonality and the residuals (Kuiper, 1978). Several methods have been proposed to decompose time-series into its underlying components, which can be applied to spatio-temporal data in a pixel-by-pixel approach. The most simple approach to separate the trend is the Linear Trend Model, which finds a linear regression in a time-series via least-squares fitting. Other methods can be based on moving-averages to smooth the series, such as the X-11 (Shiskin et al., 1967), or local polynomial fitting (i.e. Seasonal-Trend Decomposition Procedure Based on Loess (STL) (Cleveland et al., 1990)).

Another approach for spatio-temporal analysis is a raster-cube decomposition, which derives at the same time spatial patterns and their associated temporal profiles (related to all pixels together, as opposed to pixel-by-pixel in temporal decomposition). Principal Component Analysis (PCA) (or Empirical Orthogonal Function (EOF)) is a raster-cube decomposition method commonly used to evaluate spatiotemporal variability (Liang et al., 2012). EOF and PCA are the same method, but the term EOF is commonly used when the variable has spatial and temporal components (Bierman et al., 2011). Some authors refer to this type of analysis with temporal component as an extended PCA, which can be in t-mode if images at different time steps are considered statistical variables, or s-mode when the statistical variables are the temporal profiles of each sample in space (pixel) (Machado-Machado et al., 2011).

PCA analysis has been largely used to investigate the dynamic modes of the process under study, especially in climatic and meteorological research (Hannachi et al., 2007; Roundy, 2015). For instance, studies have shown that the first PCA mode of global monthly sea surface temperature can be linked to the El Niño-Southern Oscillation (Tippett and L'Heureux, 2020). With the same objective of finding patterns, PCA has been expanded to many other fields, including ocean color. Navarro and Ruiz (2006) used PCA on SeaWiFS's weekly composite chlorophyll-a maps and detected the first mode as the seasonal pattern of phytoplankton blooms in the Gulf of Cadiz, which explained 20% of the variability. It should be noted that the spatial patterns do not necessarily represent any physical principle, and their association requires careful evaluation (Bjornsson and Venegas, 1997). In the study of Navarro and Ruiz (2006), they observed that the first spatial mode was in agreement with the climatology of chlorophyll-a in the area and that the expansion coefficient time series had alternating signals between spring-fall and summer-winter, therefore indicating the seasonal component. In addition, the investigation of correlation between the temporal coefficient and other environmental variables (i.e. tide, precipitation, wind) can indicate whether the identified patterns are influenced by them (Jawson and Niemann, 2007). As an example, the study by Normandin et al. (2019) showed that the main spatial pattern of SPM verified in the Gironde estuary is highly correlated to the tidal range and river discharge.

So far in the literature, neither PCA or temporal decomposition have been applied to time series of water color variables to investigate wastewater spatio-temporal patterns. Yet, such an analysis could further evidence whether there are recurring patterns of pollution in an area and what are the potential drivers of it.

3. STUDY AREA

Conceição Lagoon is a subtropical coastal lagoon located in Santa Catarina Island, in the municipality of Florianópolis, southern Brazil (Figure 1). The system is considered one of the main attractions in the region and provides a range of valuable ecosystem services (Lisboa et al., 2008; Silva et al., 2017). Being a natural nursery habitat for crustaceans, fish and molluscs, it is considered of great biotic importance, but also a source of income for local artisanal fishermen who exploit this resource (Lüchmann et al., 2008). The lagoon is also widely used for transportation, recreation and the practice of water sports, such as sailing, kitesurfing and canoeing. These characteristics attract many visitors and stimulate human occupation in the area, which at the same time exerts pressure on the ecosystem and demands preservation efforts to maintain the provision of services (Silva et al., 2017).
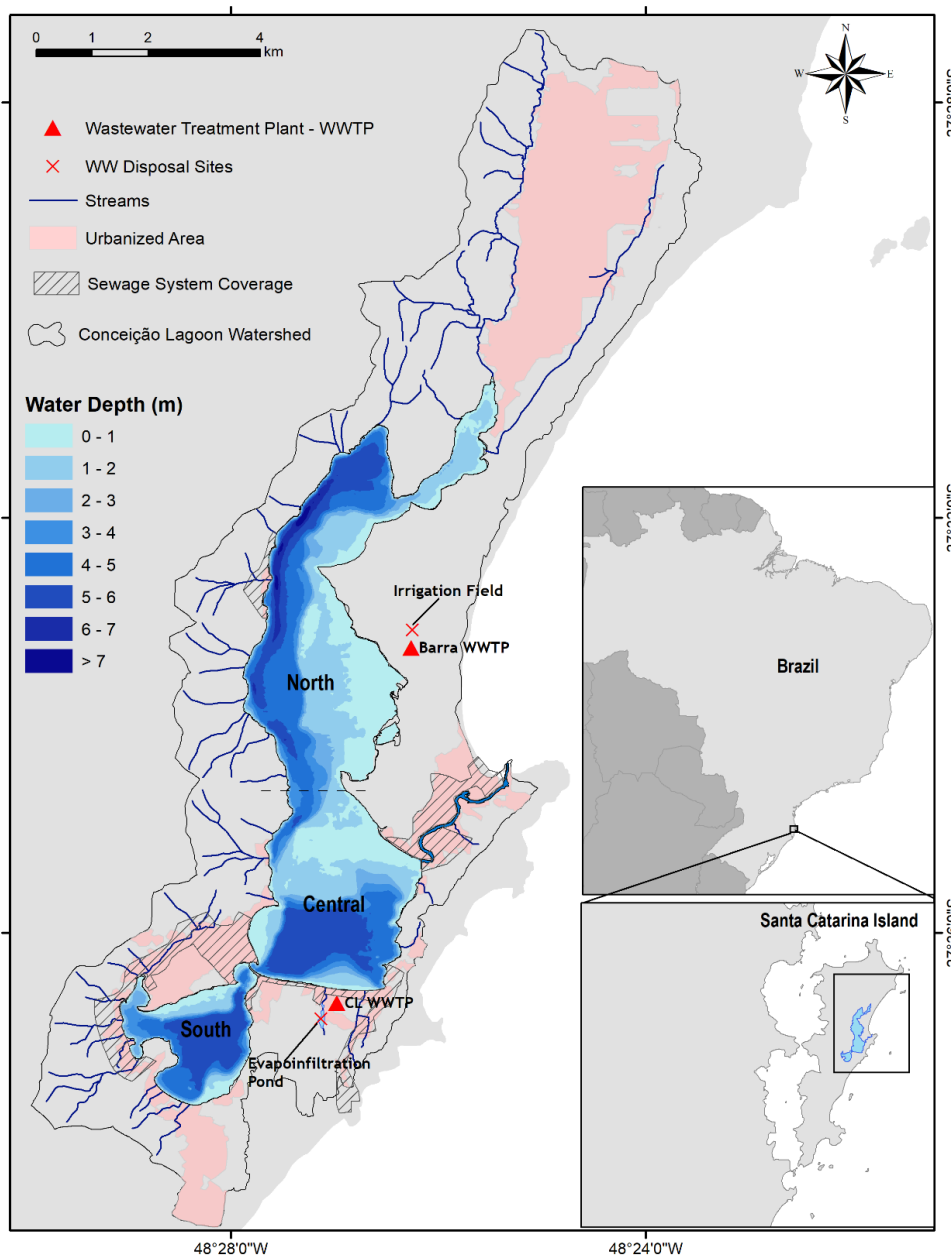
Figure 1: Location of Conceição Lagoon and main pollution sources

Conceição Lagoon ecosystem comprises a water surface area of 20.3 km² in an elongated form, which extends 13.4 km in the North-South direction, with heterogeneous bathymetry and bottom composition. Depths vary from less than 0.5 m in the eastern sandbanks to up to 8.6 m in the opposite margin. The shallower regions are also associated with a sandy substrate, while muddy sediment occurs where higher depths and river outlets are present (Porto Filho, 1993). According to these morphological features and water properties, the lagoon is traditionally divided into 3 subsystems: Northern, Central and Southern Lagoon (Fontes et al., 2010; Lisboa et al., 2008; Lüchmann et al., 2008; Martini et al., 2006). In the Central Lagoon, a meandering 2.8 km channel (Barra channel) solely connects the water body to the Atlantic Ocean, classifying it as a choked lagoon. This type of lagoon has a limited exchange with the ocean and resulting in a long residence time (Mahapatro et al., 2013). According to Silva et al. (2017), the lagoon's hydrodynamics respond primarily to meteorological forcings, especially wind, and hydrological conditions in the contributing watershed, with little to no tidal effects. These conditions increase the importance of controlling pollutant loads (CASAN, 2021).

The watershed that drains into Conceição Lagoon has an area of 61.8 km², with several small sub-watersheds of distinct characteristics. The western drainage area is delimited by high steep granitic slopes. To the east, sand deposits constitute a sedimentary coastal plain, while in the southeast a large dune field is present. Most of the area of the watershed is covered with natural vegetation. Nevertheless, around 15% of its area has been undergoing a disordered urbanization process over the last 30 years (Odreski et al., 2021), with a sharp increase in population density, which grew 93.2% between 2001 and 2015 (Silva et al., 2017). This situation has caused strong pressures on the lagoon's ecosystem, with a progressive decrease in water quality that compromises aquatic life, human health and economic activities. Drivers are mainly associated with sewage discharge, urban runoff and sediment loading due to the occupation of hillslopes (Martini et al., 2006). An important factor is the lack of a sewerage collection system for approximately 43% of the population of the basin (Odreski et al., 2021). The individualized solutions adopted by the unserviced buildings commonly present irregularities related to waterproofing and distance to groundwater level (Cabral et al., 2019). Where a sewage system is installed, recurrent issues relate to the overflowing of pumping stations and irregularities in the connections (Odreski et al., 2021). According to the municipality's inspection program, up until August 2021, 477 buildings in Conceição Lagoon sewer network had been identified with no or incomplete connection to the system or discharging effluents in the stormwater system, corresponding to 35% of the inspection sites.

As a result of these circumstances, frequent algae blooms and anoxic/hypoxic events have been observed in Conceição Lagoon over the last years, indicating a process of anthropic eutrophication (de Barros et al., 2017; Fontes et al., 2010; Silva et al., 2017). In May 2020 a large patch of scum was observed in the South Lagoon. Researchers identified the scum as decaying organic matter and biofilm formed by bacteria, diatoms, cyanobacteria and dinoflagellates, which was likely to be associated with wastewater discharge into the lagoon, considering the detection of high levels of thermotolerant coliforms and a leak in the sewage network (UFSC, 2020). The most recent, and possibly acute, event occurred on January 25th, 2021, with the rupture of an evapo-infiltration pond (EIP) that received the effluents from the Conceição Lagoon wastewater treatment plant. Due to a combination of intense rainfall and defective operation, the EIP burst and approximately 79 m³ of nutrient-rich sediment-water mixture entered Conceição Lagoon (CASAN, 2021). According to Odreski et al. (2021), the detected hypoxic conditions, harmful algae bloom and fish die-offs following the event could be a consequence of the synergistic effects caused by the incident and the historical eutrophication process taking place in the lagoon. The occurrence of such events in Conceição Lagoon highlights the need for efficient management actions, which could strongly benefit from a continuous monitoring system and detection of possible pollution sources.

4.   DATASETS

4.1.   SATELLITE IMAGE TIME-SERIES

Sentinel-2 MSI (S2-MSI) imagery from the European Space Agency's (ESA) was selected due to its high spatial and temporal resolution and radiometric quality, yielding recognized suitability for aquatic studies (Caballero et al., 2020). The combination of two polar-orbiting satellites (Sentinel-2 A and Sentinel 2-B) equipped with the MultiSpectral Instrument (MSI) provides multi-spectral images in the study area every 2-3 days with a spatial resolution of 10 m in the visible range (Table 1).

Table 1: Sentinel-2 mission band characteristics

Band	Description	Resolution	Central Wavelength
B1	Aerosols	60 meters	443.9nm (S2A) / 442.3nm (S2B)
B2	Blue	10 meters	496.6nm (S2A) / 492.1nm (S2B)
B3	Green	10 meters	560nm (S2A) / 559nm (S2B)
B4	Red	10 meters	664.5nm (S2A) / 665nm (S2B)
B5	Red Edge 1	20 meters	703.9nm (S2A) / 703.8nm (S2B)
B6	Red Edge 2	20 meters	740.2nm (S2A) / 739.1nm (S2B)
B7	Red Edge 3	20 meters	782.5nm (S2A) / 779.7nm (S2B)
B8	NIR	10 meters	835.1nm (S2A) / 833nm (S2B)
B8A	Red Edge 4	20 meters	864.8nm (S2A) / 864nm (S2B)
B9	Water vapor	60 meters	945nm (S2A) / 943.2nm (S2B)
B11	SWIR 1	20 meters	1613.7nm (S2A) / 1610.4nm (S2B)
B12	SWIR 2	20 meters	2202.4nm (S2A) / 2185.7nm (S2B)

Sentinel 2 Level-2A Products (i.e. surface reflectance), which are processed using sen2cor for atmospheric correction, were downloaded from the Copernicus Open Access Hub (https://scihub.copernicus.eu/). This product is only available for images from December 2018, therefore the period of analysis was defined as January 2019 to December 2021.

In total, 139 images acquired for the tile that covers the study area (T22JGQ) were selected to compose the Sentinel-2 time series. The condition for selection was the product's metadata cloud cover lower than 50%, with Conceição Lagoon completely or at least partially clear through visual inspection. The image distribution per month and year are presented in Figure 2. Every year the total number of images is consistent (42 - 49) and each month is represented by at least one image, except for October 2021.
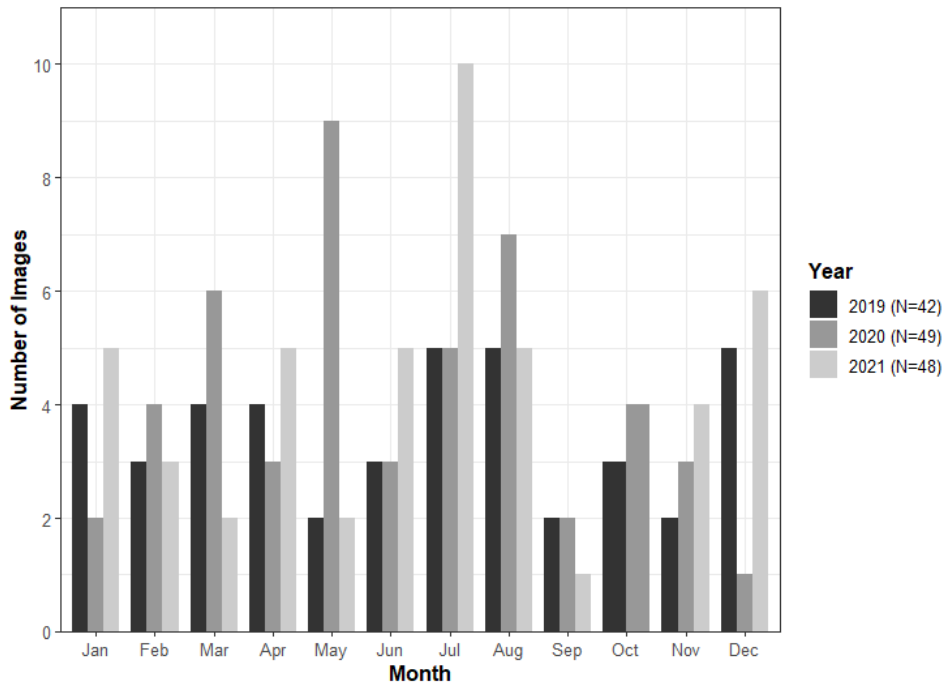
Figure 2: Selected Sentinel-2 images distribution per year and month

4.2.   FIELD MEASUREMENTS

Field measurements took place in December 2021 in Conceição Lagoon, comprising seven Field Campaigns (FC), of which three coincided with satellite's overpass and mostly clear sky (see details in Table 2). In total, 67 combined radiometric and water quality (WQ) measurements were taken, of which 11 could be matched up with Sentinel-2 images (9 points from FC 04 and 2 points from FC 06) and 8 points from FC 07 could be matched up with Landsat 8 images.

Table 2: Field campaigns details

FC	Date	Sampling Time (UTC -3)	Duration (hour)	Satellite Overpass (UTC -3)	Points Sampled	Sky Condition
01	02/12/2021	9:38 – 11:15	01:37	S2 B – 10:12	9 (P1 to P9)	Overcast
02	03/12/2021	9:47 – 10:41	00:54	L8 – 10:05	6 (P10 to P15)	Overcast
03	07/12/2021	9:38 – 12:21	02:43	S2 A – 10:12	15 (P1 to P15)	Partly Cloudy
04	10/12/2021	9:25 – 10:36	01:11	S2 A – 10:22	9 (P1 to P9)	Mostly Clear
05	13/12/2021	11:32 – 12:49	01:17	-	6 (P10 to P15)	Mostly Clear
06	17/12/2021	9:33 – 10:43	01:10	S2 A – 10:12	7 (P1 to P7)	Mostly Clear
07	28/12/2021	9:34 – 11:32	01:58	L8 – 10:05	15 (P15 to P1)	Mostly Clear

Note: S2 A/B denotes Sentinel-2 A and B satellites; L8 denotes Landsat 8 satellite

There were in total 15 sampling points, for which the locations are presented in Figure 3. These were defined based on the previous work of Horn (2021), who conducted a geostatistical analysis for the definition of homogeneous reflectance areas at different bathymetry intervals and established 60 points with the most variability in reflectance over time within the visible bands of Sentinel-2 MSI. Considering that the Central and South Lagoon have more anthropic pressure and are more prone to wastewater discharge, points were selected only in that area for this study and a few others were included to form transects.
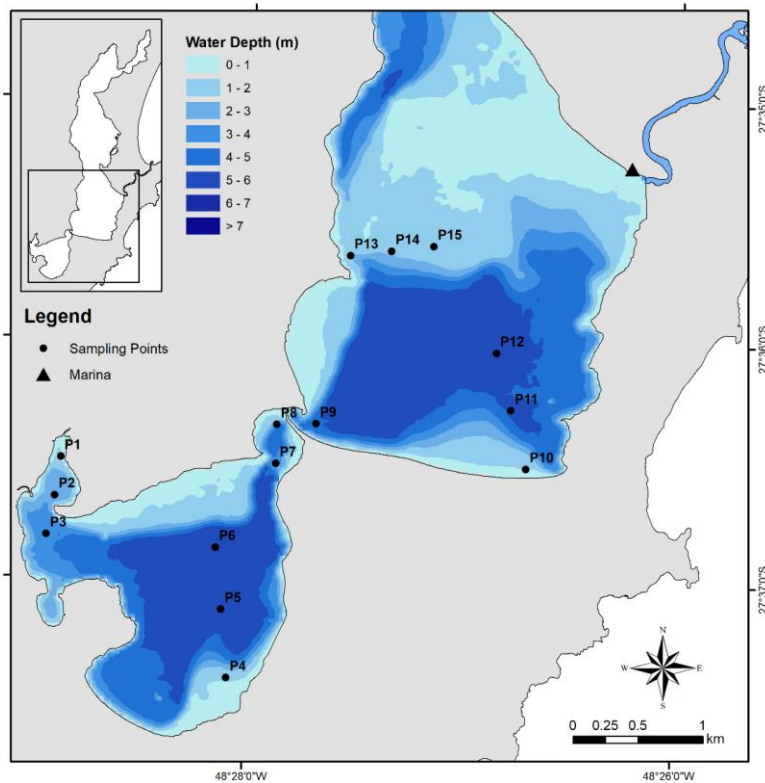
Figure 3: Sampling points for field measurements and water depth

The parameters measured in the field campaigns, the type of measurement, the method/equipment used and their objective are presented in Table 3.

Table 3: Parameters measured in field campaigns

Parameter	Type	Method/Equipment	Objective
Sky-sun downwelling irradiance - E_d	Radiometric In-situ	Hyperspectral radiometer - TriOS RAMSES-ACC-VIS	Characterize AOPs;
Water leaving upwelling radiance - L_w	Radiometric In-situ	Hyperspectral radiometer - TriOS RAMSES-ARC	Validate orbital optical remote sensing products; Calibrate hydro-optical model.
CDOM concentration	WQ In-situ	Fluorometer – TriOS microFlu	Calibrate and Validate the hydro-optical model.
Chlorophyll-a concentration	WQ Laboratory Analysis	Labs 1 and 2: Spectrophotometry following SMWW 22 10200 H	
SPM concentration	WQ Laboratory Analysis	Labs 1 and 2: Total Suspended Solids Dried from 103 to 105 °C following SMWW 2540 D	
Thermotolerant coliforms	WQ Laboratory Analysis	Lab 1: Multiple tube fermentation following SMWW 9221 E Lab 2: Enzyme substrate following SMWW 9223 B	Indicate possible faecal contamination.
Temperature	WQ In-situ	CTD – SonTek CastAway-CTD	Characterization of general physical conditions
Salinity	WQ In-situ		

Note: SMWW denotes the Standard Methods for the Examination of Water & Wastewater from the American Public Health Association

The sampling logistics involved the use of a motorized boat as a means of transportation, which was harboured in a Marina located at the entrance of the Barra Channel (see Figure 3). The general strategy was alternating between starting at P1 in the South Lagoon and starting at P10 in Central Lagoon, aiming to cover as many points as possible during the available time (maximum 1h before and after the satellite overpass).

At each sampling point, the downwelling irradiance (E_d) and water-leaving upwelling radiance (L_w) signals were recorded simultaneously at least 3 consecutive times together with the CDOM measurement (see the layout in Figure 4). The recordings are calibrated automatically in the software of the equipment (MSDA_XE) using the calibration files provided by the manufacturer. For the other WQ In-Situ measurements, the CTD device (vertical profiler) was deployed from the boat. For the parameters that required laboratory analysis, water samples were collected by the researcher and analysed by accredited local laboratories (hereby called Lab 1 and Lab 2):

- Lab 1 (FC 01 to 06): QMC Saneamento Ltda. - http://www.qmcsaneamento.com.br/

- Lab 2 (FC 07): Acquaplant Química do Brasil Ltda. - https://www.acquaplant.com.br/

A more detailed description of the sampling procedures is presented in APPENDIX A – FIELDWORK SAMPLING PROCEDURES.

Pre-processing of the radiometric data included the interpolation of each E_d and L_w spectra for 1 nm interval (originally 3.3 nm), followed by Data Quality Control procedures. This indicated likely contamination by sunglint of most of the L_w spectra. Therefore, for each sampled point, the lowest L_w and corresponding E_d were used to calculate the remote sensing reflectance R_{rs} ($R_{rs} = L_w/E_d$) and a flagging system based on a feature on the oxygen absorption band (760 nm) was used to discard the spectra that were still likely contaminated, leaving us with 34 of the original 67 spectra to use. All of this is described in detail in APPENDIX D – FIELD DATA QUALITY CONTROL.

The compiled results of the water quality measurements and characterization of the overall conditions observed during fieldwork are presented in APPENDIX C – OVERALL CONDITIONS DURING FIELDWOR. The quality of these measurements was also evaluated (see APPENDIX D – FIELD DATA QUALITY CONTROL). This indicated that the results of the two laboratories' analyses were incompatible and that the ones from Lab 1 were more consistent with other studies in the area. We, therefore, excluded the results of Lab 2 from the study.
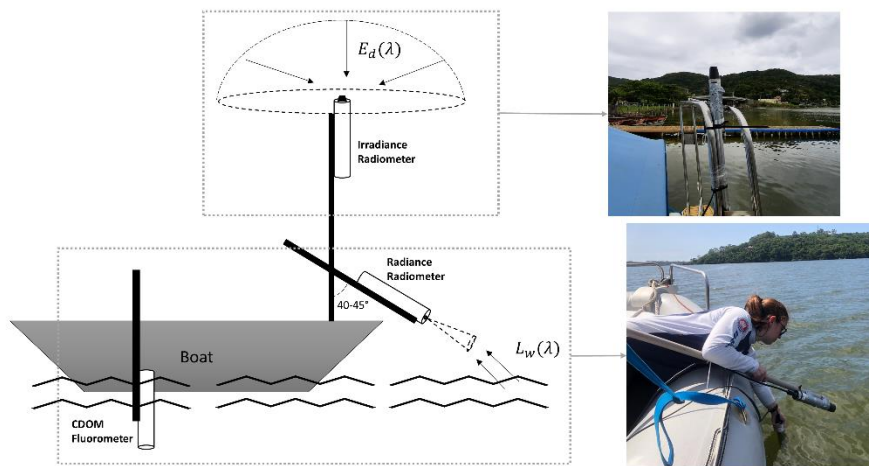
Figure 4: Layout configuration for radiometric and fluorometer measurements

4.3. COMPLEMENTARY DATASETS

4.3.1. Meteorological Data

To investigate the relation between wastewater events and other environmental variables in Conceição Lagoon, meteorological data from a weather station were used. The weather station is from the National Institute of Meteorology (INMET) and is located approximately 15 km from the lagoon (Station Code: A806). Hourly measurements of precipitation, wind direction and wind speed were obtained from INMET's website (https://portal.inmet.gov.br/dadoshistoricos) for the period between January 2019 and December 2021.

4.3.2. Conceição Lagoon Characteristics

The Maritime Hydraulics Laboratory of the Federal University of Santa Catarina (LahiMAR/UFSC) has conducted several studies of hydraulic, hydrological and water quality conditions in Conceição Lagoon for more than 15 years. Their outputs, mainly in the form of MSc Thesis, have been used as references in this study and are detailed in Table 4.

Table 4: Details of LahiMAR studies used as references for Conceição Lagoon Characteristics

Year	Type	Title	Author
2021	MSc	Characterization of the behavior of chlorophyll-a concentration in a coastal lagoon using remote sensing bio-optical models	(Horn, 2021)
2016	MSc	Space-time analysis of the trophic state of a subtropical coastal lagoon: Lagoa da Conceição, Florianópolis, Santa Catarina	(Silva, 2016)
2013	MSc	Numerical Analysis of the Influence of River and Anthropic Inputs on Residual Hydrodynamics and the Water Quality of Conceição Lagoon, Florianópolis/SC	(Silva, 2013)
2012	MSc	Hydrological Influence in the Hydrodynamic Processes of Conceição Lagoon, Florianópolis/SC	(Odreski, 2012)

4.3.3. Photographic and Video Recordings

The local community of Conceição Lagoon is highly active and has channels for sharing photographic and video recordings of anomalous conditions observed in the Lagoon. These records were shared by a local leader and were used in this study to support analysis.

5. RESEARCH METHODS

The methodology conducted in the research is summarized in the form of a flowchart in Figure 5. The main blocks of processes in the methodology, which are highlighted and numbered, correspond to each of the research sub-objectives and are described in this section.
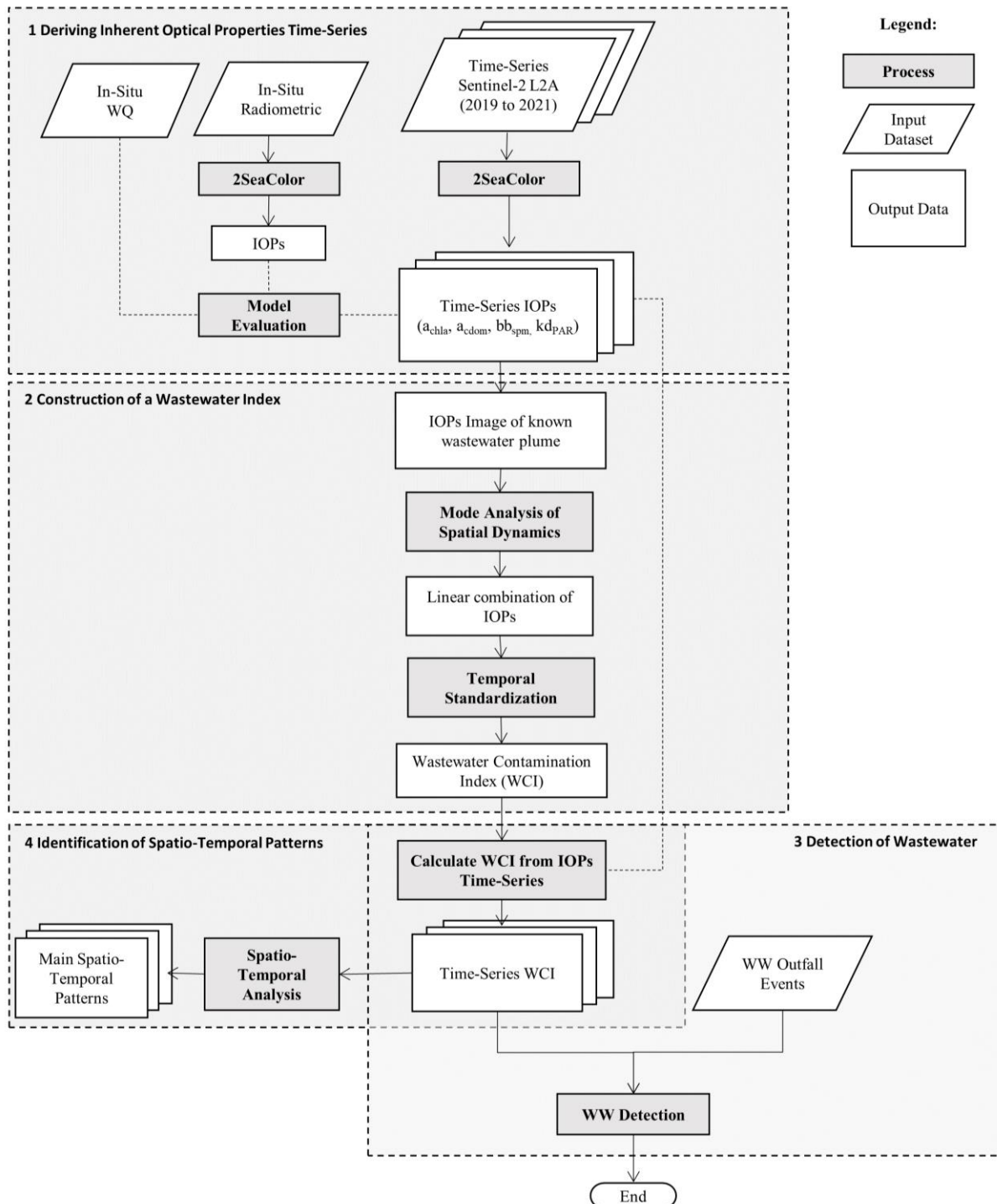
Figure 5: Flowchart summarizing the research methodology

5.1.   DERIVING INHERENT OPTICAL PROPERTIES

Hydro-optical models are algorithms developed to retrieve Inherent Optical Properties (IOPs) from Apparent Optical Properties (AOPs), which are composed by:

1- Forward model (that describes the AOP in terms of IOP);

2- Parametrization (that minimizes the number of IOPs by modelling their spectral response);

3- An inversion scheme (that derives IOP from AOP).

In this research, the analytical 2SeaColor model (Salama and Verhoef, 2015) is used to derive absorption by chlorophyll-a (a_{chla}), absorption by coloured dissolved organic matter and non-algal particles (a_{dg}), backscattering by suspended particulate matter (bb_{spm}) and diffuse attenuation coefficients in Conceição Lagoon from Sentinel-2 surface reflectance time-series (2019-2021) and remote sensing reflectance measured in-situ during Fieldwork.

The 2SeaColor simulates light interactions within water bodies in the visible part of the electromagnetic spectrum by analytically solving the two-stream radiative transfer equations, including the three radiation components: downwelling direct and diffuse fluxes and upwelling diffuse flux. Parametrization and an inversion scheme are used to derive the water column IOPs, which have been shown to provide accurate results in coastal turbid waters (Arabi et al., 2018, 2016).

The two-stream approach is an approximation of the radiative transfer theory that considers two discrete directions for radiant flux. A schematization of how this would apply to an infinitely deep water column is presented in Figure 6.
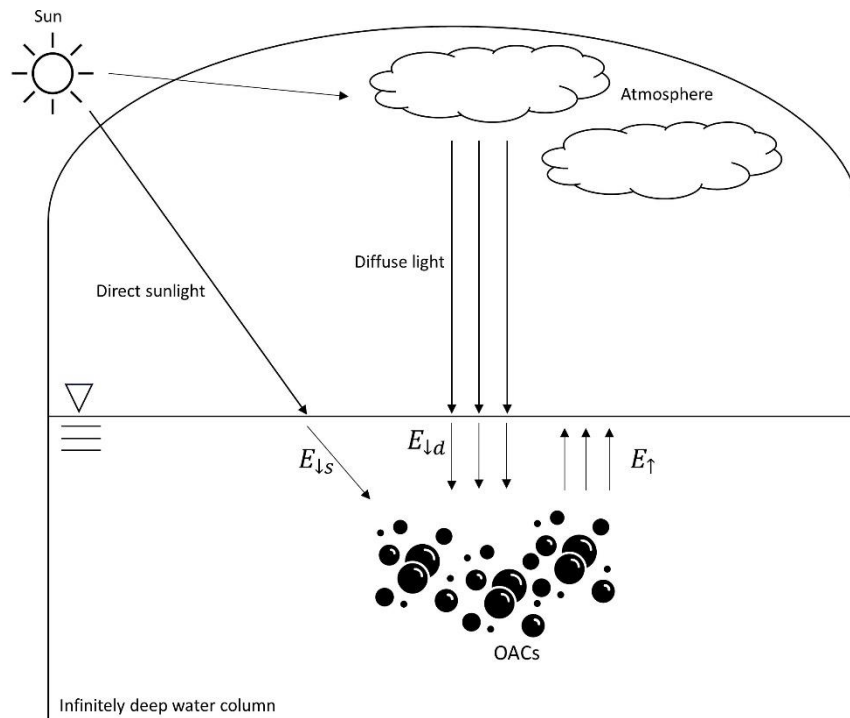
Figure 6: Representation of the 2 streams approximation for an infinitely deep water column

Based on Salama and Verhoef (2015), right below the water surface, we have the downwelling direct solar flux ($E_{\downarrow S}$), the downwelling diffuse flux ($E_{\downarrow D}$), and the upwelling flux ($E_{\uparrow}$). The total downwelling flux would then be:

$$E_{\downarrow} = E_{\downarrow S} + E_{\downarrow D} = (1 - f)E_{\downarrow} + fE_{\downarrow} \qquad\qquad 1$$

Where f is the fraction of diffuse light.

The total upwelling flux ($E_{\uparrow}$), on the other hand, depends on how $E_{\downarrow S}$ and $E_{\downarrow D}$ interact with the water molecules and the optically active constituents (OACs) by absorption and backscattering. For diffuse light, this interaction is represented by the bi-hemispherical reflectance for a semi-infinite medium (r_{∞}), which is given by the Kubelka Munk equation:

$$r_{\infty} = \frac{x}{1 + x + \sqrt{1 + 2x}} \qquad\qquad 2$$

Where x is the ratio between backscattering (b_b) and absorption (a) coefficients: $x = b_b/a$.

For direct sunlight, Salama and Verhoef (2015) propose the directional-hemispherical reflectance of the semi-infinite medium (r_{sd}^{∞}), which they solved as the following:

$$r_{sd}^{\infty} = \frac{\sqrt{1 + 2x} - 1}{\sqrt{1 + 2x} + 2\mu_w} \qquad\qquad 3$$

Where μ_w is the cosine of the solar zenith angle beneath the water surface.

The total upwelling flux, therefore, can be represented by:

$$E_{\uparrow} = r_{\infty}fE_{\downarrow} + r_{sd}^{\infty}(1 - f)E_{\downarrow} \qquad\qquad 4$$

And the irradiance reflectance just beneath the water surface (R_{∞}) is given as:

$$R_{\infty} = \frac{E_{\uparrow}}{E_{\downarrow}} = r_{\infty}f + r_{sd}^{\infty}(1 - f) \qquad\qquad 5$$

Ultimately, we can convert it to the above surface remote sensing reflectance (R_{rs}) considering the differences between the two media (air and water), which constitutes the forward model:

$$R_{rs} = \frac{t(a,w)t(w,a)}{n_w{}^2[1 - r(w,a)R_{\infty}]} \times \frac{R_{\infty}}{Q} \qquad\qquad 6$$

Where Q is the radiance to irradiance conversion factor, n_w is the index of refraction of water, $t(a,w)$ and $t(w,a)$ are respectively the air-to-water and water-to-air transmittances and $r(w,a)$ is the water-to-air reflectance.

By inverting the forward model we go from remote sensing reflectance to inherent optical properties (IOPs), in this case, the total backscattering (b_b) and absorption (a) coefficients.

These represent the bulk IOPs of the water column and result from the sum of the properties of each optically active constituent Mobley (1994):

$$a\,(\lambda) = a_w(\lambda) + a_{chla}(\lambda) + a_{dg}(\lambda) \qquad\qquad 7$$

$$b_b(\lambda) = b_{b_w}(\lambda) + b_{b\,spm}(\lambda) \qquad\qquad 8$$

Where a denotes absorption coefficient, b_b is the backscattering coefficient and the subscripts w, $chla$, dg and spm correspond respectively to water, chlorophyll-a, detritus + coloured dissolved organic matter and suspended particulate matter.

To allow the retrieval of the IOPs of interest, the following parametrizations based on Lee et al. (1999), Kirk (1994) and Kopelevich (1983) are used:

$$a_{chla}(\lambda) = (a_0(\lambda) + a_1(\lambda) \ln[a_{chla}(440)]) \, a_{chla}(440) \qquad\qquad 9$$

$$a_{dg}(\lambda) = a_{dg}(\lambda_0)e^{-S(\lambda-\lambda_0)} \qquad\qquad 10$$

$$b_{b\,spm}(\lambda) = b_{b\,spm}(\lambda_0)\left(\frac{\lambda_0}{\lambda}\right)^Y \qquad\qquad 11$$

Where a_0 and a_1 are parameters given by Lee et al. (1999), S is the spectral slope of a_{dg} and Y is the power law for $b_{b\,spm}$, for which initial values are given based on literature.

The diffuse attenuation coefficient k_d is calculated analytically from the derived IOPs (Salama and Verhoef, 2015):

$$k_d(\lambda) = \frac{((k - s')E_{\downarrow S} + \alpha E_{\downarrow D} - \sigma E_\uparrow}{E_\downarrow} \qquad\qquad 12$$

Where k, s', α and σ are the coefficients that represent extinction from the different irradiance components (more details in Salama and Verhoef (2015))

A summary of the equations and parametrizations to be used within the 2SeaColor model is presented in Table 5.

Table 5: Summary of equations and parametrizations for 2SeaColor model

Variable	Parametrization	Reference
Above-surface remote sensing reflectance	$R_{rs} = \dfrac{t(a,w)t(w,a)}{n_w{}^2[1 - r(w,a)R_\infty]} \times \dfrac{R_\infty}{Q}$	(Mobley, 1994)
Irradiance reflectance beneath the surface	$R_\infty = r_\infty f + r_{sd}^\infty (1 - f)$	(Salama and Verhoef, 2015)
Bi-hemispherical reflectance for a semi-infinite medium	$r_\infty = \dfrac{x}{1 + x + \sqrt{1 + 2x}}$	(Salama and Verhoef, 2015)
Directional-hemispherical reflectance of the semi-infinite medium	$r_{sd}^\infty = \dfrac{\sqrt{1 + 2x} - 1}{\sqrt{1 + 2x} + 2\mu_w}$	(Salama and Verhoef, 2015)
Backscattering to absorption ratio	$x = b_b/a$	(Salama and Verhoef, 2015)
Total absorption coefficient	$a(\lambda) = a_w(\lambda) + a_{chla}(\lambda) + a_{dg}(\lambda)$	(Mobley, 1994)
Total backscattering coefficient	$b_b(\lambda) = b_{b_w}(\lambda) + b_{b\,spm}(\lambda)$	(Mobley, 1994)
Water molecules absorption	$a_w(\lambda)$	(Mobley, 1994)
Chla absorption	$a_{chla}(\lambda) = (a_0(\lambda) + a_1(\lambda)\ln[a_{chla}(440)])\, a_{chla}(440)$	(Lee et al., 1999)
CDOM + NAP absorption	$a_{dg}(\lambda) = a_{dg}(\lambda_0)e^{-S(\lambda - \lambda_0)}$	(Kirk, 1994)
Water molecules backscattering	$b_{b_w}(\lambda)$	(Mobley, 1994)
SPM backscattering	$b_{b\,spm}(\lambda) = b_{b\,spm}(\lambda_0)\left(\dfrac{\lambda_0}{\lambda}\right)^Y$	(Kopelevich, 1983)
Diffuse attenuation coefficient	$k_d(\lambda) = \dfrac{((k - s')E_{\downarrow S} + \alpha E_{\downarrow D} - \sigma E_\uparrow}{E_\downarrow}$	(Salama and Verhoef, 2015)

The 2SeaColor inversion of Sentinel-2 Level-2A images derives the following variables:

- $k_d(443)$ (Band 1)
- $k_d(490)$ (Band 2)
- $k_d(560)$ (Band 3)
- $k_d(665)$ (Band 4)
- $k_d(705)$ (Band 5)
- $k_d(740)$ (Band 6)
- $k_d(783)$ (Band 7)
- $k_d(842)$ (Band 8)
- $a_{chla}(440)$ (Band 9)
- $a_{dg}(440)$ (Band 10)
- $b_{b\,spm}(440)$ (Band 11)
- S (Band 12)
- Y (Band 13)

To evaluate the agreement between the model retrievals on images and in-situ spectra, their matched-up IOPs $(a_{chla}(440), a_{dg}(440), b_{b\,spm}(440))$ were compared via type 2 regression. The values for the images were extracted considering the average of a 3x3 pixel window. The goodness-of-fit measures used for evaluation were the slope and intercept of the regression line.

To compare the IOPs derived by the model and concentration of water quality variables, a type 1 regression was conducted relating the IOPs (from in-situ and images) and the water quality in-situ measurements.

The correlation was assessed for the following pairs of variables:

- $a_{chla}(440)$ Vs. chlorophyll-a concentration
- $a_{dg}(440)$ Vs. CDOM concentration
- $b_{b\,spm}(440)$ Vs. SPM concentration

5.2.   FORMULATION OF A WASTEWATER INDEX

The light attenuation caused by the presence of wastewater plumes was assessed to formulate a Wastewater Index (WCI). One image capturing a wastewater outfall in Conceição Lagoon was selected as a reference to investigate the main optical properties that could indicate wastewater. This event was selected due to its large proportion (79 m³) and the presence of a persistent plume that was identifiable from a natural-color image of the 8th of February 2021 (Figure 7). An assumption is made that the signals associated with the plume of this specific event would be representative of other wastewater plumes in the area. The following sections describe the steps to reach the final formulation of the index.

5.2.1.   Band Subset: Selection of IOPs

The IOPs included in this analysis were chosen considering their potential indication of wastewater:

- $a_{dg}(440)$:   higher CDOM has been associated with wastewater plumes (Ayad et al., 2020; Marmorino et al., 2010; Nezlin et al., 2008).

- $b_{b\,spm}(440)$:   higher SPM has been associated with wastewater plumes (Ayad et al., 2020; Nezlin et al., 2008; Nezlin and DiGiacomo, 2005).

- $a_{chla}(440)$:   higher chlorophyll-a has been observed following a wastewater outfall (Trinh et al., 2017). Note that this would probably be the result of after-effect algae bloom and its occurrence depends on other environmental conditions, such as temperature, light availability and column mixing (Caballero et al., 2020).

- $k_{d\,PAR}$:   is a quasi-IOP (Yu et al., 2016) that represents the photosynthetically active radiation (PAR) penetration in the water column and is a function of both bulk IOPs and illumination conditions. It has not been reported in the literature as being directly associated with wastewater, but it was included due to its relation with the water column biogeochemistry (Salama and Verhoef, 2015).

Derived values of $a_{chla}(440)$, $a_{dg}(440)$ and $b_{b\,spm}(440)$ are already given as output raster bands from the 2SeaColor processing. $k_{d\,PAR}$ is calculated as the discrete summation of values of k_d from the visible bands of Sentinel-2 MSI (B1 to B5) over the spectral interval:

$$k_{d\,PAR} = \frac{\sum_{i=1}^{n} k_{d_i}\,\lambda_i}{\sum_{i=1}^{n} \lambda_i}$$ 13

Where λ_i is the spectral interval covered by the band i and n is the total number of bands (5 in this case).

An Interactive Data Language (IDL) routine coupled with ENVI software was used to:
- Get all the 139 2SeaColor output rasters
- Calculate $k_{d\,PAR}$ for each raster
- Save new rasters with only the bands of interest: $k_{d\,PAR}$, $a_{chla}(440)$, $a_{dg}(440)$ and $b_{b\,spm}(440)$.

5.2.2.   Spatial Subset

The next step was to subset the rasters to an area of interest (AOI) where the wastewater plume was observed on the image of February 8th 2021. The subset was also performed via IDL/ENVI routine, defining the AOI as a rectangle with approximately 0.9 by 0.4 km, avoiding optically shallow waters (Figure 7).
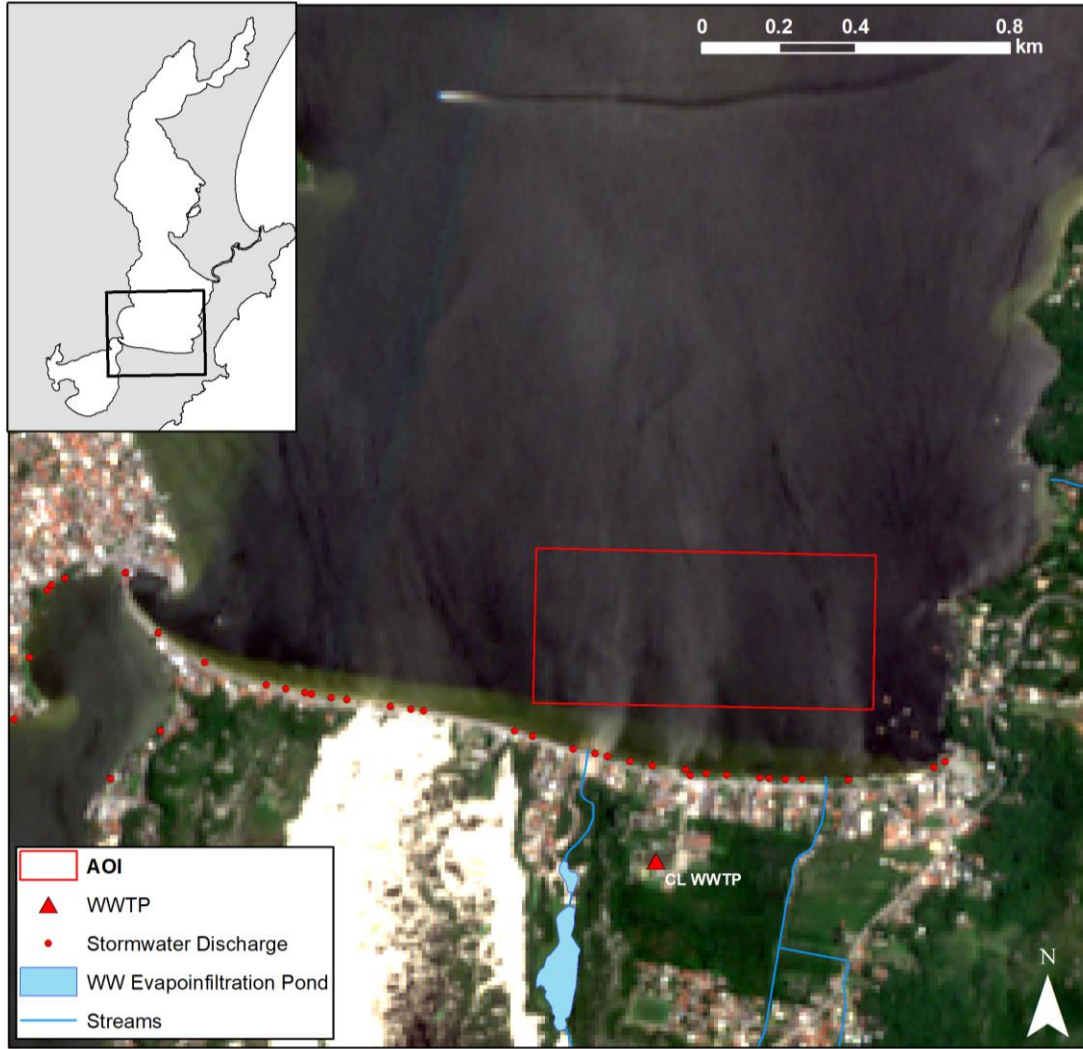
Figure 7: Sentinel-2 Image of 2021-02-08 with a visible wastewater plume coming from the area of the EIP burst and the Area of Interest (AOI) determined for the Spatial Subset

5.2.3. Principal Component Analysis (PCA)

A Principal Component Analysis (PCA) was performed on the subsets of the IOPs rasters. The aim was to reduce the dimensionality of the data and find a linear combination of IOPs that best captured the differences between wastewater plume and the background. PCA is a widely used technique for data compression, and its applicability in remote sensing to derive indices that synthesize the effects of multiple indicators has been demonstrated (Guo et al., 2020; Hu and Xu, 2019; Ingebritsen and Lyon, 1985; Yu et al., 2021). According to Hu and Xu (2019), the formulation of indices by PCA is an unbiased method that can objectively provide weights to each indicator in such a way that the index best explains the data variation. Furthermore, Ayad et al. (2020) have shown that PCA of reflectance values was able to distinguish between stormwater, wastewater and clean water in Southern California coast.

The classic approach of PCA is based on the mathematical technique of Eigen-decomposition of the covariance matrix. Taking a centred matrix $\overline{\mathbf{A}}(\boldsymbol{m} \times \boldsymbol{n})$, the covariance matrix is calculated as:

$$\mathbf{COV} = \frac{\overline{\mathbf{A}}^{\mathrm{T}} \times \overline{\mathbf{A}}}{n-1} \tag{14}$$

Where **COV** is an $n \times n$ symmetric matrix. Eigenanalysis suggests that any symmetric matrix can be decomposed as:

$$\mathbf{COV} \times \mathbf{V} = \mathbf{L} \times \mathbf{V} \qquad\qquad 15$$

Where **V** is an $n \times n$ matrix with orthogonal Eigenvectors as columns that give the direction of transformation: $\mathbf{V} = \begin{bmatrix} v_{11} & \cdots & v_{1n} \\ \vdots & \ddots & \vdots \\ v_{n1} & \cdots & v_{nn} \end{bmatrix}$,

And **L** is an $n \times n$ diagonal matrix of Eigenvalues: $\mathbf{L} = \begin{bmatrix} \lambda_{11} & \cdots & 0 \\ \vdots & \ddots & \vdots \\ 0 & \cdots & \lambda_{nn} \end{bmatrix}$

The projection of the centred matrix $\overline{\mathbf{A}}$ onto the orthogonal matrix **V** gives the Principal Components (PC) matrix:

$$\mathbf{PC} = \overline{\mathbf{A}} \times \mathbf{V} \qquad\qquad 16$$

Each column of PC is a Principal Component, each Eigenvector (column of **V**) associated with a PC gives the direction of transformation of the data, and their corresponding Eigenvalue λ gives a quantitative assessment of the explained variance:

$$\% \, \text{Var. Explained PC}_i = \frac{\lambda_i}{\sum_{k=1}^{n} \lambda_k} \times 100 \qquad\qquad 17$$

The PCs are organized in order of variance explained, with the first PC, transformed by the first Eigenvector, being the one that contains most of the information in the dataset.

In this analysis, the PCA is conducted on single images with multiple variables (IOPs), and the rasters can be represented by the following matrix:

$$\mathbf{A} = \begin{bmatrix} k_{d\,PAR_1} & a_{chla_1} & a_{dg_1} & b_{b\,spm_1} \\ \vdots & \vdots & \vdots & \vdots \\ k_{d\,PAR_m} & a_{chla_m} & a_{dg_m} & b_{b\,spm_m} \end{bmatrix}$$

Where $n = 4$ and m represents the reshaped 2D image with k rows and i columns ($m = k \times i$).

The first PC of each raster is given by:

$$PC1 = v_{11} . \overline{k_{d\,PAR}} + v_{12} . \overline{a_{chla}} + v_{13} . \overline{a_{dg}} + v_{14} . \overline{b_{b\,spm}} \qquad\qquad 18$$

The first Eigenvectors obtained for each raster ($v_{11}, v_{12}, v_{13}, v_{14}$) were extracted for further analysis. This procedure was conducted in IDL for all the subsetted rasters in the time series to allow comparison between natural conditions and when the plume was present.

5.2.4. Eigenvectors Analysis

The next step was analysing the first Eigenvectors obtained for each of the rasters to assess whether the one associated with the plume was distinct from the others. For this, an approach based on the Spectral Angle Mapper (SAM) technique was used, which is called in this case Eigenvector Angle Difference (EAD). This technique calculates the angle difference between a test and a reference vector, both of n-dimensions:

$$\alpha = \cos^{-1}\left(\frac{\sum_{i=1}^{n} t_i\, r_i}{\sqrt{\sum_{i=1}^{n} t_i{}^2}\,\sqrt{\sum_{i=1}^{n} r_i{}^2}}\right) \qquad\qquad 19$$

Where t_i is the test vector, r_i is the reference vector and n represents the dimension of the vectors. In this case, the reference is taken as the Eigenvector extracted from the raster that contains the visible wastewater plume, with 4 dimensions, and the other Eigenvectors are compared to it. Figure 8 shows a graphical representation of the EAD in a 2-D space. The smaller the angle between the plume and other rasters' Eigenvectors, the more similar they are. This procedure was conducted in R.
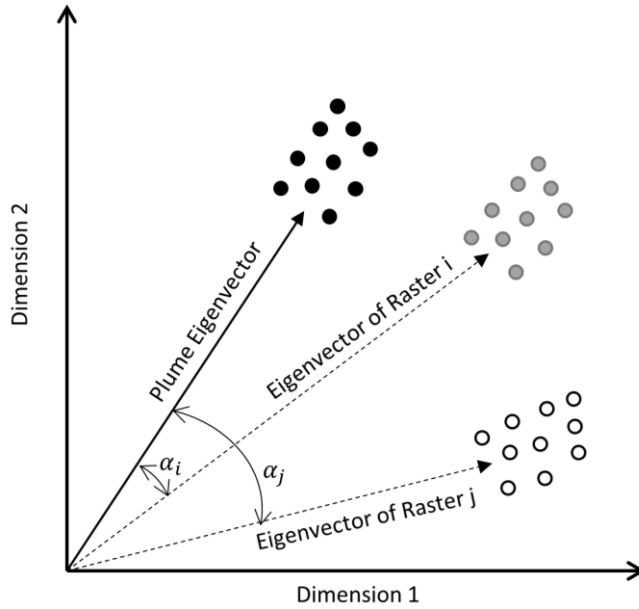
Figure 8: Graphical representation of the Eigenvector Angle Difference (EAD) method

5.2.5. Construction of the Index

After comparison between the plume and the other Eigenvectors, the most similar ones (smaller angle difference) are selected, as they give the direction of transformation that best captures the difference between the plume and the background spatially. The similar Eigenvectors are evaluated, considering the sign (positive or negative) and the relative importance that they give to each IOP, and an optimal linear combination of IOPs (hereby called LCI) is defined from it. To formulate the final WCI, this LCI is applied to each centralized raster and the standardized anomalies are calculated:

$$WCI = \frac{LCI - \mu}{\sigma} \qquad\qquad 20$$

Where *LCI* is the pixel value after centralization and application of the linear combination, μ is the mean LCI pixel value across time and σ is the standard deviation across time.

Standardized anomalies indicate deviations in an easy-to-interpret way since the mean is equal to 0 and the standard deviation is equal to 1. It also enables setting up thresholds for extreme values based on the standard deviation, and the comparison between locations that might have different conditions overall. It detects, therefore, unusual conditions for that specific location.

5.3.   DETECTION OF WASTEWATER PLUMES

Applying the WCI onto the IOPs time-series generated the WCI time series. Areas with depth lower than 1.5 m are excluded in this process to avoid bottom reflectance contamination caused by optically shallow waters. The bathymetric map used for this procedure was obtained from Horn (2021).

To evaluate if the WCI is consistent in detecting wastewater plumes in Conceição Lagoon, the signals produced on images associated with outfalls that occurred in the area between 2019 and 2021 were investigated. Although six incidents have been officially reported in that period, most of them did not coincide with satellite overpass or there was cloud cover impeding analysis. Worth mentioning that overflows from sewage pumping stations, for instance, are typically associated with heavy rainfall and cloud cover conditions. This constitutes a constraint of the method since optical remote sensing relies on clear skies. Yet, depending on the scale and duration of the outfall, the plumes might be detectable after a few days.

Two officially reported wastewater outfall events were analysed by inspection of the WCI classes at the locations of the expected plume. Environmental conditions (i.e. wind, precipitation, water quality measurements, hydrodynamics) and photographic records were also considered for interpretation of the results. In addition, WCI maps of two other dates with potential outfalls were inspected. These were not officially reported events, but the WCI maps indicated anomalous water conditions. Data on other environmental variables were also used to support the hypothesis.

Table 6: Details of analysed wastewater outfall events in Conceição Lagoon between 2019 and 2021

Event	Location	Reported	Type of Outfall	S2 Images
1 – EIP Burst	Middle of Rendeiras Avenue – Central Lagoon	Yes, on 2021-01-25	Burst of WWTP Evapo-infiltration pond. Very large volume of sewage-sediment mixture	2021-01-31 2021-02-03 2021-02-05 2021-02-08
2 – Leak from Sewage Pipe	Centrinho, in front of Via Lagoa Shopping – South Lagoon	Yes, on 2020-05-19	Leak from a broken sewage pipe. Raw waste was being discharged into the stormwater pipe and directly into the lagoon a few days before reported	2020-05-16
3 – Potential Outfall 2021-06-13	Middle of Rendeiras Avenue – Central Lagoon	No	Potential	2021-06-13
4 – Potential Outfall 2021-12-10	Bridge between South and Central Lagoon	No	Potential	2021-12-10

5.4.   IDENTIFICATION OF WCI SPATIO-TEMPORAL PATTERNS

PCA t-mode was applied to the time series of WCI for the identification of the spatio-temporal patterns in Conceição Lagoon. PCA t-mode decomposes a dataset with spatial and temporal components into orthogonal spatial patterns that explain the maximum variance of the dataset over space (PC modes) and Eigenvectors that give the temporal variability of the PC modes (Mascaro et al., 2015). The mathematical principle of the method is the same as described in item 5.2.3 Principal Component Analysis (PCA), but in t-mode each image in time is considered a statistical variable (columns) and the samples in space (pixels) are the observations (rows). The dataset analysed is therefore be represented by the following matrix:

$$\mathbf{A(t,m)} = \begin{bmatrix} WCI_{1,1} & \cdots & WCI_{1,t} \\ \vdots & \ddots & \vdots \\ WCI_{m,1} & \cdots & WCI_{m,t} \end{bmatrix}$$

Where t represents a time-step (each image) and m represents the reshaped 2D image with k rows and i columns ($m = k \times i$).

In this arrangement, the PCA detects recurrent spatial patterns over time (Neeti and Eastman, 2014). Each image is centralized (mean is subtracted) prior to the analysis.

As described before, the projection of the centred matrix $\overline{\mathbf{A}}$ onto the Eigenvectors $\mathbf{V}$ of the covariance matrix gives the Principal Components (PC) matrix:

$$\mathbf{PC} = \overline{\mathbf{A}} \times \mathbf{V}$$

In this case, each column of PC is a spatial pattern (PC mode) and each Eigenvector (column of $\mathbf{V}$) gives the temporal profile of the corresponding PC mode. The eigenvalues of the covariance matrix report the fraction of variance explained by the PCs and are sorted in descending order. This means that the first PC mode (PC_1) explains most of the variability in the dataset, while the last PC mode (PC_N) explains it the least.

The method results in 139 PC modes (number of images) and the "broken-stick" method (Frontier, 1976) is used to select the ones that represent the main spatio-temporal patterns of the WCI in Conceição Lagoon. In this method, the modes are selected if they explain more variance than the corresponding element of the broken stick model. The variance explained by the kth element in the broken-stick model is calculated as (Jolliffe, 2002):

$$\omega_k = \frac{1}{N} \sum_{i=k}^{N} \frac{1}{i}$$

Where N is the total number of PC modes (139 in this case).

The selected PC modes represent the main spatial patterns observed in the analysed period, and their associated Eigenvectors show how these patterns vary in time. For a better interpretation of the results and association with physical processes, the correlation between Eigenvectors and other environmental variables was also investigated. Considering that the occurrence of wastewater outfalls is frequently associated with rainfall and that the hydrodynamics of the Lagoon is mainly influenced by meteorological and hydrological forcings (Silva et al., 2017), the environmental variables examined were accumulated

precipitation, wind speed and wind direction. The correlation between Eigenvectors and environmental variables can indicate if the latter are potential drivers of the spatial patterns (Normandin et al., 2019).

The Linear Trend is also calculated via least-square fitting for the WCI time-series to evaluate the tendency of improvement or worsening of water quality over time, considering a confidence interval of 95%. In addition, the mean, coefficient of variation[1] and linear trend of the four IOPs that comprise the index ($a_{chla}(440)$, $a_{dg}(440)$, $b_{b\,spm}(440)$ and $k_d(PAR)$) were calculated to support interpretation of the spatio-temporal patterns.

---

[1] Coefficient of variation is calculated as the ratio between standard deviation and the mean: CV=(σ/μ)*100

6.   RESULTS AND DISCUSSION

6.1.   DERIVING INHERENT OPTICAL PROPERTIES

6.1.1.   IOPs from In-Situ Rrs

The 2SeaColor model was applied to the 34 in-situ remote sensing reflectance (R_{rs}) spectra which were classified as glint-free (process described in APPENDIX D – FIELD DATA QUALITY CONTROL). As a result, the IOPs associated with each spectrum were obtained, and histograms of these are presented in Figure 9. Absorption by chlorophyll-a (a_{chla}) varied from 0.51 to 2.47 m^{-1}, and had most values centered around 1 m^{-1}. Absorption by non-algal particles and CDOM (a_{dg}) varied from 0.053 to 1.83 m^{-1}, with most values centered around 0.25 m^{-1}. Backscattering by suspended particulate matter ($b_{b\,spm}$) varied from 0.051 to 0.41 m^{-1}, with most values around 0.075 m^{-1}. This results suggest that chlorophyll-a is the main responsible for light attenuation in the waters of Conceição Lagoon.
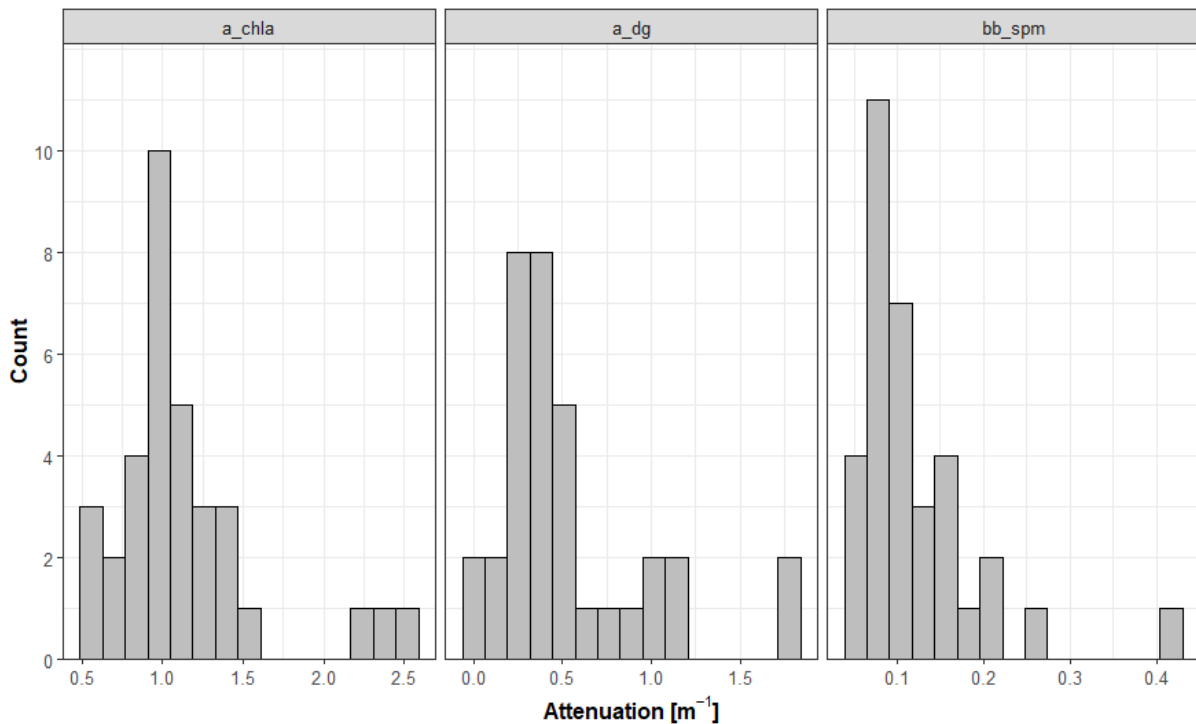
Figure 9: Histograms of the IOPs obtained from in-situ measured remote sensing reflectance

6.1.2.   Matchups of Images and In-Situ Spectra-derived IOPs

The 2SeaColor was also applied to a Sentinel-2 image that was coincidental with in-situ measurements and had clear sky conditions with all sampled points visible (2021/12/10 – FC04). The IOPs extracted from the image and the ones obtained from the in-situ measurements are compared in Figure 10 via type 2 regression. For all the IOPs it is observed low R^2, which means that there is weak or no correlation between the values derived from the image and the ones from the in-situ spectra. For a_{dg} it is seen the

best correlation, with a slope close to 1 and an intercept of 0.15 m^{-1}, meaning that overall the a_{dg} derived from the image are slightly higher than the ones from the in-situ spectra. For $b_{b\,spm}$ the values obtained from the image are much higher than the in-situ (range of 8.5-10 m^{-1} in comparison to 0.06-0.15 m^{-1}). For a_{chla} the range of values from in-situ and image are very similar, but there is no agreement between the match-ups. These extremely high values of $b_{b\,spm}$ could be associated with glint contamination in the image.
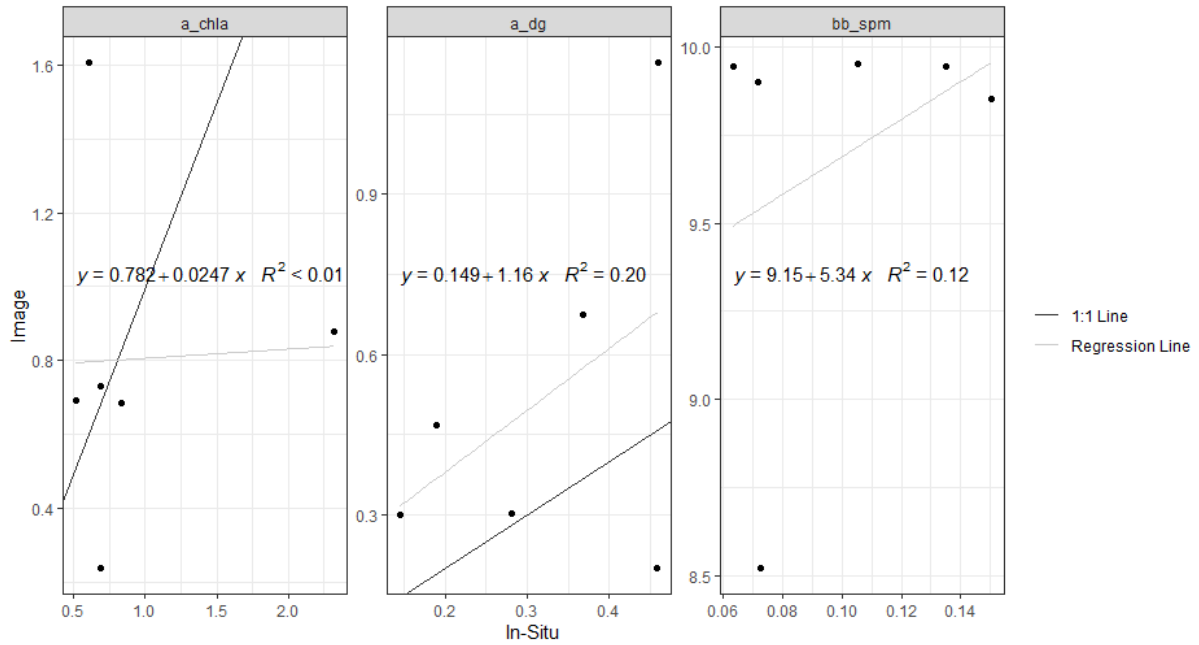
Figure 10: Comparison between IOPs derived from the in-situ measured R_{rs} and the corresponding image on 2021/12/10 via type 2 regression

6.1.3.   Matchups IOPs and Water Constituents Concentration

Figure 11 shows the scatterplots of the concentration of water constituents against their respective IOPs derived from the in-situ spectra. There was no correlation observed between them, which could indicate problems with the in-situ spectra, the water quality measurements, or the model. The same analysis was performed for the IOPs derived from a Sentinel-2 image that was coincidental with in-situ water quality measurements (2021/12/10 – FC04 - Figure 12). In this case, a seemingly high correlation coefficient is observed for chlorophyll-a (R=0.61), but the p-value is also high (>0.1), which means the correlation is not statistically significant.

The application of empirical indices established in the literature to the in-situ spectra also did not provide a statistically significant correlation with water constituents concentration (details about this procedure in

APPENDIX E– COMPARISON 2SEACOLOR WITH EMPIRICAL INDICES). This gives a stronger indication that the in-situ measurements of the Fieldwork might not be consistent. Another potential reason for the poor correlation could be related to the optical complexity of the area. It has been shown that for complex waters, absorption by chlorophyll-a can differ by a factor up to three for the same chlorophyll-a concentration (Yacobi et al., 2015). It should be noted that species of brown algae have been reported in the area several times and were observed during the Fieldwork. These algae have fucoxanthin as an accessory pigment, which has overlapping absorption features with chlorophyll-a and CDOM, influencing their retrievals. Considering all these uncertainties, it was not possible to calibrate the model to retrieve the concentrations of optically active constituents. Nevertheless, a strong agreement between the 2SeaColor-derived IOPs and empirical indices applied to in-situ spectra (see APPENDIX E) gives more confidence that the model is able to at least capture the main features expected of the IOPs and indicate the proportion of the main water quality variables. Since the method is based on variability of IOPs and relative proportion between them, the 2SeaColor was considered adequate for further use despite the mentioned limitations.
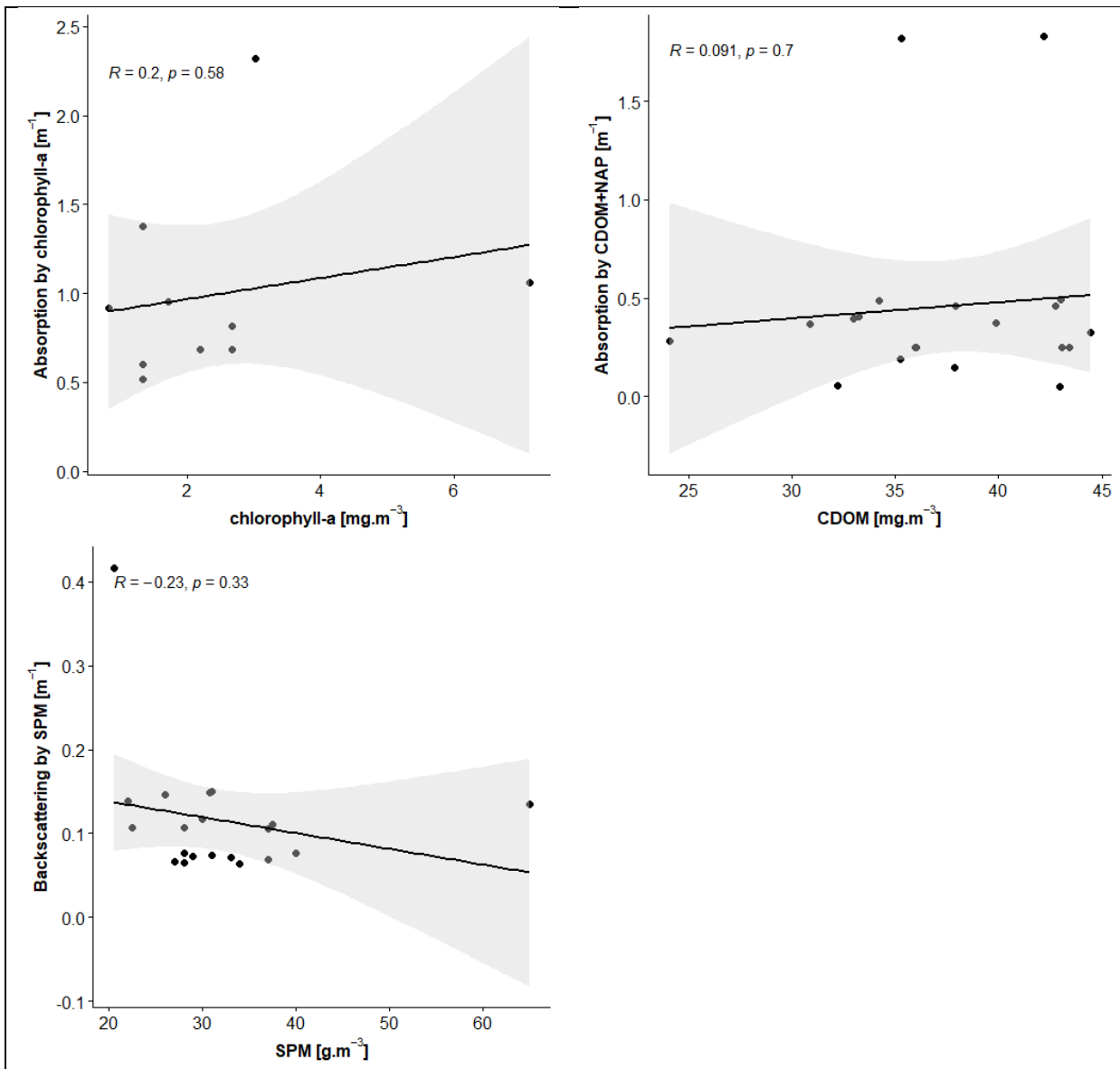
Figure 11: Scatterplots of concentration of water constituents from in-situ samples against their respective IOPs derived from in-situ spectra, with the regression line in black, the confidence interval in grey, the Pearson correlation (R) and the corresponding p-value (p)
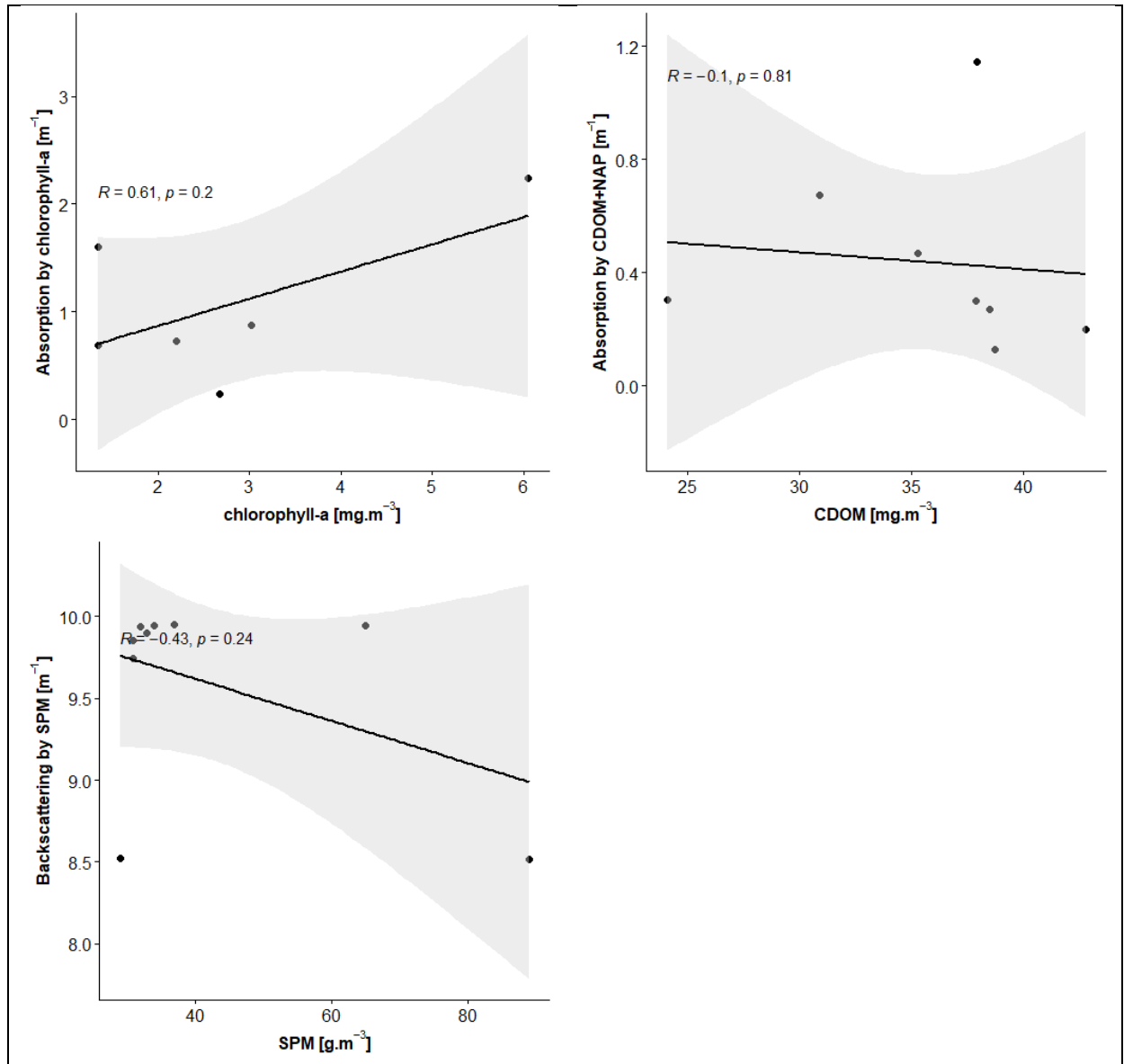
Figure 12: Scatterplots of the concentration of water constituents from in-situ samples against their respective IOPs derived from Sentinel-2 image, with the regression line in black, the confidence interval in grey, the Pearson correlation (R) and the corresponding p-value (p)

6.2.   FORMULATION OF THE WASTEWATER INDEX

PCA analysis of subsetted IOPs rasters resulted in 139 Eigenvectors that best explain the variance in them. Comparing the Plume Eigenvector (associated with the plume observed on 2021/02/08) with the others via EAD, we observe angle differences ranging from 0.07 to 2.37 radians, with a mean of 0.78 radians or 45° (see Figure 13). This indicates that the Plume Eigenvector is distinct from most of the other Eigenvectors, but there are similar ones that give the direction of transformation that best captures the difference between the plume and the background spatially.
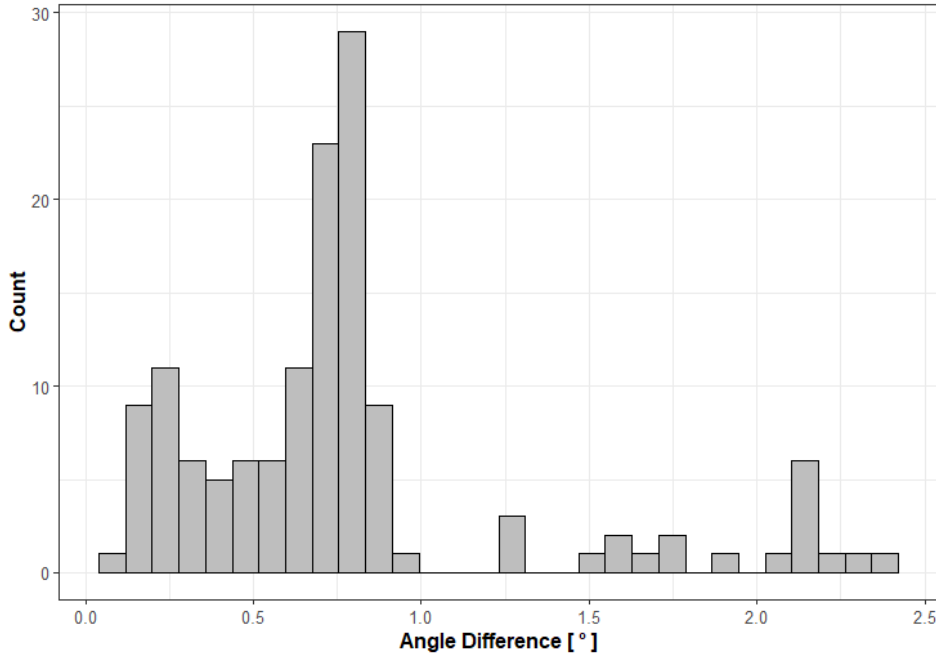
Figure 13: Histogram of the Eigenvectors Angle Difference, representing the distribution of the angle difference between the Plume Eigenvector (reference) and the Eigenvectors of other images.

Based on the distribution of angles differences, a threshold of 0.15 radians (8.5 degrees) was established to select the equivalent Eigenvectors, which are detailed in Table 7. It can be seen that the elements of the Eigenvectors are all positive, which means that the IOPs associated with them positively influence the PC. The relative importance of each IOP, hereby called the weight (w), can be calculated from the elements of the Eigenvectors ($w_{1i} = v_{1i}/\sum v$).

Table 7: Details of the Eigenvectors which are the most similar to the Plume Eigenvector (Reference)

Date	v_{11} (k_{dPAR})	v_{12} (a_{chla})	v_{13} (a_{dg})	v_{14} ($b_{b\,spm}$)
2021-02-08 - Reference	0.95	0.17	0.32	0.9
2019-09-27	1.23	0.15	0.44	1.04
2019-10-22	1.81	0.3	0.64	2.22
2019-12-28	0.9	0.25	0.35	0.72
2020-01-15	0.78	0.05	0.26	0.89
2020-02-24	0.71	0.19	0.22	0.52
2020-08-04	2.64	0.89	0.68	2.72
2020-08-07	0.59	0.1	0.29	0.7
2021-09-26	1.15	0.29	0.45	0.91

Table 8 presents the weights of each IOP in the equivalent Eigenvectors, which are very similar to each other. The strongest weights are given to $k_{d\,PAR}$ and $b_{b\,spm}$, with approximately 40% each. We can derive from it that the wastewater plume is mostly characterized by a high concentration of particulate matter and low light penetration. Coloured dissolved organic matter and detritus have a secondary role in the description of the wastewater plume, with 15%, while chlorophyll-a has the lowest influence (8%). This was expected, as chlorophyll-a increase due to wastewater would likely be a post-effect following nutrient enrichment and depending on other environmental conditions (i.e. temperature, column mixing, etc.).

Table 8: Weights of each IOP in the Eigenvectors

Date	w_{11} $(k_{d\,PAR})$	w_{12} (a_{chla})	w_{13} (a_{dg})	w_{14} $(b_{b\,spm})$
2021-02-08 - Reference	0.41	0.07	0.14	0.38
2019-09-27	0.43	0.05	0.15	0.36
2019-10-22	0.36	0.06	0.13	0.45
2019-12-28	0.41	0.11	0.16	0.32
2020-01-15	0.39	0.03	0.13	0.45
2020-02-24	0.43	0.12	0.13	0.32
2020-08-04	0.38	0.13	0.10	0.39
2020-08-07	0.35	0.06	0.17	0.42
2021-09-26	0.41	0.10	0.16	0.33
Mean	**0.40**	**0.08**	**0.14**	**0.38**
Standard Deviation	**0.03**	**0.04**	**0.02**	**0.05**

The mean weights are used to compute the optimal Linear Combination of IOPs (LCI) for wastewater detection:

$$LCI = 0.40.\ \overline{k_{d\,PAR}} +\ 0.08.\overline{a_{chla}} + 0.14.\ \overline{a_{dg}}\ + 0.38.\overline{b_{b\,spm}} \qquad\qquad 21$$

The WCI is then given as the standardized anomalies of the LCI. Based on the expected normal distribution of standardized anomalies, classes of Water Quality can be derived from the WCI values, as is presented in Figure 14. Finally, the WCI was applied to the images, generating a WCI maps time series with Water Quality Classification.
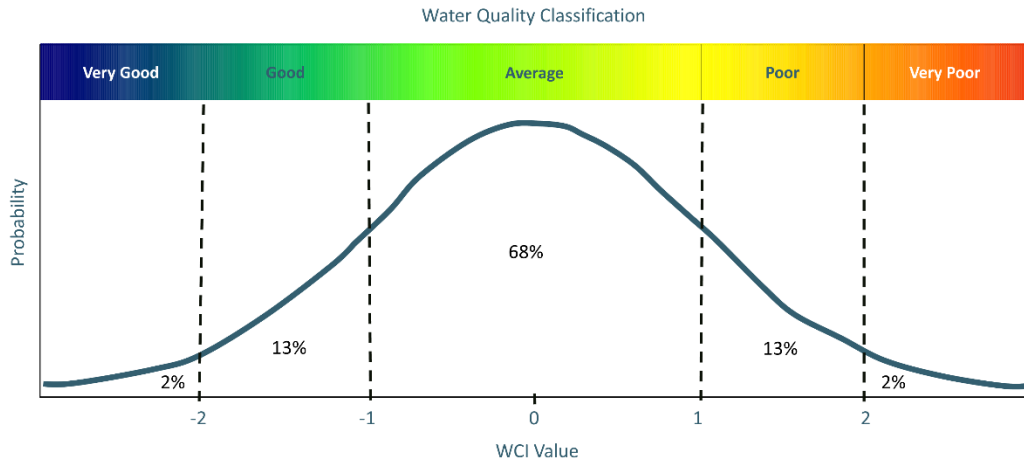
Figure 14: Classes of Water Quality and their relation to WCI values and the expected probability distribution

6.3. DETECTION OF WASTEWATER PLUMES

The WCI Maps Time-Series was used to investigate plumes of four wastewater outfall events, two officially reported and two potential. The meteorological data used to support the analysis are presented in APPENDIX F– COMPILATION OF METEOROLOGICAL DATA. The following sections describe the results for each of them.

6.3.1. Event of EIP Burst – 2021-01-25

The Evapo-Infiltration Pond (EIP) of the Conceição Lagoon Wastewater Treatment Plant (CL WWTP) burst on the 25th of January 2021 after intense rainfall, releasing approximately 79,000 m³ of effluent-sediment mixture directly into Conceição Lagoon (Figure 15). The EIP is where the sewage is disposed of after treatment, but monitoring showed that on several occasions the efficiency of the WWTP was below what is required by law, presenting high biological oxygen demand (BOD), nitrogen and phosphorus levels (ARESC, 2021). It is estimated that the event released to the lagoon 1.44 tons of BOD, 2.04 tons of ammoniacal nitrogen, 0.43 tons of nitrate and 0.36 tons of total phosphorus (Odreski et al., 2021).

Figure 15: Picture of the EIP burst on the 25th of January 2021 (Source: Corpo de Bombeiros, 2021)

Following the event, there were four Sentinel-2 images for which the WCI was applied:

- 2021-01-31
- 2021-02-03
- 2021-02-05
- 2021-02-08

The one from 2021-01-31 had scattered clouds in the area of interest, and, therefore, was discarded.

The image of the WCI for 2021-02-03 is presented in Figure 16. It can be observed that there are high values (indicating poor quality) towards the East of the burst area, which could suggest the transport of the plume into that area. Other studies have indicated a residual hydrodynamic flux in that direction (Silva et al., 2017). In addition, the wind was blowing from NW, favouring this transport. Cloud cover prevents interpretation of the rest of the image.

The image of 2021-02-05 (Figure 17) shows that the WCI values are overall very similar to the average. The noise seen in the Northern part of the Lagoon corresponds to clouds, while in the South Lagoon the 2SeaColor model masked some values as NoData. A potential reason why the plume is not seen on this day anymore could be the wind, which was coming from the NE direction, with an average speed of 1.6 m/s. The wind from this direction tends to create waves that provide intense mixing to the water column and it also goes in the opposite direction of the expected flow of the plume.

On the 8th of February, 14 days after the event, it is seen again a plume coming from the area of the EIP burst, with high WCI values (Figure 18). In-situ measurements conducted 4 days later by the State's Public Services Regulation Agency (ARESC, 2021) indicated very high values of Nitrogen and BOD in the Central Lagoon. On this day the wind was from the SE direction, which tends to keep the water calmer in that area and favour the flow of the plume towards the NW. High WCI values are also seen in the Northern Lagoon. This could indicate contamination of the waters of that area, which is in line with reported events of fish die-offs and oxygen depletion in the extreme North of the lagoon in the following days (UFSC, 2021).
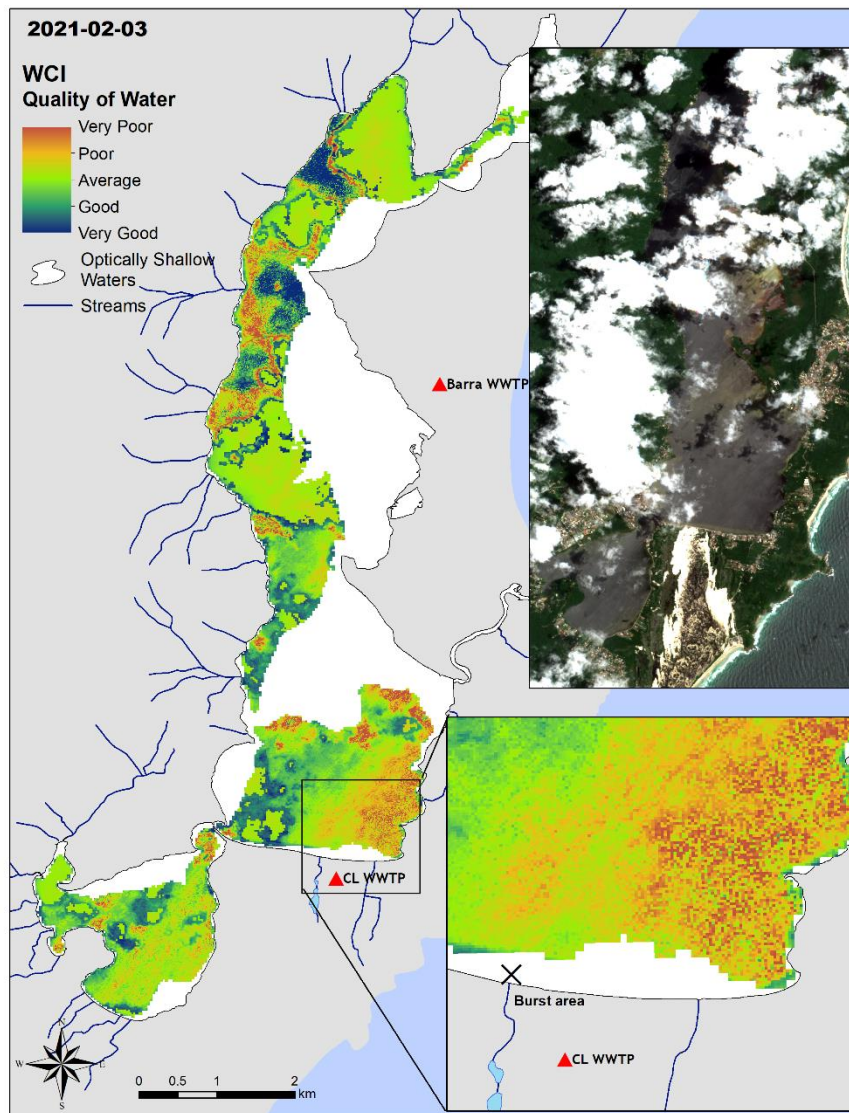
Figure 16: Map of the WCI in Conceição Lagoon on 2021-02-03, with detail of area with poor quality and Sentinel-2 RGB image showing the cloud cover that impairs analysis
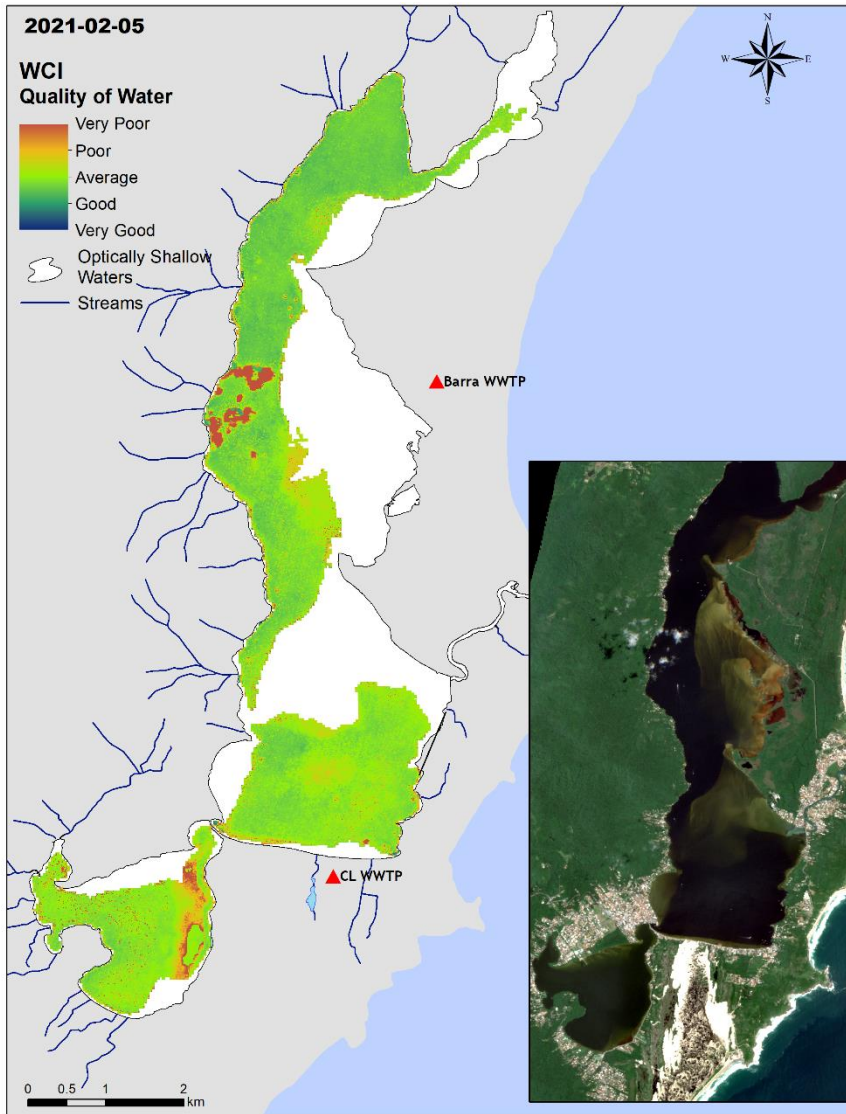
Figure 17: Map of the WCI in Conceição Lagoon on 2021-02-05 with detail of Sentinel-2 RGB image showing cloud cover in the North Lagoon that impairs analysis
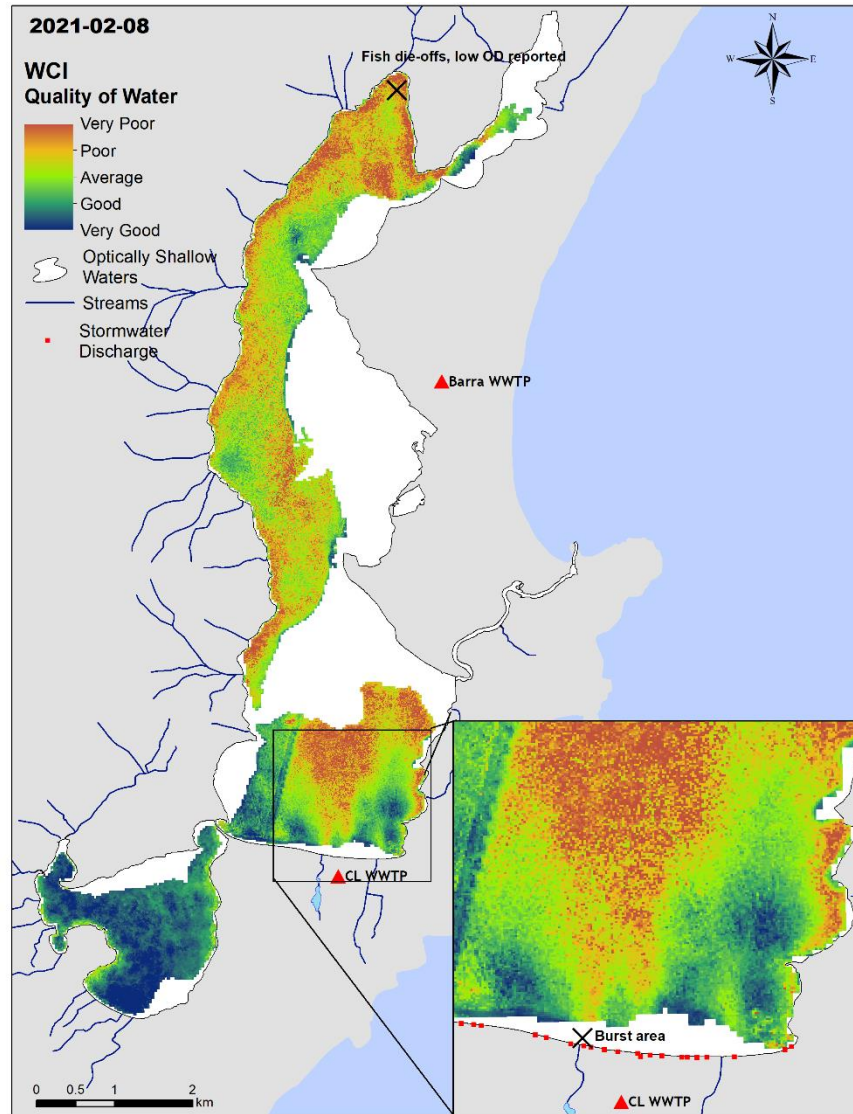
Figure 18: Map of the WCI in Conceição Lagoon on 2021-02-08 with detail of the EIP burst area and plume of worse water quality

6.3.2. Leak from Sewage Pipe – 2020-05-19

On the 19th of May 2020, it was identified a leak from the sewage pipe in Centrinho da Lagoa, the neighborhood's urban centre. Inspection by the city's Environmental Agency (FLORAM) verified that, due to a broken sewage pipe, raw waste was being discharged into the stormwater system and directly into the Lagoon (Figure 19). In the WCI image of 2020-05-16 (Figure 20) there are high values indicating poor water quality around the area of the leak and across the bridge, in Cooperbarco Pier. The presence of shallow waters in that region prevents evaluation of the conditions closer to land.

Areas with worse quality are also seen in the South Lagoon. This is supported by reports that showed extensive scum patches since the 14th of May (2 days before the image) in that region. Laboratory analysis showed that the scum was decaying organic matter and biofilm formed by bacteria, diatoms, cyanobacteria and dinoflagellates (UFSC, 2020). Other deviant hotspots in Central Lagoon were caused by cloud cover and boats, as it can be seen in the true-color image.

Figure 19: Picture of the inspection test that verified raw sewage being discharged into the Lagoon on the 19th of May 2020 (Source: Eduardo Cristófoli/NDTV, 2020)

a) Centrinho da Lagoa

b) Cooperbarco Pier

c) Canto da Lagoa
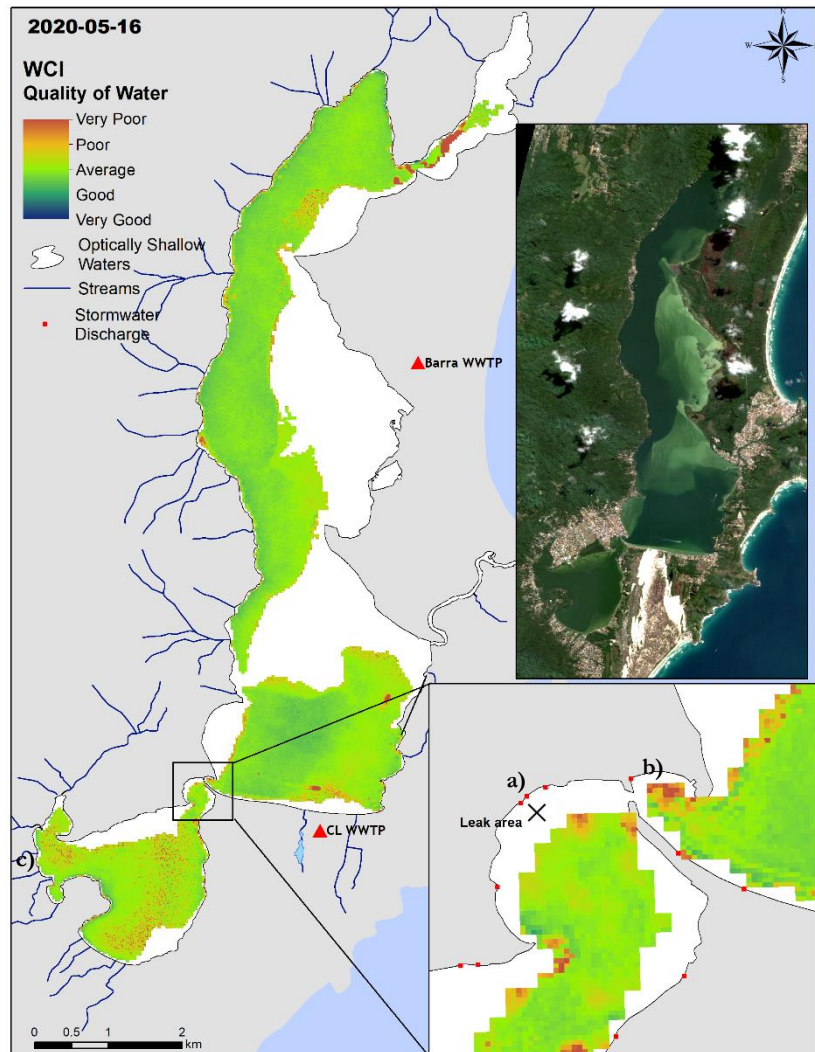
Figure 20: Map of the WCI in Conceição Lagoon on 2020-05-16, with the detail of the leak area. Pictures a), b) and c) show scum that was seen in the locations pointed in the map.

6.3.3. Potential Outfall – 2021-06-13

On the WCI map of the 13th of June 2021 (Figure 21), we can observe a plume-like shape in the Rendeiras area, close to several stormwater discharge points and the drainage area of the CL WWTP EIP (see detail in Figure 21). It follows a period of heavy rainfall, with accumulated precipitation in the last five days equal to 121 mm, almost double the climatological precipitation for June (75.7 mm (Odreski et al., 2021)). The wind was blowing from the SE direction, which favours the spread of the plume as seen on the map.

Hotspots of worse water quality are also seen in the South Lagoon. It should be noted that three days later, on the 16th of June, photographic records show foam in the area close to the bridge (Figure 22). Since the recurrent hydrodynamic flux in this area is from the South to Central Lagoon (Figure 23 (Silva, 2013)), this could mean that the worse quality water verified on the 13th further South moved towards the bridge and into Central Lagoon. Furthermore, on the 19th of June, in-situ measurements from the Treaty for the Lagoon[2] showed values of faecal coliforms higher than the allowed by Brazilian legislation for bathing waters (>1,000 MPN/100 ml) in the areas around the bridge.
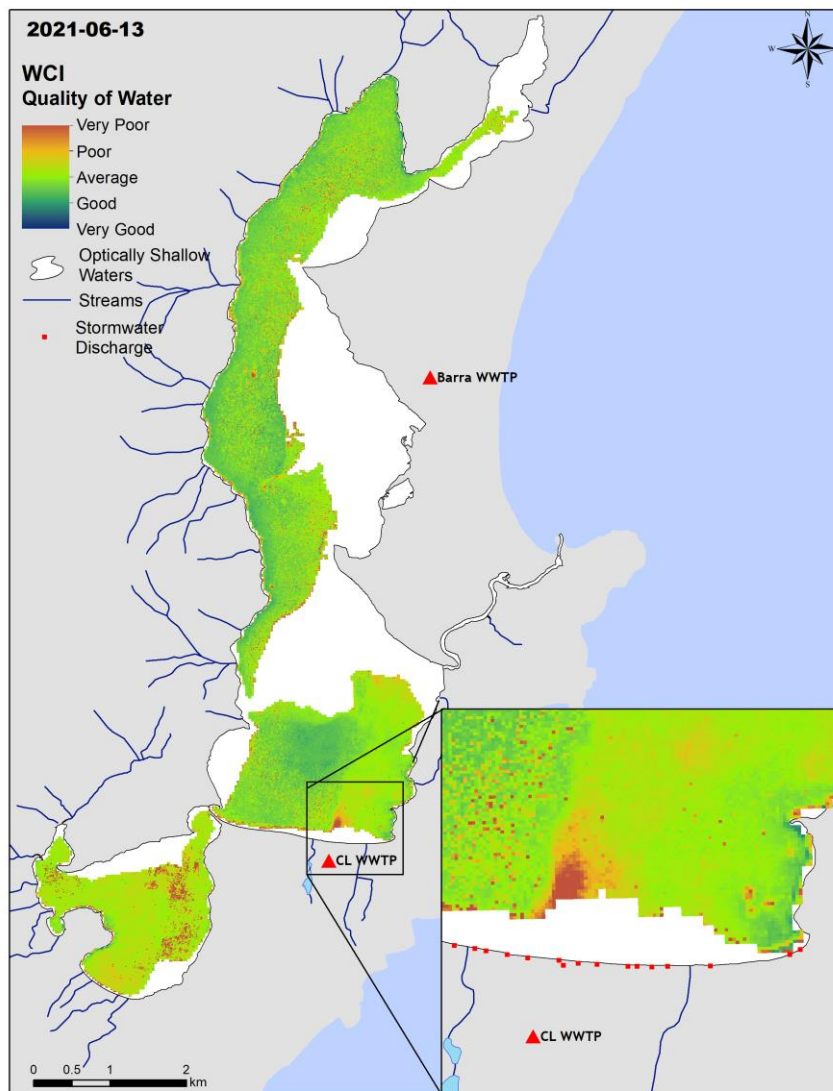
Figure 21: Map of the WCI in Conceição Lagoon on 2021-06-13 with detail of a potential wastewater plume with very poor water quality

---

[2] Inspection and monitoring program of the sewage system operator (CASAN) in partnership with the municipality – data publicly available from https://tratopelalagoa.com.br/pt/resultado_testes_qualidade_agua/

Figure 22: Picture of foam present around the bridge area on the 16th of June 2021
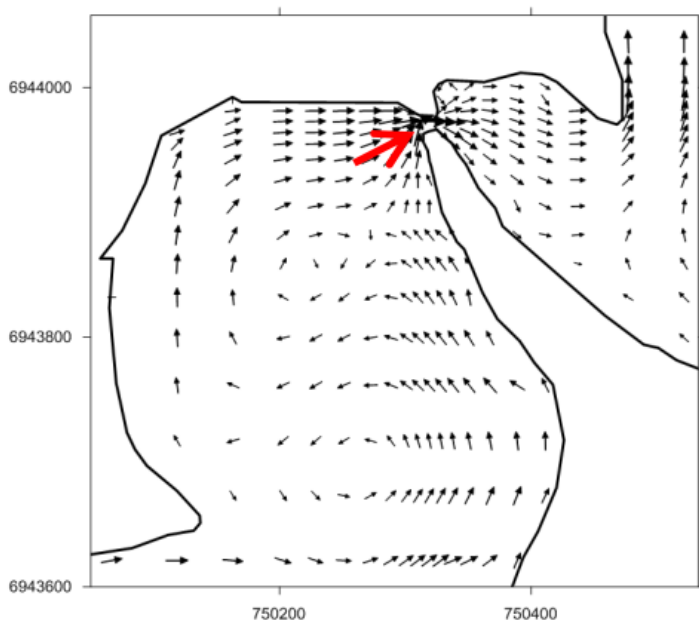
Figure 23: Mean circulation in the area of connection between the South and Central Lagoon. This is the result of a hydrodynamic model simulating a period between 2012 and 2013. Adapted from Silva (2013)

6.3.4. Potential Outfall – 2021-12-10

On the WCI map of December 10[th,] 2021 (Figure 24) we observe plume-like shapes of worse water quality coming from stormwater discharge points or urbanized stream outlets. The 5 days accumulated precipitation was 42 mm, 25% of the climatological mean for December, which could be contributing to the worsening of the water quality in those areas. It should be noted that this is the touristic high season, when the population of the basin can triplicate and problems of contamination tend to worsen (Silva et al., 2017).

One potential wastewater plume is observed in Rendeiras Avenue's extreme eastern point, called Retiro (see detail Figure 24). Retiro receives stormwater contribution from a relatively large urbanized area and is one of the points monitored by the State's Environmental Institute (IMA) for bathing quality[3] that is frequently classified as unsafe, influenced by low velocities (Figure 25). The direction of the wind (SE, 131°) also corroborates the shape of the plume.

Other hotspots are seen in the South Lagoon: at the outlet of Apa stream, at the Badejo Hill Bay and Porto da Lagoa. These are also typically low circulation areas that tend to accumulate the load carried by streams (Figure 25)(Odreski, 2012). Very close to the outlet of Apa stream there is a sewage pumping station, which on several occasions following heavy rainfall has been recorded overflowing raw sewage directly into the stream and, consequently, to the lagoon. This could be another event like this. In Porto da Lagoa we see that there is no sewage collection system, meaning that the buildings must dispose of sewage via individual septic tanks, which commonly present irregularities with waterproofing and distance to groundwater level (Cabral et al., 2019). In conditions of persistent rainfall and heavy human occupation, the chances of polluted water reaching the lagoon are higher. It is worth mentioning that on the night of the 6th of December (4 days before the image), the community recorded a large number of aquatic organisms (i.e. fish, crabs, shrimp) dead in that area.

Hotspots of very poor water quality to the North of the lagoon were caused by cloud cover and the values are therefore not interpretable.

---

[3] IMA Bathing Water Quality Monitoring data are publicly available from https://balneabilidade.ima.sc.gov.br/
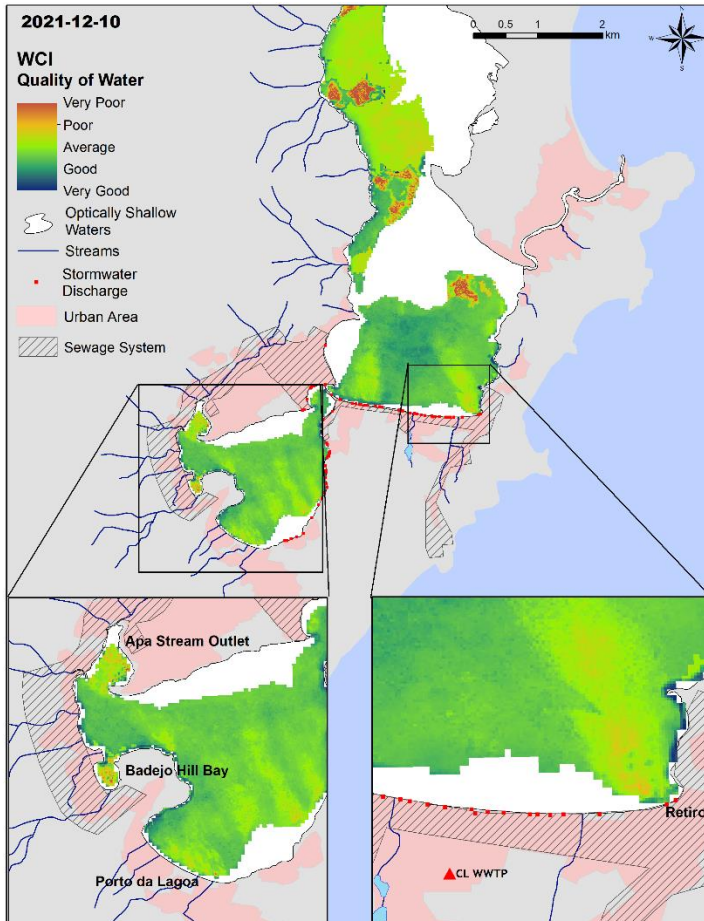
Figure 24: Map of the WCI in Conceição Lagoon on 2021-12-10, with details of potential wastewater plumes in Retiro, Apa Stream Outlet, Porto da Lagoa and Badejo Hill Bay
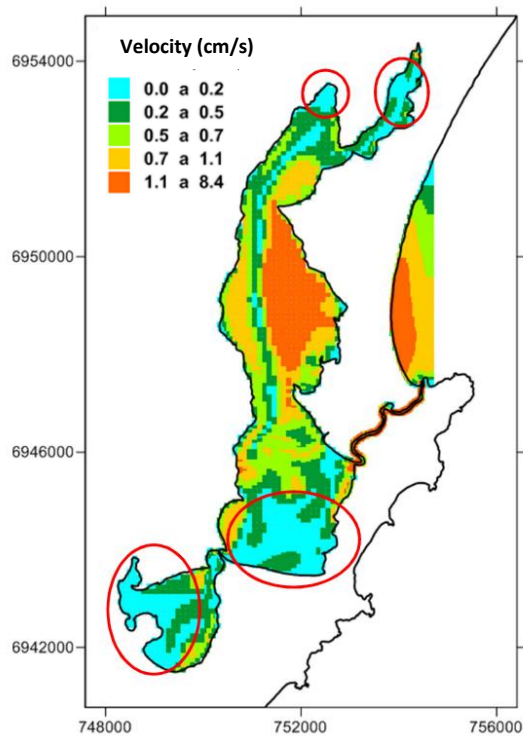
Figure 25: Mean velocities in Conceição Lagoon as a result of a hydrodynamic model simulating a period between 2012 and 2013. Adapted from Silva (2013)

6.4.   WCI SPATIO-TEMPORAL PATTERNS

The t-mode PCA transformed the WCI maps time-series into 139 PC modes (spatial patterns) with their associated Eigenvectors (temporal scale). After applying the broken-stick method, the first 7 PC modes were considered relevant patterns (higher values in comparison to broken-stick – see Figure 26).
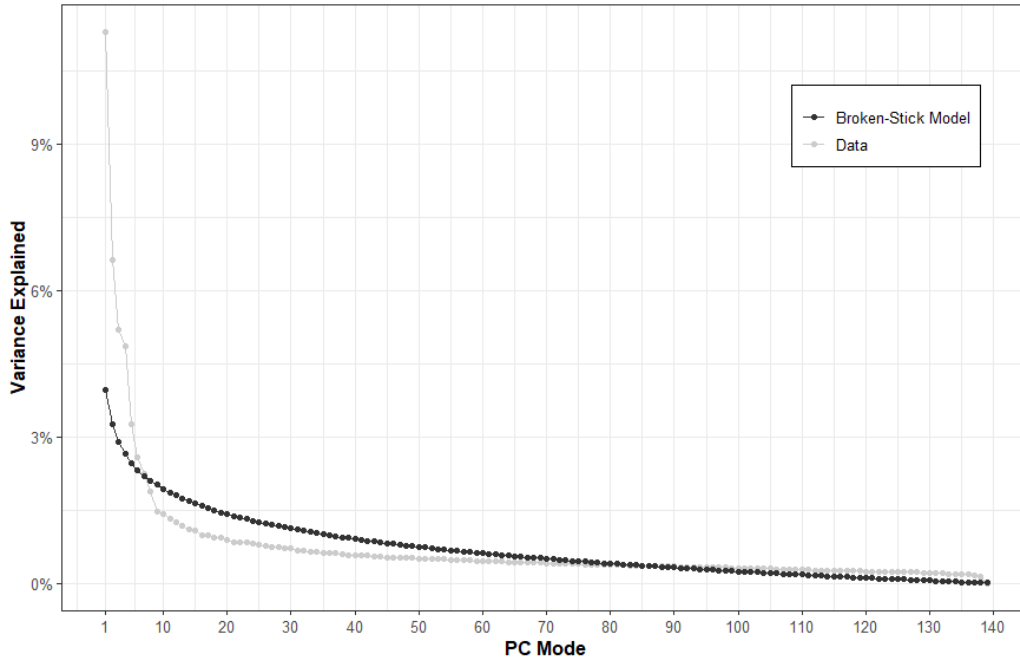
Figure 26: Variance explained by each PC mode in comparison with the broken-stick model

The selected PC modes and the variance explained by them are presented in Figure 27. We observe that the first mode explains 11.29% of the variance in the WCI time series, and all the seven modes together account for only 36% of the total variance. This suggests that there are no strongly recurrent patterns of the WCI, highlighting the irregular nature and unpredictability of wastewater outfalls.

Figure 28 presents the Eigenvectors of each PC mode in time. There is no clear seasonality verified, but the values change between negative and positive constantly, and the associated pattern is reversed according to the sign Eigenvectors elements assume. For instance, in PC1, when the Eigenvector elements are positive there are high values of WCI in the North Lagoon and low values in the South. When Eigenvector elements assume negative values, South Lagoon has higher WCI and therefore worse water quality than the North.

Looking at the correlation between the Eigenvectors of the modes and environmental variables (Table 9), it is observed that precipitation does not seem to influence the spatial patterns, while wind could be playing a role. The Eigenvectors of PC1 and PC3 have slight correlations with wind speed and direction. This means that the variation in the Eigenvector elements (which in turn influence the spatial pattern in sign and scale) are somewhat affected by wind speed and direction. Eigenvectors of PC5 and PC7 are only correlated with wind direction. The highest correlation is seen between wind direction and Eigenvector of PC7, with 0.31. This means that the pattern of PC7 is potentially driven by wind direction.

We can derive that WCI is highly variable both in time and space, with no significantly recurrent temporal or spatial patterns, but the wind could play a role in the dispersion and detection of wastewater plumes. Worth mentioning that patterns in PCA are influenced by noise (cloud cover and shadows, for instance) and could be the result of statistical artifacts, especially considering the low explainability of the modes.
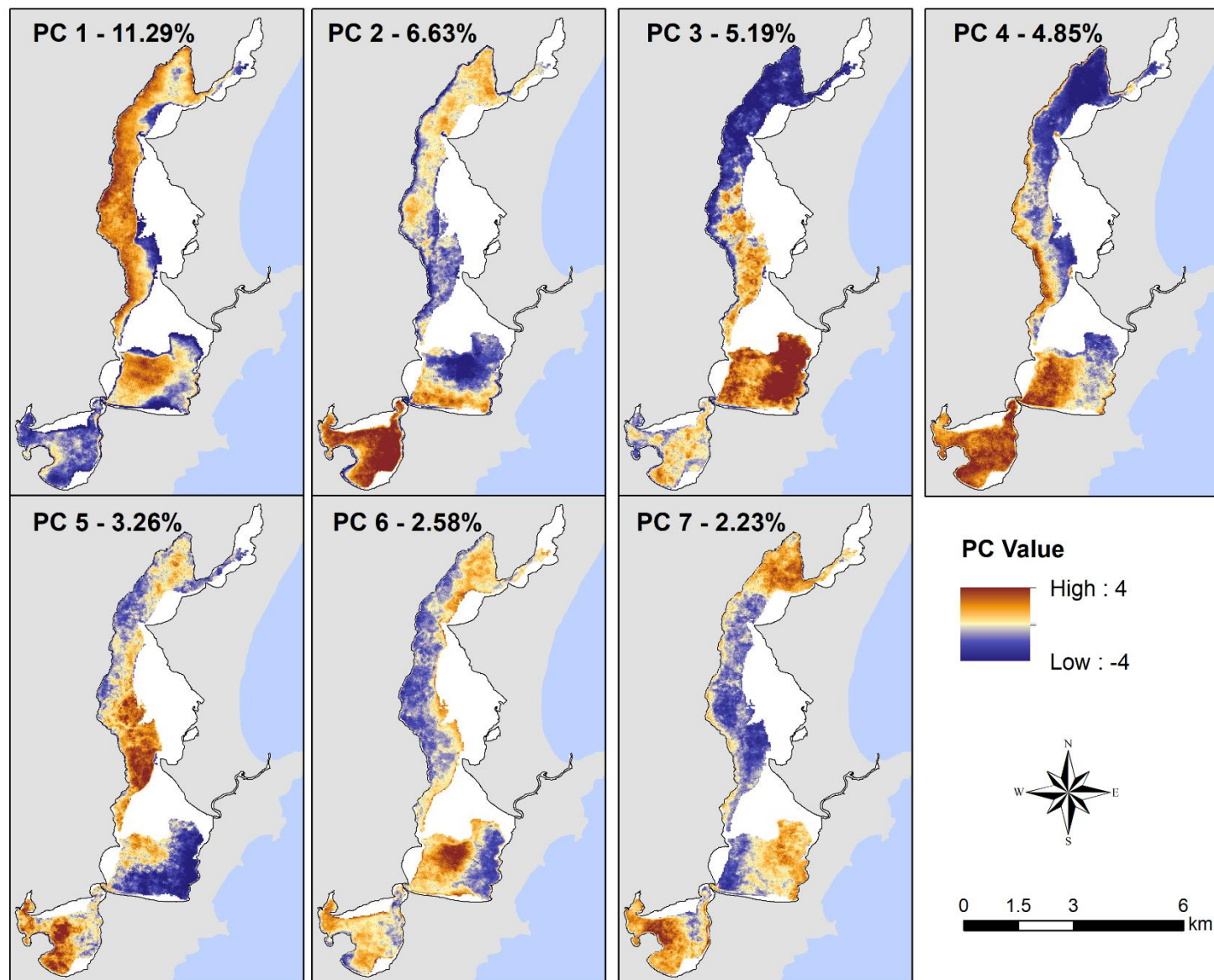
Figure 27: PC modes of WCI and their respective explained variance.
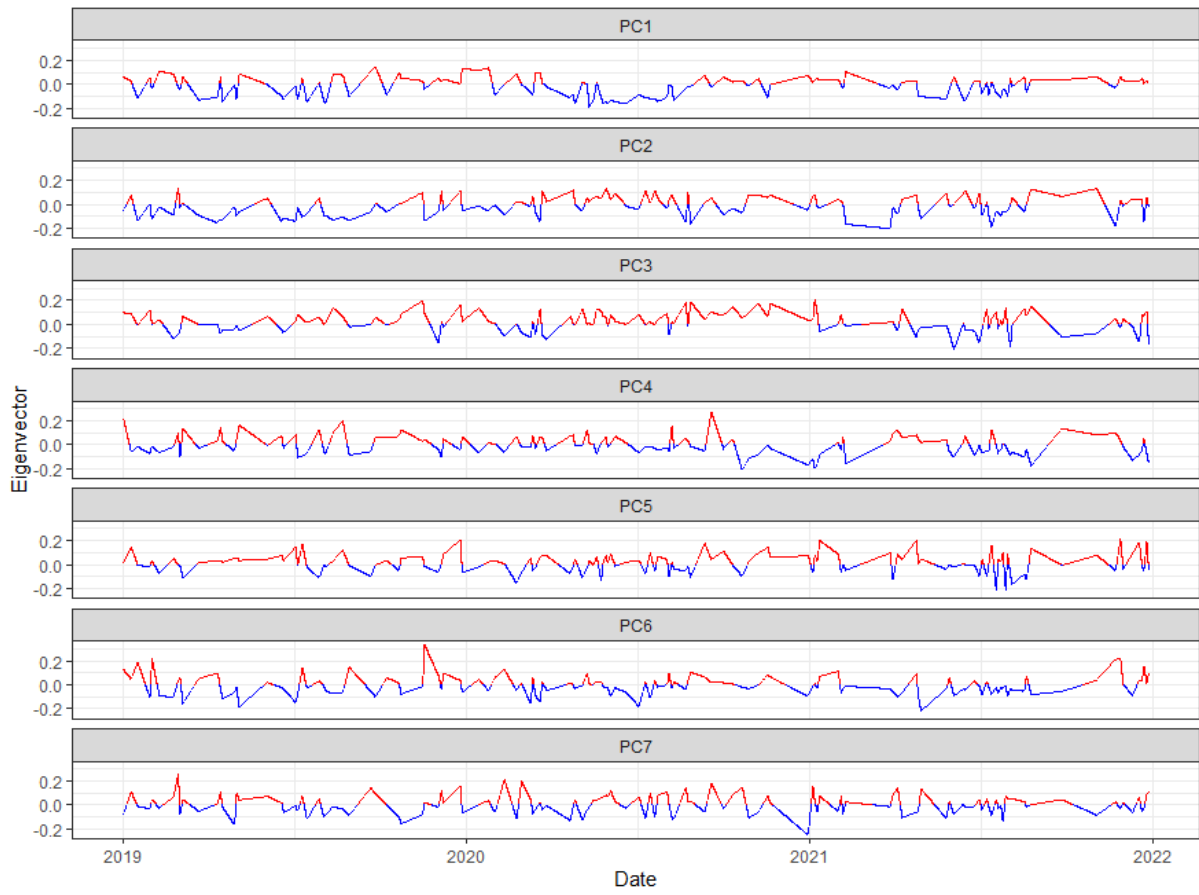
Figure 28: Eigenvectors of the first seven PC modes. Red colour denotes positive values and blue negative values.

Table 9: Pearson correlation coefficient between the first seven modes' Eigenvectors and environmental variables, highlighting the ones that are statistically significant at 95% confidence level.

Eigenvectors of	5-Days Accumulated Precipitation	Wind Speed	Wind Direction[a]
PC1	0.09	**0.23** [b]	**0.19**[b]
PC2	0.08	-0.09	0.08
PC3	-0.06	**0.24**[b]	**0.17**[b]
PC4	-0.03	0.01	0.13
PC5	0.16	-0.07	**0.18**[b]
PC6	0.17	0.03	0.09
PC7	0.02	-0.03	**0.31**[b]

[a] Circular-Linear correlation between a circular variable (wind direction) and linear variable (Eigenvector)

[b] Statistically significant correlation at 95% confidence level.

6.4.1. IOPs General Patterns

To aid interpretation of the WCI spatio-temporal patterns, the mean and coefficient of variation (CV) of $k_d(PAR)$, $b_{b\,spm}(440)$, $a_{dg}(440)$ and $a_{chla}(440)$ were calculated and are presented in Figure 29, Figure 30, Figure 31 and Figure 32, respectively.

The mean $k_d(PAR)$ is highest closer to the margins of the lagoon and there are hotspots in the middle of the Central and in the South Lagoon. A very similar pattern is observed for $a_{chla}(440)$ and $b_{b\,spm}(440)$, but for the latter lower values are seen, especially in the South Lagoon. Mean $a_{dg}(440)$ is very high in the South Lagoon and in the extreme North arm, regions characterized by outlets of urbanized rivers.

It is possible to observe a hotspot of high values for all IOPs in the central lagoon, which is very persistent (low CV for all IOPs as well). This is an area under the influence of drainage from the CL WWTP disposal site and stormwater from urbanized area in general, which could be potential drivers.

For all four IOPs it is also observed high CV towards the North Lagoon and some spots closer to land in Central and South Lagoon. This is an indication that on those locations the values deviate from the mean considerably over time. This could be associated with the PC modes obtained from PCA of the WCI, where high magnitude PC values (positive or negative) are also often observed in the same areas. Nevertheless, this is just a visual interpretation that is not straightforward and further analysis would be required to establish a relation.
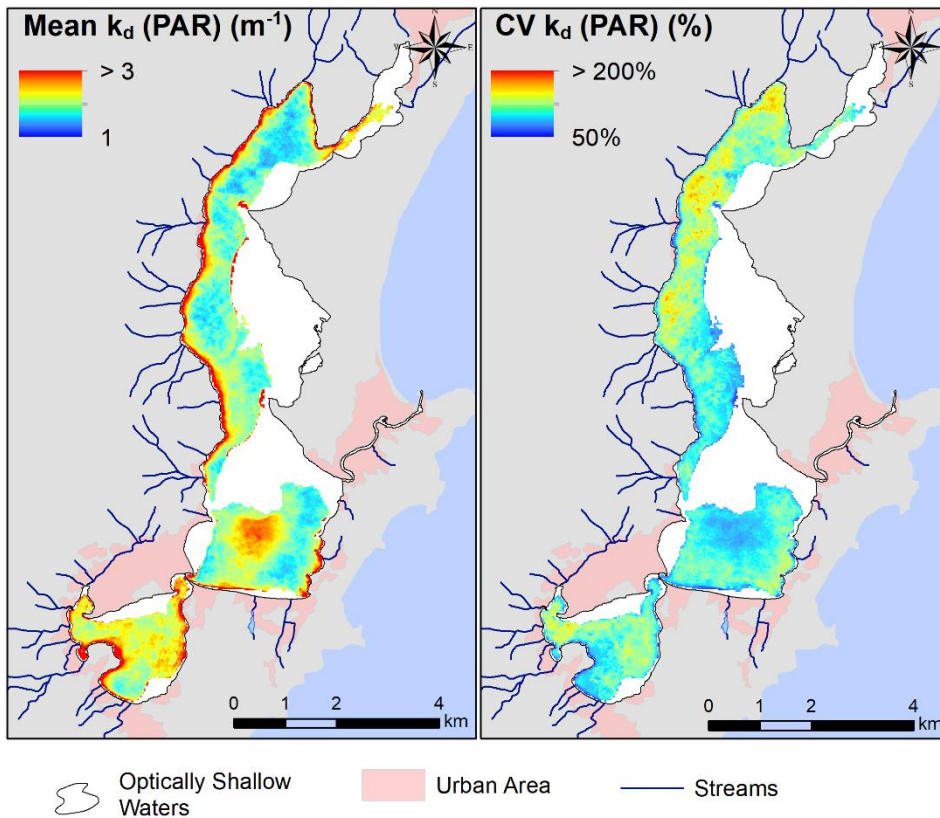
Figure 29: Mean and coefficient of variation (CV) of $k_d(PAR)$
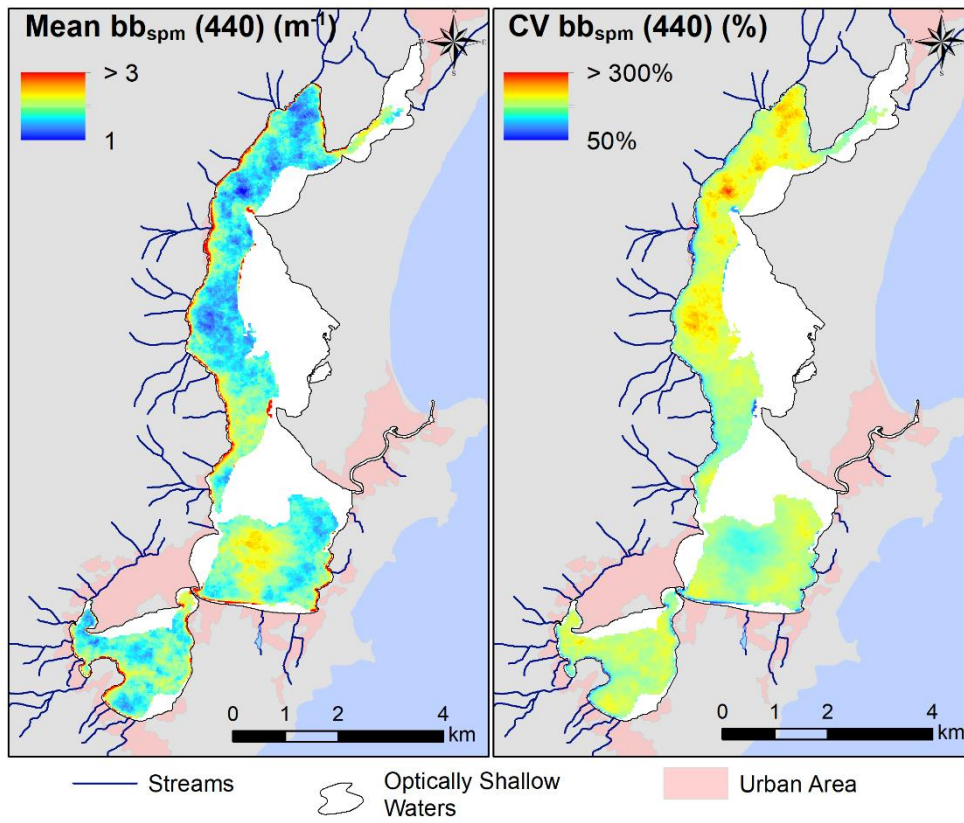
Figure 30: Mean and coefficient of variation (CV) of $b_{b\,spm}(440)$
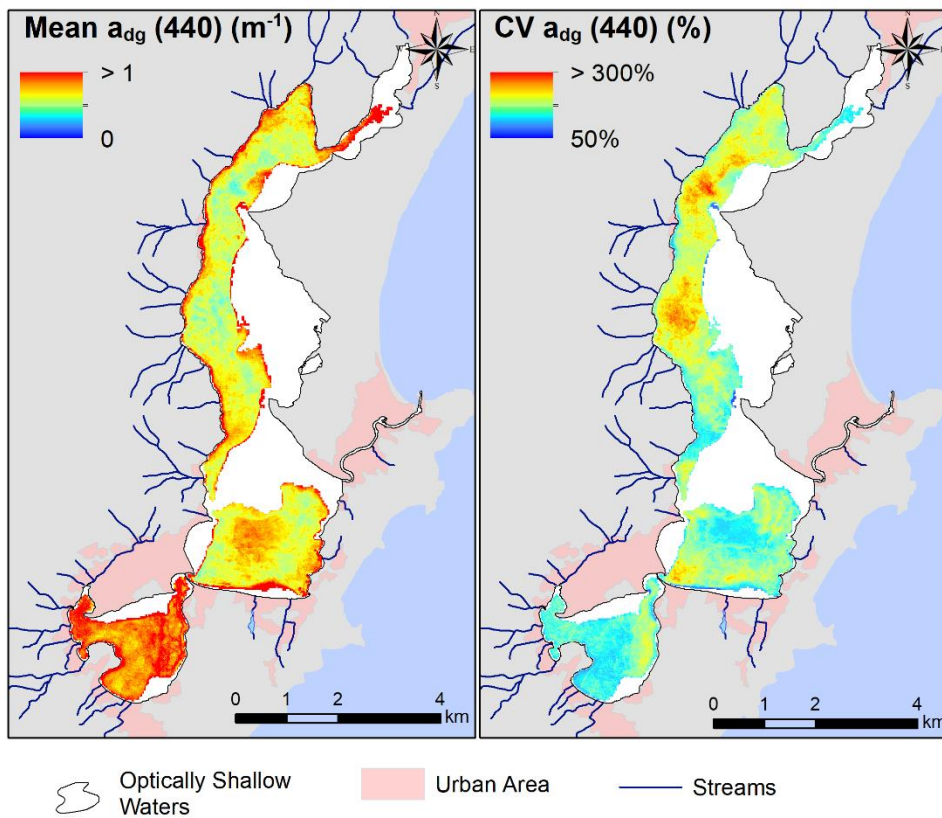
Figure 31: Mean and coefficient of variation (CV) of $a_{dg}(440)$
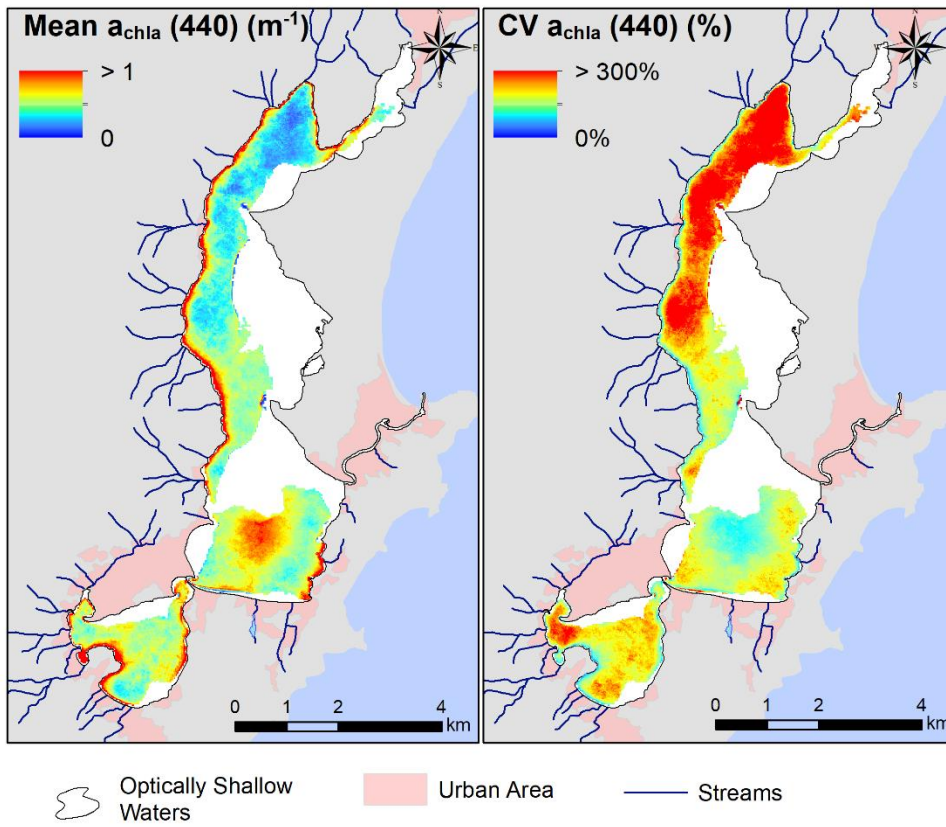
Figure 32: Mean and coefficient of variation (CV) of $a_{chla}(440)$

6.4.2. Trend Analysis

The trend of the WCI per day between 2019 and 2021 is shown in Figure 33, where we can see areas with water quality improvement (negative values) or worsening (positive values). Worsening is seen mainly in the South Lagoon, in areas closer to the land and also in the extreme North. The worsening in the South Lagoon could be associated with the surrounding urban occupation and lower exchange with seawater. There has been several reports of raw sewage outfalls into the Apa river, which flows into that area. Closer to the land we also have more influence of anthropic activities and river outlets, which could be increasing pollutant loads. Worsening in the extreme North of the Lagoon could be due to the expansion of Rio Vermelho district. Rio Vermelho has been experiencing accelerated and disordered population growth (ICES-BID, 2015), with the added issue that there is no sewage collection and the hydrographic basin drains into the Lagoon. Improvement of the water quality can be seen in the deeper areas of Central Lagoon, potentially due to the exchange with the Barra Channel.
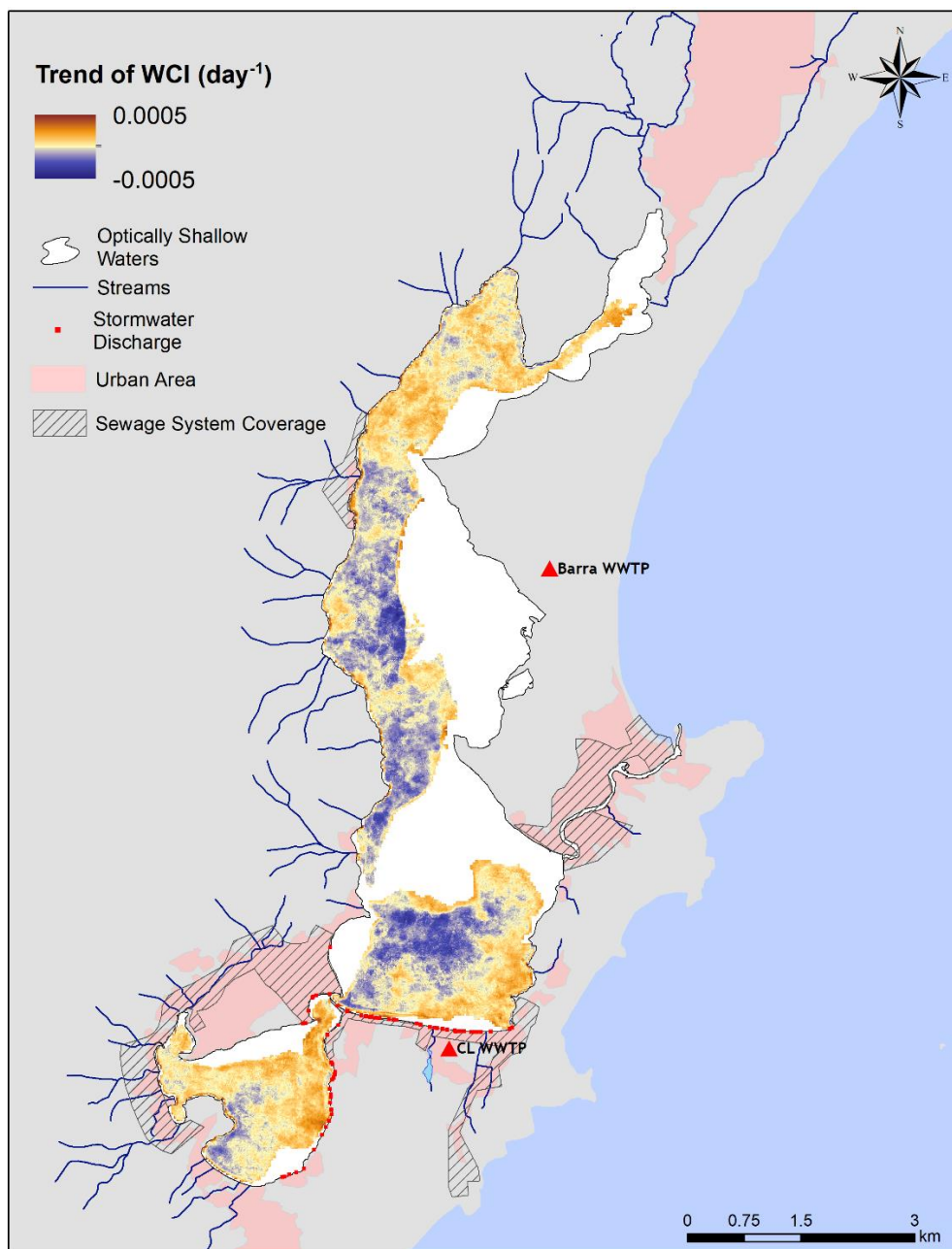
Figure 33: Linear trend of the WCI per day for the period between 2019 and 2021

In Figure 34 the trend of each IOP is presented. It is possible to observe a strong decrease of $b_{b\,spm}(440)$ throughout the whole lagoon, which indicates sedimentation of solids over time. This suggests that the regions with a positive trend for WCI are mostly influenced by the combination of the other IOPs $(k_d(PAR), a_{dg}(440)$ and $a_{chla}(440))$, which have positive trends in the same area and combined are able to surpass the negative trend of SPM.
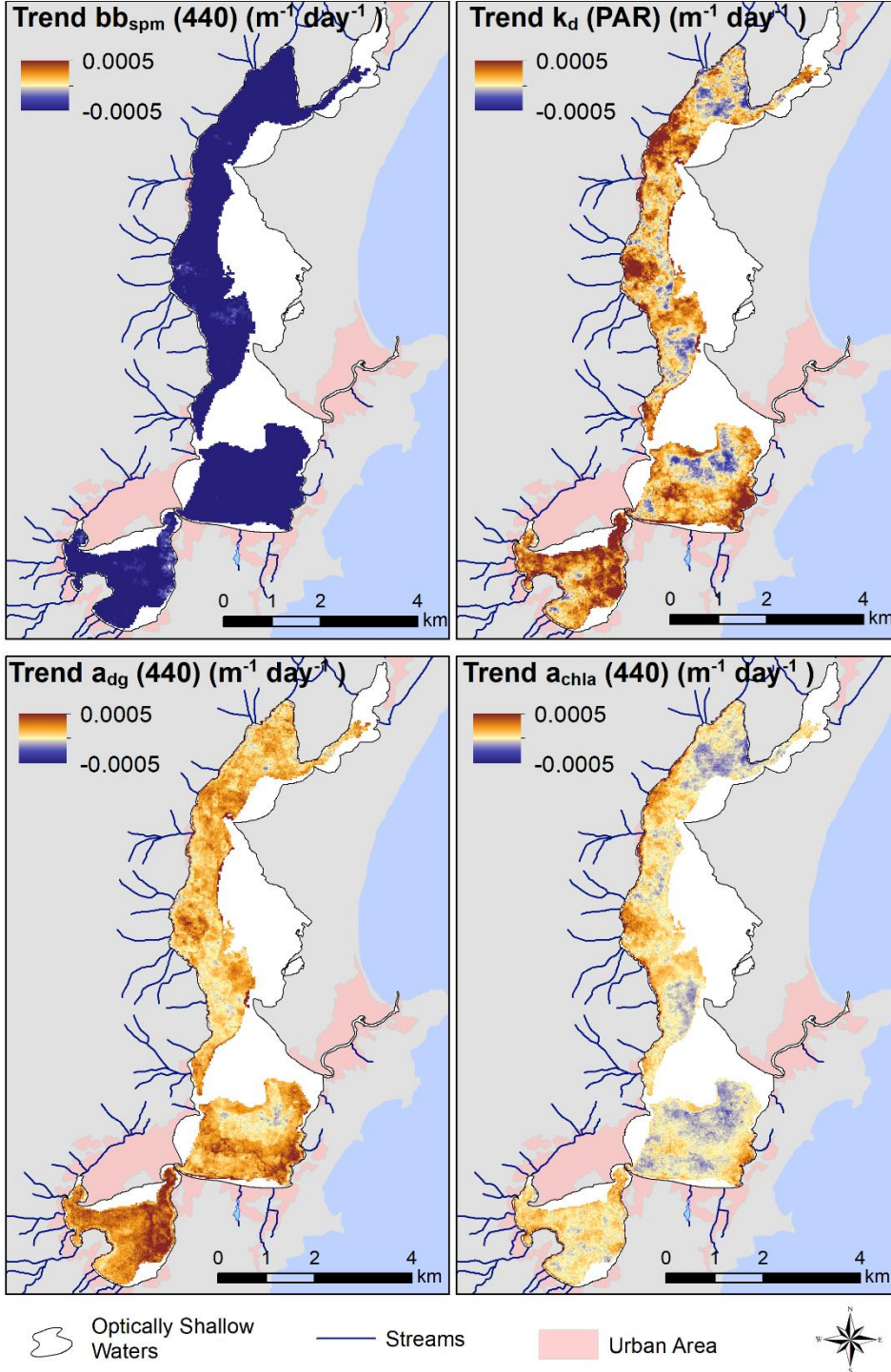
Figure 34: Linear trend of $k_d(PAR), b_{b\,spm}(440), a_{dg}(440)$ and $a_{chla}(440)$ per day for the period between 2019 and 2021

7. CONCLUSION AND RECOMMENDATIONS

With this study, the capabilities of optical remote sensing in the detection of wastewater outfalls in Conceição Lagoon were recognized. Even with certain constraints, it was possible to formulate a novel index from IOPs that captured spatial differences between wastewater plumes and ambient waters, and detected anomalous conditions across time, which was called Wastewater Contamination Index (WCI).

One of the constraints is related to the retrieval of Inherent Optical Properties (IOPs) in Conceição Lagoon. The IOPs were derived from Sentinel-2 imagery using the 2SeaColor model, and evaluation of the model performance showed poor agreement between in-situ measurements and model-derived variables. Possible reasons for it were associated with uncertain quality of the field measurements, reduced number of in-situ-satellite matchups, the optical complexity of the water and the sensitivity of the model. Analytical models, such as the 2SeaColor, have the forward model based on the exact solution of RTE and are more sensitive to noise, which can be caused by glint and errors in atmospheric correction (Sagan et al., 2020). Therefore, it was not possible to convert IOPs into concentration of water constituents. Nevertheless, a strong agreement between the 2SeaColor-derived IOPs and empirical models established in the literature applied to in-situ spectra gave us more confidence that the model is able to at least capture the main features expected of the IOPs and indicate the proportion of the fundamental water quality variables. Since the method is based on variability of IOPs and relative proportion between them, the 2SeaColor was considered acceptable for further use despite the mentioned limitations.

The proportion of optical signals associated with a wastewater plume was used to derive the WCI. It was shown that wastewater is mostly characterized by a high concentration of particulate matter and low light penetration, which are given a weight of approximately 40% each. Coloured dissolved organic matter and detritus have a secondary role in the description of the wastewater plume, with a weight of 15%, while chlorophyll-a has the lowest influence (8%). It should be noted that in this case only one plume was used as a reference to assess the relative weights of IOPs and it was assumed that it would be representative of other wastewater spills in the area. Ideally, a larger number of images portraying visible and confirmed wastewater plumes should be used to give statistical strength to the hypothesis, but it was not available in this case. Nonetheless, the application of the WCI to images of other suspected outfall events indicated the suitability of the index for wastewater detection. With the aid of photographic records, meteorological, water quality and hydrodynamics data, it was possible to find agreement between high WCI and four wastewater outfalls. Results indicated that wind could be an important factor in the observation of plumes, probably due to its importance to the lagoon's circulation and column mixing. Clouds, on the other hand, constitute a limitation of the method. The cloud mask from Sentinel-2 does not efficiently remove clouds and their shadows, and these harm the interpretation of WCI due to deviant signals. The spatio-temporal analysis of WCI did not provide significant recurrent patterns of wastewater pollution in the area, which highlights the irregular nature and unpredictability of wastewater outfalls.

In this context, the following recommendations are given for improvement of the method and future studies:
- Quality assured in-situ water quality measurements, including other pigments such as chlorophyll-b and fucoxanthin;
- Quality assured radiometric measurements: use of fixed sensors and viewing geometry, third radiance radiometer to capture sky radiance and allow correction for glint;

- Improvements to the Hydro-Optical model, including parametrization for other pigments and inclusion of bottom reflectance effects;

- Use of larger number of reference wastewater plumes to characterize the proportion of IOPs that best captures the wastewater signal;

- Evaluation of the WCI performance in other locations;

- Effective identification and masking of clouds and cloud shadows;

- Machine Learning to automate the process of wastewater detection. It should be noted that in this case, a large number of reference images of wastewater plumes would be required for training.

- Inclusion of shapes and other remote sensing features (i.e. radar, thermal) in the detection process.

REFERENCES

Arabi, B., Salama, M.S., van der Wal, D., Pitarch, J., Verhoef, W., 2020. The impact of sea bottom effects on the retrieval of water constituent concentrations from MERIS and OLCI images in shallow tidal waters supported by radiative transfer modeling. Remote Sens. Environ. 237, 111596. https://doi.org/10.1016/j.rse.2019.111596

Arabi, B., Salama, M.S., Wernand, M.R., Verhoef, W., 2018. Remote sensing of water constituent concentrations using time series of in-situ hyperspectral measurements in the Wadden Sea. Remote Sens. Environ. 216, 154–170. https://doi.org/10.1016/J.RSE.2018.06.040

Arabi, B., Salama, M.S., Wernand, M.R., Verhoef, W., 2016. MOD2SEA: A coupled atmosphere-hydro-optical model for the retrieval of chlorophyll-a from remote sensing observations in complex turbid waters. Remote Sens. 8, 722. https://doi.org/10.3390/rs8090722

ARESC, 2021. Monitoramento da Qualidade Hídrica da Lagoa da Conceição , município de Florianópolis [Monitoring of the Water Quality of Lagoa da Conceição, municipality of Florianópolis].

Ayad, M., Li, J., Holt, B., Lee, C., 2020. Analysis and Classification of Stormwater and Wastewater Runoff From the Tijuana River Using Remote Sensing Imagery. Front. Environ. Sci. 8, 599030. https://doi.org/10.3389/fenvs.2020.599030

Bernardo, N., Carmo, A., Rotta, L., Alcântara, E., 2020. Single tuned algorithm to estimate the SPM concentration in a cascade reservoir system using OLI/L8 images. Adv. Sp. Res. 66, 2583–2596. https://doi.org/10.1016/J.ASR.2020.08.035

Bierman, P., Lewis, M., Ostendorf, B., Tanner, J., 2011. A review of methods for analysing spatial and temporal patterns in coastal water quality. Ecol. Indic. 11, 103–114. https://doi.org/10.1016/J.ECOLIND.2009.11.001

Bjornsson, H., Venegas, S.A., 1997. A Manual for EOF and SVD Analyses of Climatic Data, Report No. 97-1.

Bondur, V.G., Vorobyev, V.E., Zamshin, V. V, Serebryany, A.N., Latushkin, A.A., Li, M.E., Martynov, O. V, Hurchak, A.P., Grinchenko, D. V, 2018. Monitoring Anthropogenic Impact on Some Coastal Water Areas of the Black Sea Using Multispectral Satellite Imagery 54, 3–22. https://doi.org/10.1134/S0001433818090098

Bondur, V.G., Zamshin, V. V., Zamshina, A.S., Vorobyev, V.E., 2020. Registering from Space the Features of Deep Wastewater Outfalls into Coastal Water Areas Due to Discharge Collector Breaks. Izv. - Atmos. Ocean Phys. 56, 979–988. https://doi.org/10.1134/S0001433820090066

Brezonik, P.L., Olmanson, L.G., Finlay, J.C., Bauer, M.E., 2015. Factors affecting the measurement of CDOM by remote sensing of optically complex inland waters. Remote Sens. Environ. 157, 199–215. https://doi.org/10.1016/J.RSE.2014.04.033

Bueso, D., Piles, M., Camps-Valls, G., 2020. Nonlinear PCA for Spatio-Temporal Analysis of Earth Observation Data. IEEE Trans. Geosci. Remote Sens. 58, 5752–5763. https://doi.org/10.1109/TGRS.2020.2969813

Burggraaff, O., 2020. Biases from incorrect reflectance convolution. Opt. Express, Vol. 28, Issue 9, pp. 13801-13816 28, 13801–13816. https://doi.org/10.1364/OE.391470

Busch, J.A., Hedley, J.D., Zielinski, O., 2013. Correction of hyperspectral reflectance measurements for surface objects and direct sun reflection on surface waters. http://dx.doi.org/10.1080/01431161.2013.804226 34, 6651–6667. https://doi.org/10.1080/01431161.2013.804226

Caballero, I., Fernández, R., Escalante, O.M., Mamán, L., Navarro, G., 2020. New capabilities of Sentinel-2A/B satellites combined with in situ data for monitoring small harmful algal blooms in complex coastal waters. Sci. Reports 2020 101 10, 1–14. https://doi.org/10.1038/s41598-020-65600-1

Cabral, A., Bercovich, M.V., Fonseca, A., 2019. Implications of poor-regulated wastewater treatment systems in the water quality and nutrient fluxes of a subtropical coastal lagoon. Reg. Stud. Mar. Sci. 29, 100672. https://doi.org/10.1016/j.rsma.2019.100672

CASAN, 2021. Projeto de Recuperação de Áreas Degradadas - PRAD Lagoa da Conceição-Florianópolis/SC [Degraded Area Recovery Program Lagoa da Conceição-Florianópolis/SC].

Cleveland, R.B., Cleveland, W.S., McRae, J.E., Terpenning, I., 1990. STL: A Seasonal-Trend Decomposition Procedure Based on Loess. J. Off. Stat. 6, 3–73. https://doi.org/10.1007/978-1-4613-4499-5_24

D'Sa, E.J., Miller, R.L., McKee, B.A., 2007. Suspended particulate matter dynamics in coastal waters from ocean color: Application to the northern Gulf of Mexico. Geophys. Res. Lett. 34, 23611. https://doi.org/10.1029/2007GL031192

Dall'Olmo, G., Gitelson, A.A., 2005. Effect of bio-optical parameter variability on the remote estimation of chlorophyll-a concentration in turbid productive waters: experimental results. Appl. Opt. Vol. 44, Issue 3, pp. 412-422 44, 412–422. https://doi.org/10.1364/AO.44.000412

de Barros, G., Larissa, A.D., Fonseca, O., Cabral dos Santos, A., Luiza Schmitz Fontes, M., Rodolfo Donnangelo Varela, A., Franco, D., 2017. Nutrient distribution in a shallow subtropical lagoon, south Brazil, subjected to seasonal hypoxic and anoxic events. Brazilian J. Oceanogr. 65, 116–127. https://doi.org/10.1590/S1679-87592017101206502

DiGiacomo, P.M., Washburn, L., Holt, B., Jones, B.H., 2004. Coastal pollution hazards in southern California observed by SAR imagery: Stormwater plumes, wastewater plumes, and natural hydrocarbon seeps. Mar. Pollut. Bull. 49, 1013–1024. https://doi.org/10.1016/j.marpolbul.2004.07.016

Doxaran, D., Froidefond, J.-M., Castaing, P., 2003. Remote-sensing reflectance of turbid sediment-dominated waters. Reduction of sediment type variations and changing illumination conditions effects by use of reflectance ratios. Appl. Opt. Vol. 42, Issue 15, pp. 2623-2634 42, 2623–2634. https://doi.org/10.1364/AO.42.002623

El Mahrad, B., Newton, A., Icely, J., Kacimi, I., Abalansa, S., Snoussi, M., 2020. Contribution of Remote Sensing Technologies to a Holistic Coastal and Marine Environmental Management Framework: A Review. Remote Sens. 12, 2313. https://doi.org/10.3390/rs12142313

Ficek, D., Zapadka, T., Dera, J., 2011. Remote sensing reflectance of Pomeranian lakes and the Baltic. Oceanologia 53, 959–970. https://doi.org/10.5697/OC.53-4.959

Fontes, M.L.S., Suzuki, M.T., Cottrell, M.T., Abreu, P.C., 2010. Primary Production in a Subtropical Stratified Coastal Lagoon—Contribution of Anoxygenic Phototrophic Bacteria. Microb. Ecol. 2010 611 61, 223–237. https://doi.org/10.1007/S00248-010-9739-X

Fraschetti, S., Gambi, C., Giangrande, A., Musco, L., Terlizzi, A., Danovaro, R., 2006. Structural and functional response of meiofauna rocky assemblages to sewage pollution. Mar. Pollut. Bull. 52, 540–548. https://doi.org/10.1016/j.marpolbul.2005.10.001

Frontier, S., 1976. Étude de la décroissance des valeurs propres dans une analyse en composantes principales: Comparaison avec le moddle du bâton brisé. J. Exp. Mar. Bio. Ecol. 25, 67–75. https://doi.org/10.1016/0022-0981(76)90076-9

Gancheva, I., Campbell, G., Peneva, E., 2020. Satellite remote sensing techniques for detection of riverine and other sources flows in the coastal part of the Black Sea, in: EGU General Assembly. Online. https://doi.org/https://doi.org/10.5194/egusphere-egu2020-8336

Gernez, P., Barillé, L., Lerouxel, A., Mazeran, C., Lucas, A., Doxaran, D., 2014. Remote sensing of suspended particulate matter in turbid oyster-farming ecosystems. J. Geophys. Res. Ocean. 119, 7277–7294. https://doi.org/10.1002/2014JC010055

Gierach, M.M., Holt, B., Trinh, R., Jack Pan, B., Rains, C., 2017. Satellite detection of wastewater diversion plumes in Southern California. Estuar. Coast. Shelf Sci. 186, 171–182. https://doi.org/10.1016/j.ecss.2016.10.012

Groetsch, P.M.M., Gege, P., Simis, S.G.H., Eleveld, M.A., Peters, S.W.M., 2017. Validation of a spectral correction procedure for sun and sky reflections in above-water reflectance measurements. Opt. Express 25, A742. https://doi.org/10.1364/oe.25.00a742

Groom, S., Sathyendranath, S., Ban, Y., Bernard, S., Brewin, R., Brotas, V., Brockmann, C., Chauhan, P., Choi, J., Chuprin, A., Ciavatta, S., Cipollini, P., Donlon, C., Franz, B., He, X., Hirata, T., Jackson, T., Kampel, M., Krasemann, H., Lavender, S., Pardo-Martinez, S., Mélin, F., Platt, T., Santoleri, R., Skakala, J., Schaeffer, B., Smith, M., Steinmetz, F., Valente, A., Wang, M., 2019. Satellite Ocean Colour: Current Status and Future Perspective. Front. Mar. Sci. 0, 485. https://doi.org/10.3389/FMARS.2019.00485

Guo, B., Fang, Y., Jin, X., Zhou, Y., 2020. Monitoring the effects of land consolidation on the ecological environmental quality based on remote sensing: A case study of Chaohu Lake Basin, China. Land use policy 95, 104569. https://doi.org/10.1016/J.LANDUSEPOL.2020.104569

Hafeez, S., Sing Wong, M., Abbas, S., Y. T. Kwok, C., Nichol, J., Ho Lee, K., Tang, D., Pun, L., 2019.

Detection and Monitoring of Marine Pollution Using Remote Sensing Technologies, in: Fouzia, H.B. (Ed.), Monitoring of Marine Pollution. IntechOpen. https://doi.org/10.5772/intechopen.81657

Hannachi, A., Jolliffe, I.T., Stephenson, D.B., 2007. Empirical orthogonal functions and related techniques in atmospheric science: A review. Int. J. Climatol. 27, 1119–1152. https://doi.org/10.1002/JOC.1499

Harringmeyer, J.P., Kaiser, K., Thompson, D.R., Gierach, M.M., Cash, C.L., Fichot, C.G., 2021. Detection and Sourcing of CDOM in Urban Coastal Waters With UV-Visible Imaging Spectroscopy. Front. Environ. Sci. 9, 1–21. https://doi.org/10.3389/fenvs.2021.647966

Horn, L.R., 2021. Caracterização do comportamento da concentração de clorofila-a em uma laguna costeira, com o uso de modelos bio-ópticos de sensoriamento remoto [Characterization of the behavior of chlorophyll-a concentration in a coastal lagoon using remote sensing bio-o. Universidade Federal de Santa Catarina - UFSC.

Hu, X., Xu, H., 2019. A new remote sensing index based on the pressure-state-response framework to assess regional ecological change. Environ. Sci. Pollut. Res. 26, 5381–5393. https://doi.org/10.1007/S11356-018-3948-0/FIGURES/7

Hummel, M.A., Berry, M.S., Stacey, M.T., 2018. Sea Level Rise Impacts on Wastewater Treatment Systems Along the U.S. Coasts. Earth's Futur. 6, 622–633. https://doi.org/10.1002/2017EF000805

ICES-BID, 2015. Crescimento Urbano de Florianópolis - Relatório Final - Estudo 3 [Florianópolis Urban Growth - Final Report - Study 3] 441.

Ingebritsen, S.E., Lyon, R.J., 1985. Principal components analysis of multitemporal image pairs. Int. J. Remote Sens. 6, 687–696. https://doi.org/10.1080/01431168508948491

IOCCG, 2000. Remote Sensing of Ocean Colour in Coastal, and Other Optically-Complex, Waters.

IOCCG Protocol Series, 2019. Protocols for Satellite Ocean Colour Data Validation: In Situ Optical Radiometry., in: Zibordi, G., Voss, K.J., Johnson, B.C., Mueller, J.L. (Eds.), Ocean Optics and Biogeochemistry Protocols for Satellite Ocean Colour Sensor Validation, Volume 3.0. International Ocean Colour Coordinating Group (IOCCG), Dartmouth, NS, Canada. https://doi.org/10.25607/OBP-691

IPCC, 2018. Global Warming of 1.5°C. An IPCC Special Report on the impacts of global warming of 1.5°C above pre-industrial levels and related global greenhouse gas emission pathways, in the context of strengthening the global response to the threat of climate change,.

Jawson, S.D., Niemann, J.D., 2007. Spatial patterns from EOF analysis of soil moisture at a large scale and their dependence on soil, land-use, and topographic properties. Adv. Water Resour. 30, 366–381. https://doi.org/10.1016/J.ADVWATRES.2006.05.006

Jolliffe, I.T., 2002. Principal Component Analysis, 2nd ed, Springer Series in Statistics. Springer, New York. https://doi.org/10.1007/B98835

Kirk, J.T.O., 1994. Light and Photosynthesis in Aquatic Ecosystems, 2nd ed. Cambridge University Press.

Koehler, J., Kuenzer, C., 2020. Forecasting Spatio-Temporal Dynamics on the Land Surface Using Earth Observation Data—A Review. Remote Sens. 2020, Vol. 12, Page 3513 12, 3513. https://doi.org/10.3390/RS12213513

Kopelevich, O. V., 1983. Small-parameter model of optical properties of sea waters. Ocean Opt. 1, 208–234.

Kratzer, S., Therese Harvey, E., Philipson, P., 2014. The use of ocean color remote sensing in integrated coastal zone management-A case study from Himmerfjärden, Sweden. Mar. Policy 43, 29–39. https://doi.org/10.1016/j.marpol.2013.03.023

Krestenitis, M., Orfanidis, G., Ioannidis, K., Avgerinakis, K., Vrochidis, S., Kompatsiaris, I., 2019. Oil Spill Identification from Satellite Images Using Deep Neural Networks. Remote Sens. 2019, Vol. 11, Page 1762 11, 1762. https://doi.org/10.3390/RS11151762

Kuiper, J., 1978. A Survey and Comparative Analysis of Various Methods of Seasonal Adjustment, in: Zellner, A. (Ed.), Seasonal Analysis of Economic Time Series. NBER, pp. 59–94.

Kutser, T., Vahtmäe, E., Paavel, B., Kauer, T., 2013. Removing glint effects from field radiometry data measured in optically complex coastal and inland waters. Remote Sens. Environ. 133, 85–89. https://doi.org/10.1016/J.RSE.2013.02.011

Kutser, T., Vahtmäe, E., Praks, J., 2009. A sun glint correction method for hyperspectral imagery containing areas with non-negligible water leaving NIR signal. Remote Sens. Environ. 113, 2267–2274. https://doi.org/10.1016/J.RSE.2009.06.016

Lee, Z., Carder, K.L., Mobley, C.D., Steward, R.G., Patch, J.S., 1999. Hyperspectral remote sensing for shallow waters: 2. Deriving bottom depths and water properties by optimization.

Letelier, R.M., Abbott, M.R., 1996. An analysis of chlorophyll fluorescence algorithms for the moderate resolution imaging spectrometer (MODIS). Remote Sens. Environ. 58, 215–223. https://doi.org/10.1016/S0034-4257(96)00073-9

Liang, S., Li, X., Wang, J. (Eds.), 2012. Chapter 22 - High-level Land Product Integration Methods, in: Advanced Remote Sensing. Academic Press, Boston, pp. 667–690. https://doi.org/https://doi.org/10.1016/B978-0-12-385954-9.00022-8

Lisboa, L.K., Teive, L.F., Petrucio, M.M., 2008. Lagoa da Conceição: uma revisão da disponibilidade de dados ecológicos visando o direcionamento de novas pesquisas no ecossistema. Rev. Biotemas 21, 139–146.

Loisel, H., Mangin, A., Vantrepotte, V., Dessailly, D., Ngoc Dinh, D., Garnesson, P., Ouillon, S., Lefebvre, J.P., Mériaux, X., Minh Phan, T., 2014. Variability of suspended particulate matter concentration in coastal waters under the Mekong's influence from ocean color (MERIS) remote sensing over the last decade. Remote Sens. Environ. 150, 218–230. https://doi.org/10.1016/j.rse.2014.05.006

Lopez y Royo, C., Silvestri, C., Pergent, G., Casazza, G., 2009. Assessing human-induced pressures on coastal areas with publicly available data. J. Environ. Manage. 90, 1494–1501. https://doi.org/10.1016/j.jenvman.2008.10.007

Lüchmann, K.H., Freire, A.S., Ferreira, N.C., Daura-Jorge, F.G., Marques, M.R.F., 2008. Spatial and temporal variations in abundance and biomass of penaeid shrimps in the subtropical Conceição Lagoon, southern Brazil. J. Mar. Biol. Assoc. United Kingdom 88, 293–299. https://doi.org/10.1017/S0025315408000556

Machado-Machado, E.A., Neeti, N., Eastman, J.R., Chen, H., 2011. Implications of space-time orientation for Principal Components Analysis of Earth observation image time series. Earth Sci. Informatics 4, 117–124. https://doi.org/10.1007/S12145-011-0082-7/FIGURES/4

Mahapatro, D., Panigrahy, R.C., Panda, S., 2013. Coastal Lagoon: Present Status and Future Challenges. Int. J. Mar. Sci. https://doi.org/10.5376/IJMS.2013.03.0023

Mannino, A., Russ, M.E., Hooker, S.B., 2008. Algorithm development and validation for satellite-derived distributions of DOC and CDOM in the U.S. Middle Atlantic Bight. J. Geophys. Res. Ocean. 113, 7051. https://doi.org/10.1029/2007JC004493

Marmorino, G.O., Smith, G.B., Miller, W.D., Bowles, J.H., 2010. Detection of a buoyant coastal wastewater discharge using airborne hyperspectral and infrared imagery. J. Appl. Remote Sens. 4, 043502. https://doi.org/10.1117/1.3302630

Martini, L.C.P., Mattos, D.S., Barbosa, D.F.P., Rech, A.I.B., 2006. Uso de sensoriamento remoto orbital para avaliação da distribUição espacial de clorofila_a na lagoa da conceição-florianópolis, sc Use of orbital remote sensing in the assessment of spatial distribUtion of Chlorophyll_a in lagoa da ConCeição-florianópolis.

Mascaro, G., Vivoni, E.R., Méndez-Barroso, L.A., 2015. Hyperresolution hydrologic modeling in a regional watershed and its interpretation using empirical orthogonal functions. Adv. Water Resour. 83, 190–206. https://doi.org/10.1016/j.advwatres.2015.05.023

Matthews, M.W., Bernard, S., Robertson, L., 2012. An algorithm for detecting trophic status (chlorophyll-a), cyanobacterial-dominance, surface scums and floating vegetation in inland and coastal waters. Remote Sens. Environ. 124, 637–652. https://doi.org/10.1016/J.RSE.2012.05.032

Menken, K.D., Brezonik, P.L., Bauer, M.E., 2009. Influence of Chlorophyll and Colored Dissolved Organic Matter (CDOM) on Lake Reflectance Spectra: Implications for Measuring Lake Properties by Remote Sensing. http://dx.doi.org/10.1080/07438140609353895 22, 179–190. https://doi.org/10.1080/07438140609353895

Mishra, D.R., Mishra, S., 2010. Plume and bloom: effect of the Mississippi River diversion on the water quality of Lake Pontchartrain. http://dx.doi.org/10.1080/10106041003763394 25, 555–568. https://doi.org/10.1080/10106041003763394

Mishra, S., Mishra, D.R., 2012. Normalized difference chlorophyll index: A novel model for remote estimation of chlorophyll-a concentration in turbid productive waters. Remote Sens. Environ. 117, 394–406. https://doi.org/10.1016/J.RSE.2011.10.016

Mobley, C.D., 1999. Estimation of the remote-sensing reflectance from above-surface measurements. Appl. Opt. Vol. 38, Issue 36, pp. 7442-7455 38, 7442–7455. https://doi.org/10.1364/AO.38.007442

Mobley, C.D., 1994. Light and water: radiative transfer in natural waters. Academic Press.

Navarro, G., Ruiz, J., 2006. Spatial and temporal variability of phytoplankton in the Gulf of Cádiz through remote sensing images. Deep. Res. Part II Top. Stud. Oceanogr. 53, 1241–1260.

https://doi.org/10.1016/J.DSR2.2006.04.014

Nechad, B., Ruddick, K.G., Park, Y., 2010. Calibration and validation of a generic multisensor algorithm for mapping of total suspended matter in turbid waters. Remote Sens. Environ. 114, 854–866. https://doi.org/10.1016/J.RSE.2009.11.022

Neeti, N., Eastman, R.J., 2014. Novel approaches in Extended Principal Component Analysis to compare spatio-temporal patterns among multiple image time series. Remote Sens. Environ. 148, 84–96. https://doi.org/10.1016/J.RSE.2014.03.015

Nezlin, N.P., DiGiacomo, P.M., 2005. Satellite ocean color observations of stormwater runoff plumes along the San Pedro Shelf (southern California) during 1997–2003. Cont. Shelf Res. 25, 1692–1711. https://doi.org/10.1016/J.CSR.2005.05.001

Nezlin, N.P., DiGiacomo, P.M., Diehl, D.W., Jones, B.H., Johnson, S.C., Mengel, M.J., Reifel, K.M., Warrick, J.A., Wang, M., 2008. Stormwater plume detection by MODIS imagery in the southern California coastal ocean. Estuar. Coast. Shelf Sci. 80, 141–152. https://doi.org/10.1016/j.ecss.2008.07.012

Normandin, C., Lubac, B., Sottolichio, A., Frappart, F., Ygorra, B., Marieu, V., 2019. Analysis of Suspended Sediment Variability in a Large Highly Turbid Estuary Using a 5-Year-Long Remotely Sensed Data Archive at High Resolution. J. Geophys. Res. Ocean. 124, 7661–7682. https://doi.org/10.1029/2019JC015417

Odreski, F., Curtarelli, M.P., Berns, G.A.G., 2021. Estudo técnico de suporte para recuperação ambiental da Lagoa da Conceição [Technical study for supporting the environmental recovery of Conceição Lagoon]. Florianópolis/SC.

Odreski, L.F.R., 2012. Influência Hidrológica nos Processos Hidrodinâmicos da Lagoa da Conceição, Florianópolis/SC [Hydrological Influence in the Hydrodynamic Processes of Conceição Lagoon, Florianópolis/SC]. MSc Thesis. Federal University of Santa Catarina.

Porto Filho, E., 1993. Sedimentometria e algumas considerações sobre a biogeoquimica dos sedimentos de fundo da Lagoa da Conceição, Ilha de Santa Catarina [Sedimentometry and some considerations on the biogeochemistry of the bottom sediments of Lagoa da Conceição, Santa Catarin. Universidade Federal de Santa Catarina.

Raj, M. V, 2013. Water quality Parameters and it influences in the Ennore estuary and near Coastal Environment with respect to Industrial and Domestic sewage, Int. Res. J. Environment Sci. International Science Congress Association.

Roundy, P.E., 2015. On the Interpretation of EOF Analysis of ENSO, Atmospheric Kelvin Waves, and the MJO. J. Clim. 28, 1148–1165. https://doi.org/10.1175/JCLI-D-14-00398.1

Ruddick, K.G., Voss, K., Banks, A.C., Boss, E., Castagna, A., Frouin, R., Hieronymi, M., Jamet, C., Johnson, B.C., Kuusk, J., Lee, Z., Ondrusek, M., Vabson, V., Vendt, R., 2019. A Review of Protocols for Fiducial Reference Measurements of Downwelling Irradiance for the Validation of Satellite Remote Sensing Data over Water. Remote Sens. 2019, Vol. 11, Page 1742 11, 1742. https://doi.org/10.3390/RS11151742

Sagan, V., Peterson, K.T., Maimaitijiang, M., Sidike, P., Sloan, J., Greeling, B.A., Maalouf, S., Adams, C., 2020. Monitoring inland water quality using remote sensing: potential and limitations of spectral indices, bio-optical simulations, machine learning, and cloud computing. Earth-Science Rev. 205, 103187. https://doi.org/10.1016/J.EARSCIREV.2020.103187

Salama, M.S., Verhoef, W., 2015. Two-stream remote sensing model for water quality mapping: 2SeaColor. Remote Sens. Environ. 157, 111–122. https://doi.org/10.1016/j.rse.2014.07.022

Seegers, B.N., Teel, E.N., Kudela, R.M., Caron, D.A., Jones, B.H., 2017. Glider and remote sensing observations of the upper ocean response to an extended shallow coastal diversion of wastewater effluent. Estuar. Coast. Shelf Sci. 186, 198–208. https://doi.org/10.1016/J.ECSS.2016.06.019

Shiskin, J., Young, A.H., Musgrave, J.C., 1967. The X-11 variant of the census method II seasonal adjustment program.

Silva, J.C., 2013. Análise Numérica da Influência Dos Aportes Fluviais e Antrópicos Sobre a Hidrodinâmica Residual e a Qualidade da Água da Lagoa da Conceição – Florianópolis - SC [Numerical Analysis of the Influence of River and Anthropic Inputs on Residual Hydrodynamics a. Federal University of Santa Catarina.

Silva, V.E.C., 2016. Space-time analysis of the trophic state of a subtropical coastal lagoon: Lagoa da Conceição, Florianópolis, Santa Catarina. Federal University of Santa Catarina.

Silva, V.E.C., Franco, D., Larissa Fonseca, A., Luiza Fontes, M., Rodolfo Donnangelo, A., 2017. Space time evolution of the trophic state of a subtropical lagoon: Lagoa da Conceição, Florianópolis Island

of Santa Catarina, Brazil. Brazilian J. Water Resour. 22. https://doi.org/10.1590/2318-0331.011716027

Tippett, M.K., L'Heureux, M.L., 2020. Low-dimensional representations of Niño 3.4 evolution and the spring persistence barrier. npj Clim. Atmos. Sci. 2020 31 3, 1–11. https://doi.org/10.1038/s41612-020-0128-y

Toming, K., Kutser, T., Laas, A., Sepp, M., Paavel, B., Nõges, T., 2016. First Experiences in Mapping Lake Water Quality Parameters with Sentinel-2 MSI Imagery. Remote Sens. 2016, Vol. 8, Page 640 8, 640. https://doi.org/10.3390/RS8080640

Trinh, R.C., Fichot, C.G., Gierach, M.M., Holt, B., Malakar, N.K., Hulley, G., Smith, J., 2017. Application of Landsat 8 for monitoring impacts of wastewater discharge on coastal water quality. Front. Mar. Sci. 4, 329. https://doi.org/10.3389/fmars.2017.00329

Turner, R. K., 2015. Introduction, in: Turner, R. Kerry, Schaafsma, M. (Eds.), Coastal Zones Ecosystem Services. Studies in Ecological Economics. Springer, Norwich, UK, pp. 1–7. https://doi.org/10.1007/978-3-319-17214-9_1

UFSC, 2021. NOTA TÉCNICA Nº03/PES/2021 [Technical Note on mortality of organisms and rotten smell in Lagoa da Conceição].

UFSC, 2020. Nota Técnica sobre a situação da Lagoa da Conceição [Technical Report on the situation of Conceição Lagoon]. Florianopolis.

Vanhellemont, Q., 2019. Adaptation of the dark spectrum fitting atmospheric correction for aquatic applications of the Landsat and Sentinel-2 archives. Remote Sens. Environ. 225, 175–192. https://doi.org/10.1016/J.RSE.2019.03.010

West, M., 1997. Time series decomposition. Biometrika 84, 489–494. https://doi.org/10.1093/BIOMET/84.2.489

Xia, J., Yang, C., Li, Q., 2018. Building a spatiotemporal index for Earth Observation Big Data. Int. J. Appl. Earth Obs. Geoinf. 73, 245–252. https://doi.org/10.1016/J.JAG.2018.04.012

Yacobi, Y.Z., Köhler, J., Leunert, F., Gitelson, A., 2015. Phycocyanin-specific absorption coefficient: Eliminating the effect of chlorophylls absorption. Limnol. Oceanogr. Methods 13, 157–168. https://doi.org/10.1002/LOM3.10015

Yu, T., Jiapaer, G., Bao, A., Zheng, G., Jiang, L., Yuan, Y., Huang, X., 2021. Using synthetic remote sensing indicators to monitor the land degradation in a salinized area. Remote Sens. 13, 2851. https://doi.org/10.3390/RS13152851/S1

Yu, X., Salama, M.S., Shen, F., Verhoef, W., 2016. Retrieval of the diffuse attenuation coefficient from GOCI images using the 2SeaColor model: A case study in the Yangtze Estuary. Remote Sens. Environ. 175, 109–119. https://doi.org/10.1016/J.RSE.2015.12.053

APPENDICES

APPENDIX A – FIELDWORK SAMPLING PROCEDURES

The sampling procedures started before going to the field, with the preparation of the equipment. This included:

1. Preparing water sampling bottles:

   a. Add tags with the date and name of the points;

   b. Wrap bottles for chlorophyll-a analysis with aluminum foil (to avoid light interaction);

   c. Place them in a cool box.

2. Configuring the TriOS software (MSDA_XE):

   a. Add external trigger for all instruments and enable automatic measurement ('auto');

   b. Select saving of Calibrated and Raw files

   c. Select saving as File and on Database

   d. Select saving folder according to the date

In the field, the sampling logistics involved the use of a motorized boat as a means of transportation, which was harbored in a Marina located at the entrance of the Barra Channel (see Figure 3). Each day of measurement the equipment was prepared there: connection of the sensors to the logger and computer, connection of the logger to the power supply and mounting of the irradiance sensor onto a vertical metallic bar on the boat (see Figure 35). The next step was to move to the sampling locations, with the general strategy of alternating between starting at P1 in the South Lagoon and starting at P10 in Central Lagoon, aiming to cover as many points as possible during the available time (maximum 1h before and after overpass).

a)   b)

Figure 35: a) Boat used for the field measurements at the Marina and its b) Deck layout.

The procedure for performing the measurements at each sampling point can be summarized in the following steps:

1. Go to the specified sampling point without going with the boat over the point (to avoid turbulence and mixing);

2. Drop the anchor and get stable;

3. Note down in the Recording Sheet (APPENDIX C):

    a. Point number

    b. GPS coordinates

    c. Time

    d. Weather conditions

    e. Wind speed and direction

    f. Water aspect

4. Check TriOS software (MSDA_XE) configurations:

    a. Turn off the continuous measurement of CDOM, re-configure external trigger and automatic measurement ('auto');

    b. Select saving folder according to the sampling point;

    c. Select integration time for radiance and irradiance radiometers. In this case, it was left on 'auto' for automatic selection according to illumination conditions.

5. Do radiometric and fluorometer measurements with the following arrangement:

    a. <u>Downwelling Irradiance radiometer (Ed):</u> should be placed looking upwards, with no interference of parts of the boat in the field of view. In this case, mounted on a vertical bar on the boat (see Figure 36)

    b. <u>Water Leaving Radiance radiometer (Lw):</u> stand with the back to the sun, turn 90 degrees to one of the sides, trying to find the best spot without shadows and sun glint. Point the radiometer to the water at an angle between 40-45 degrees from nadir.

    c. <u>CDOM fluorometer:</u> place it underwater, approximately 15 cm depth.

When everything is ready, hit the trigger and wait for the measurement to finish (purple signal). Repeat this three times at least.
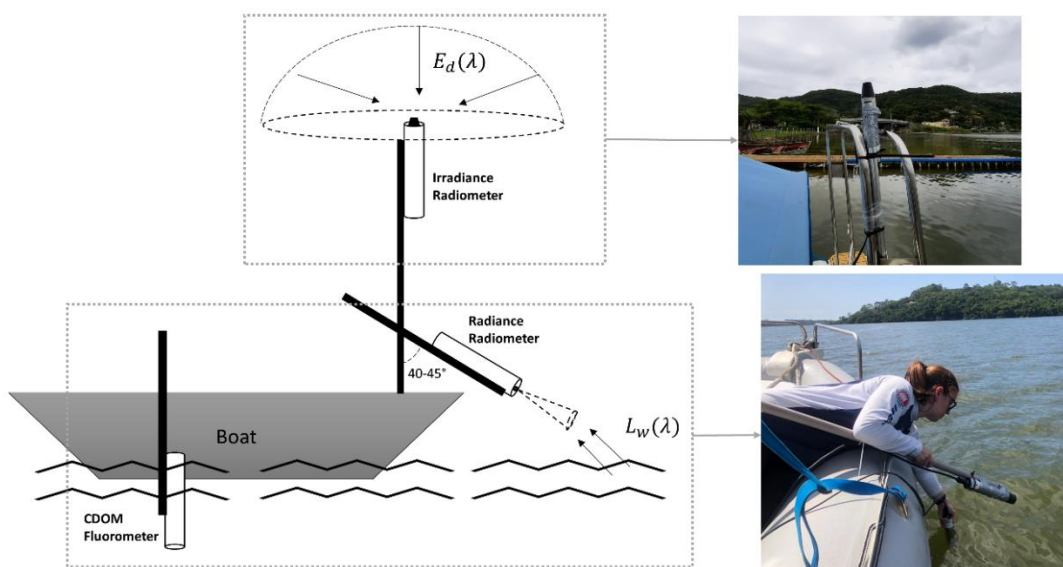
Figure 36: Layout configuration for radiometric and fluorometer measurements

6. Collect water samples (Figure 37 a)):

   a. Get the 3 bottles (one for each laboratory analysis) labeled with the according sampling point;

   b. Collect water from the surface with the inox jar, discard it once and collect it again;

   c. Fill the sampling bottles;

   d. Place bottles in the cool box.

7. Do CTD measurements (Figure 37 b)):

   a. Lower the device with a cable until it reaches the bottom and bring it back to the surface;

   b. Note down the depth and water surface temperature in the Recording Sheet.

8. Get everything settled and move to the next point.

a)   b)

Figure 37: a) Water sample collection. b) CTD measurement

Once all the field measurements of the day were completed, the boat returned to the Marina and the water samples were directly transported in the cool box to the laboratory for analysis.

APPENDIX B – SAMPLE FIELDWORK RECORDING SHEET

FIELDWORK RECORDING SHEET

MSc Research Amanda de Liz Arcari – a.delizarcari@student.utwente.nl

www.itc.nl

I. Basic Information

Date:	
Time:	
Point Number:	
GPS Coordinates Lat: Long:	

II. Conditions

Cloud Coverage:	
Rain:	
Wind:	
Temperature:	
Water aspect:	

III. Measurements Checklist

☐ Radiometric + CDOM

☐ Water Sample

☐ Secchi depth

IV. Notes

APPENDIX C – OVERALL CONDITIONS DURING FIELDWORK

The following sections describe in general the behavior of the sky conditions and water quality parameters measured during the Field Campaigns. The last section presents the compiled water quality results for consultation.

a) Sky Conditions

The sky-sun downwelling irradiance (E_d) measurements from each Field Campaign (FC) day were analyzed to evaluate the variability of the illumination conditions. Table 10 shows the sky condition and the respective average values of measured E_d and its range (min to max) for each day of measurement.
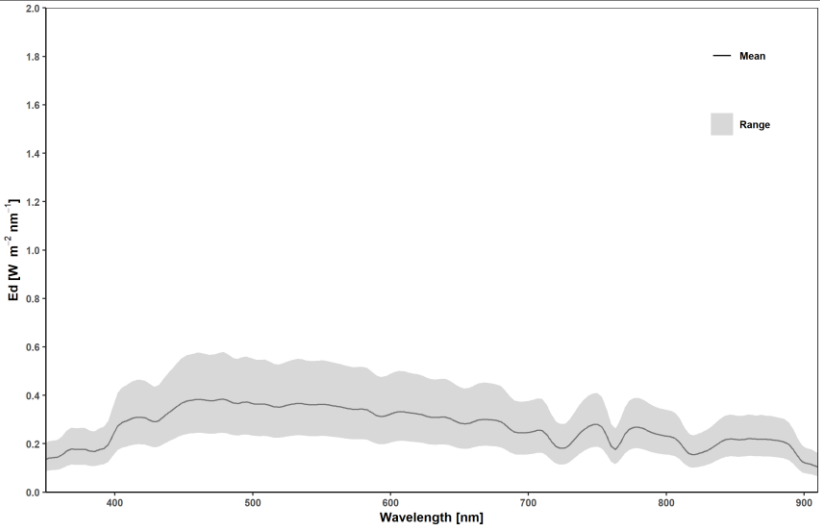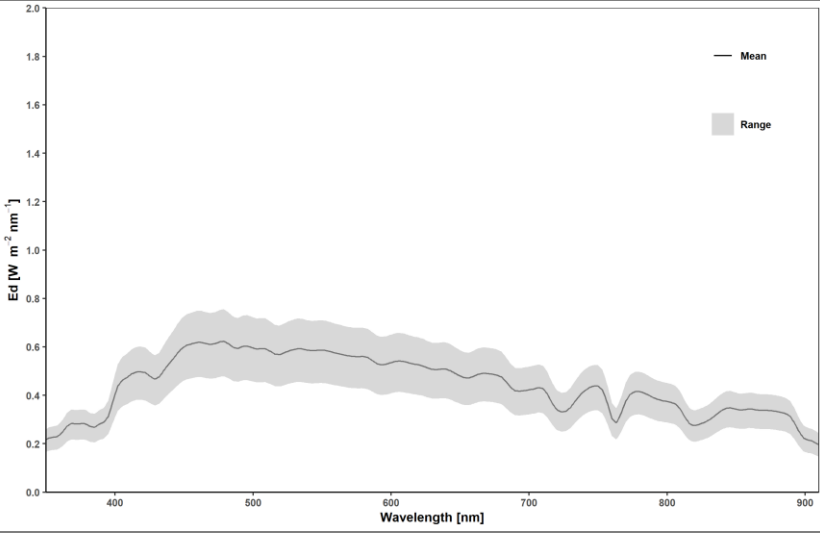
It can be observed that during FC 01 and 02, when the sky condition was completely overcast, E_d spectra were relatively low, with the average value reaching a maximum of 0.6 W m^{-2} nm^{-1} at around 450 nm. The variability within the measurements on those days was also low, as the range was less than 0.4 W m^{-2} nm^{-1}.

On the day of FC 03 it was partly cloudy, with a few openings. As expected, E_d average values were higher than the overcast days, reaching a maximum of 1.1 W m^{-2} nm^{-1} at around 450 nm. The range was also broader. For example, at 450 nm the minimum E_d was around 0.5 W m^{-2} nm^{-1} and the maximum 1.8 W m^{-2} nm^{-1}.

From FC 04 to FC 07 the conditions were very similar, with mostly clear skies and high scattered clouds. The average E_d spectrum measured on those days was higher than on the previous ones, reaching a maximum of 1.5 W m^{-2} nm^{-1} at around 450 nm. The ranges were broader than on the overcast days, with the maximum variability happening on FC 07, with similar values to FC 03.

It should be noted that the variability of the E_d spectra measurements for each day is influenced by the time and duration of the campaign, as the Solar Zenith Angle (SZA) will change and therefore the amount of direct irradiance (Ruddick et al., 2019). The higher variability on FC 03 and FC 07 could be explained by their longer duration (2:43 and 1:58 respectively) when the SZA also varied more: 72° to 37° on FC 03 and 75° to 50° on FC 07.

Table 10: Sky condition with the respective average irradiance values and range (min, max) for each Field Campaign (FC)

FC	Sky Condition	Irradiance
01	Overcast	
02	Overcast	
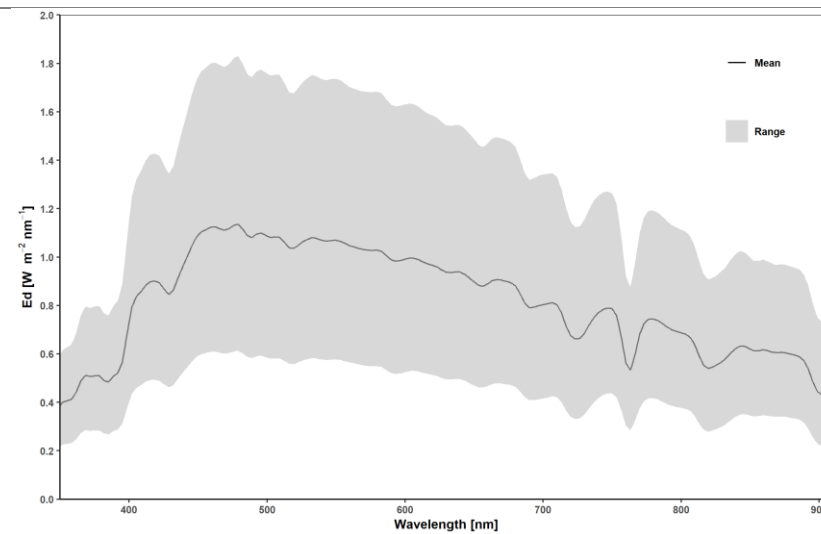
| 03 | Partly Cloudy | | |
| 04 | Mostly Clear | | |

| 05 | Mostly Clear | | |
| 06 | Mostly Clear | | |

| 07 | Mostly Clear | | |
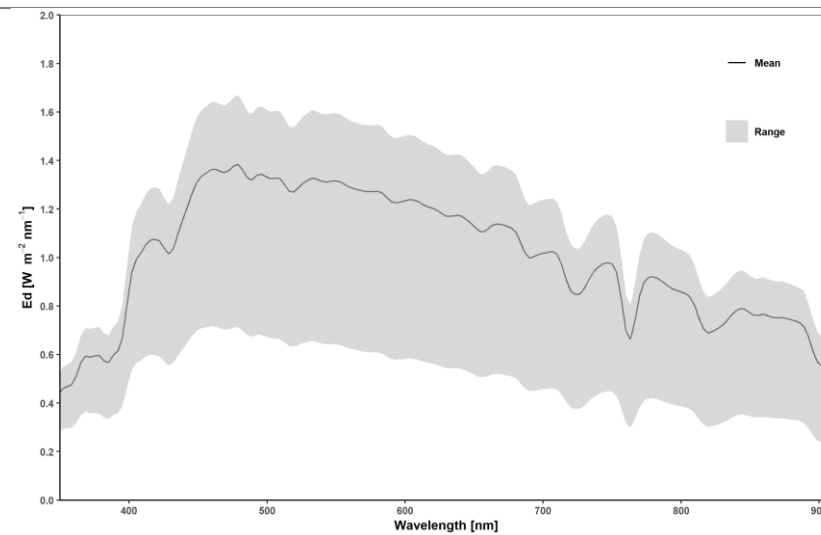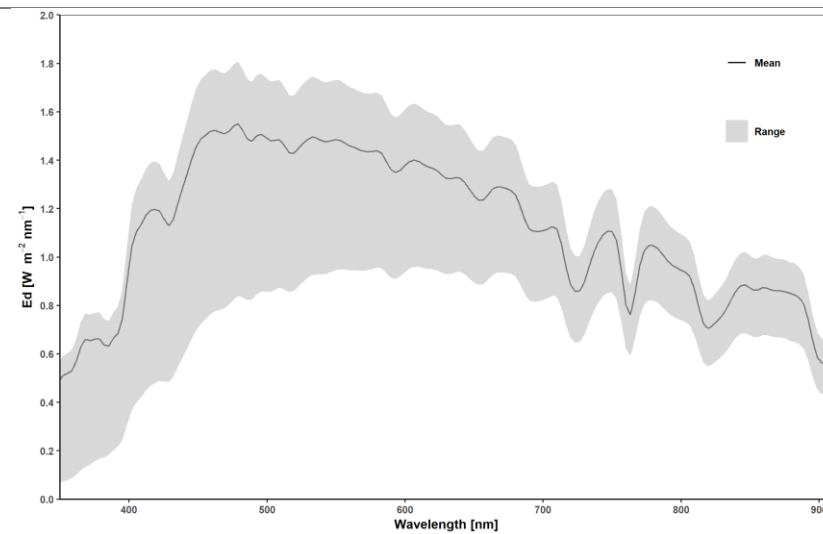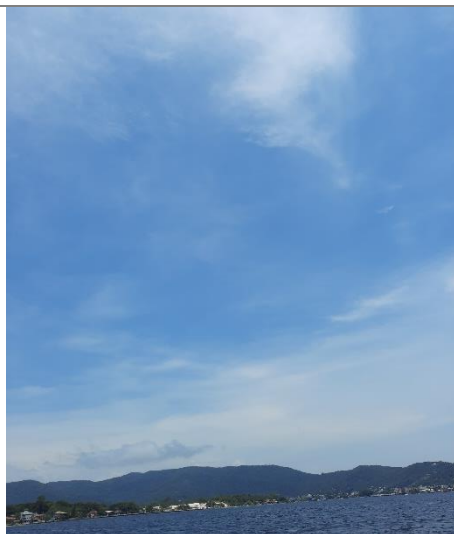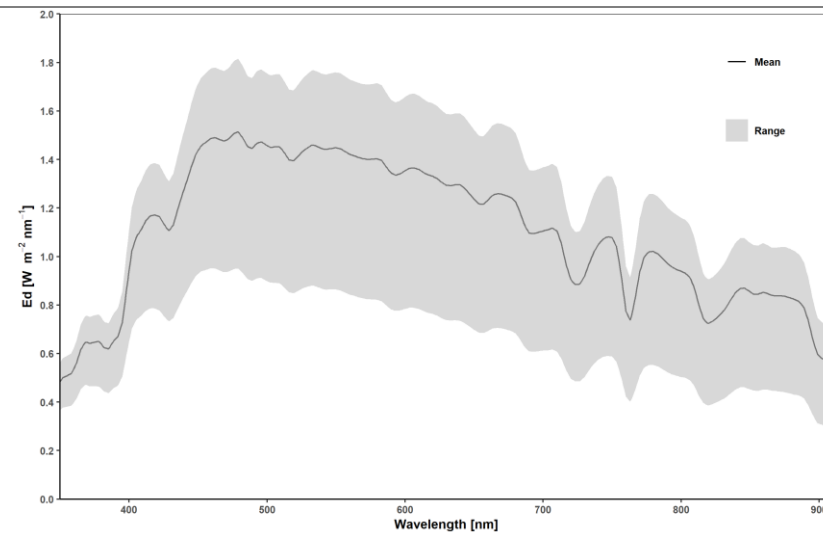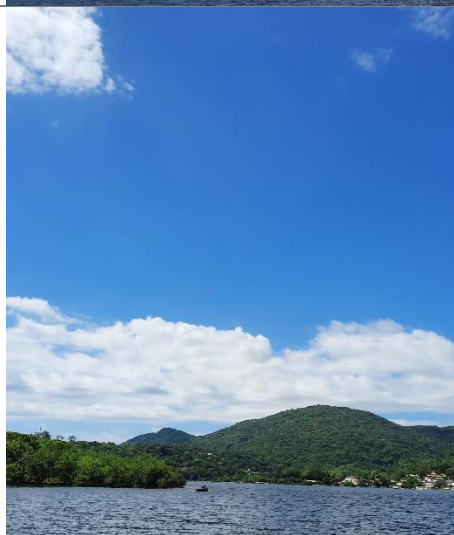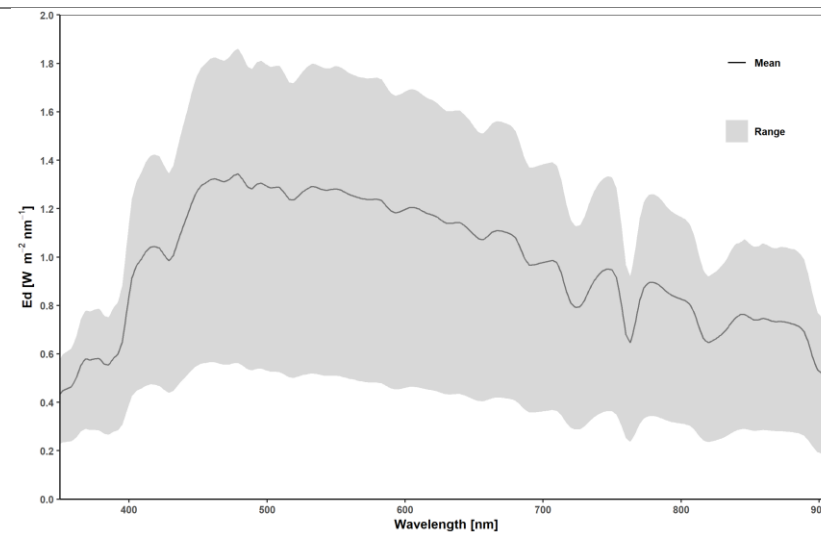
b) Surface Temperature

The temperature was measured with the CTD during all Field Campaigns, except for FC 05 (13/12/21) when the equipment was unavailable.

The water surface temperature ranged from 24.96 °C on FC 02 (03/12/21) up to 28.57 °C on FC 06 (17/12/21). Despite the variability between days, the spatial variability was low within each Field Campaign, with not much temperature difference between sampling points.
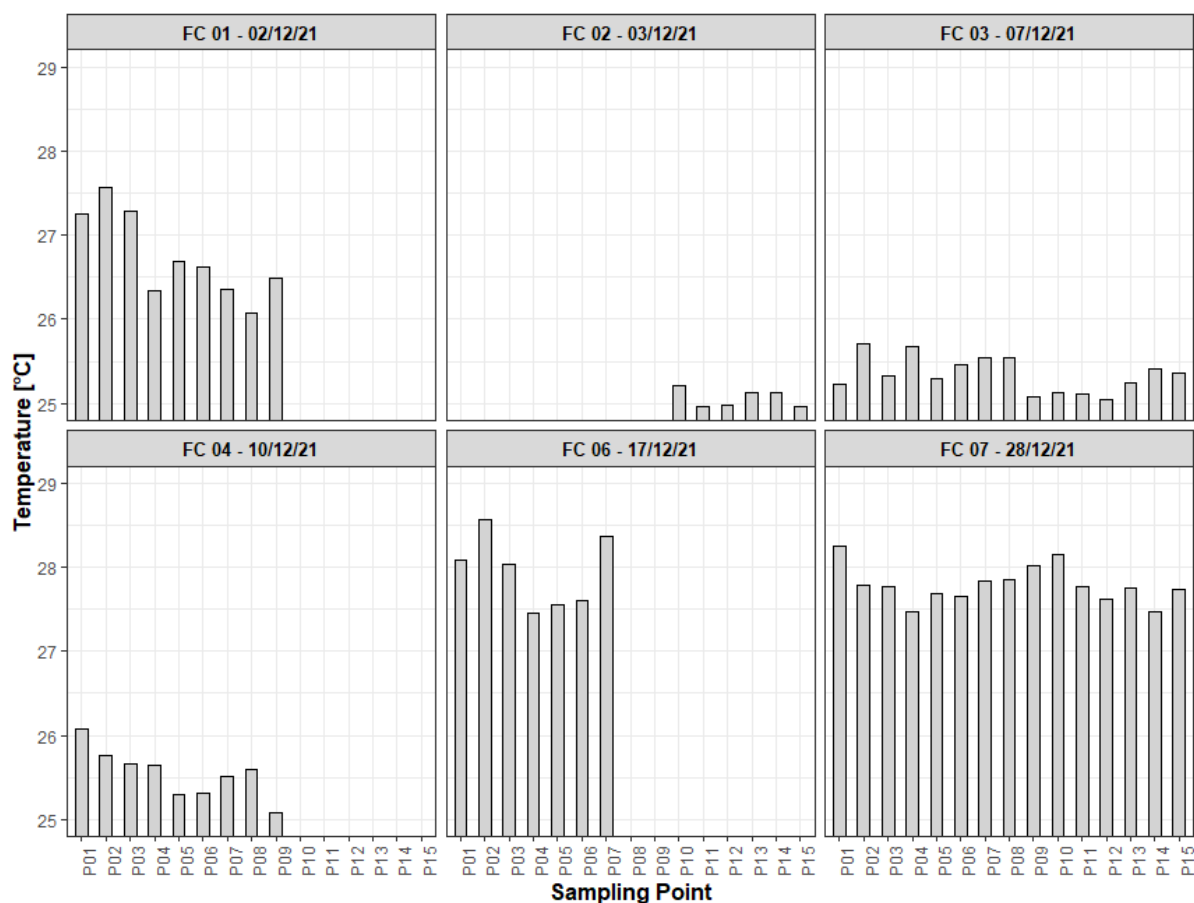
Figure 38: Temperature measured for each sampling point across the different Field Campaigns (FC)

c) Surface Salinity

Salinity was also measured with the CTD during all Field Campaigns, except for FC 05 (13/12/21) when the equipment was unavailable.

As a result of the marine influence caused by the Barra Channel, surface salinity showed very distinct characteristics between the South Lagoon and Central Lagoon. The points in the South Lagoon (P01 to P08) showed on average a salinity of 18.35 PSU, while in Central Lagoon the points (P09 to P15) had an average salinity of 24.82 PSU. The lowest salinity values were measured on P1, highlighting the influence of freshwater inputs on that location (outlet of the Apa river).
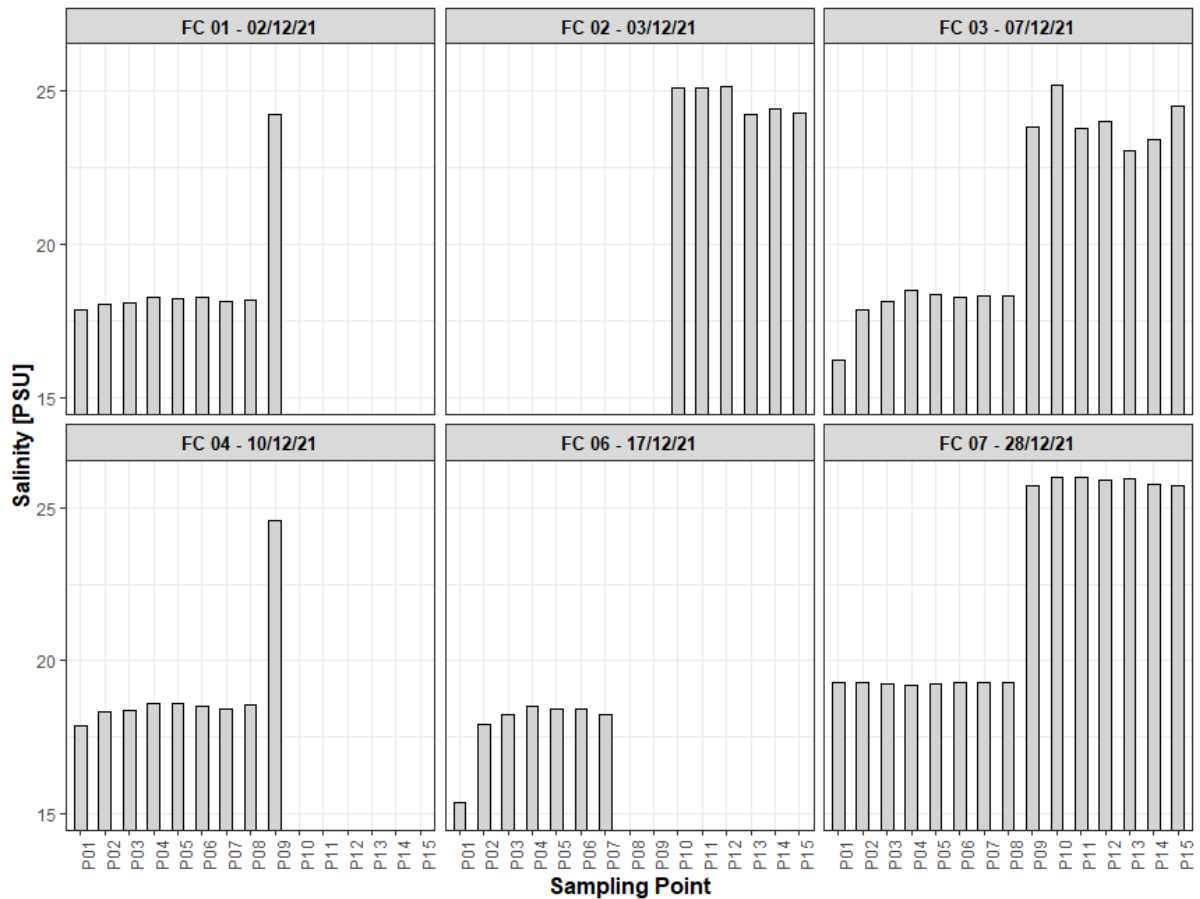
Figure 39: Salinity measured for each sampling point across the different Field Campaigns (FC)

d) Vertical Profiles of Temperature and Salinity

The CTD measurements also provide the vertical profile of water temperature and salinity, which indicate the physical characteristics of the water column that have implications for its biogeochemistry.

For the points most representative of the South Lagoon (P01 to P06) a relatively well-mixed water column was observed during all of the field campaigns (see the example of FC01 in Figure 40). Only points P05 and P06, which have higher depths (up to 5.4 m), present a slight gradient at the bottom layer with temperatures decreasing up to 1° C and salinity increasing between 2 and 4 PSU. The highest salinity observed was 22.5 PSU at the bottom layer of P06 during FC03 – 07/12/21.
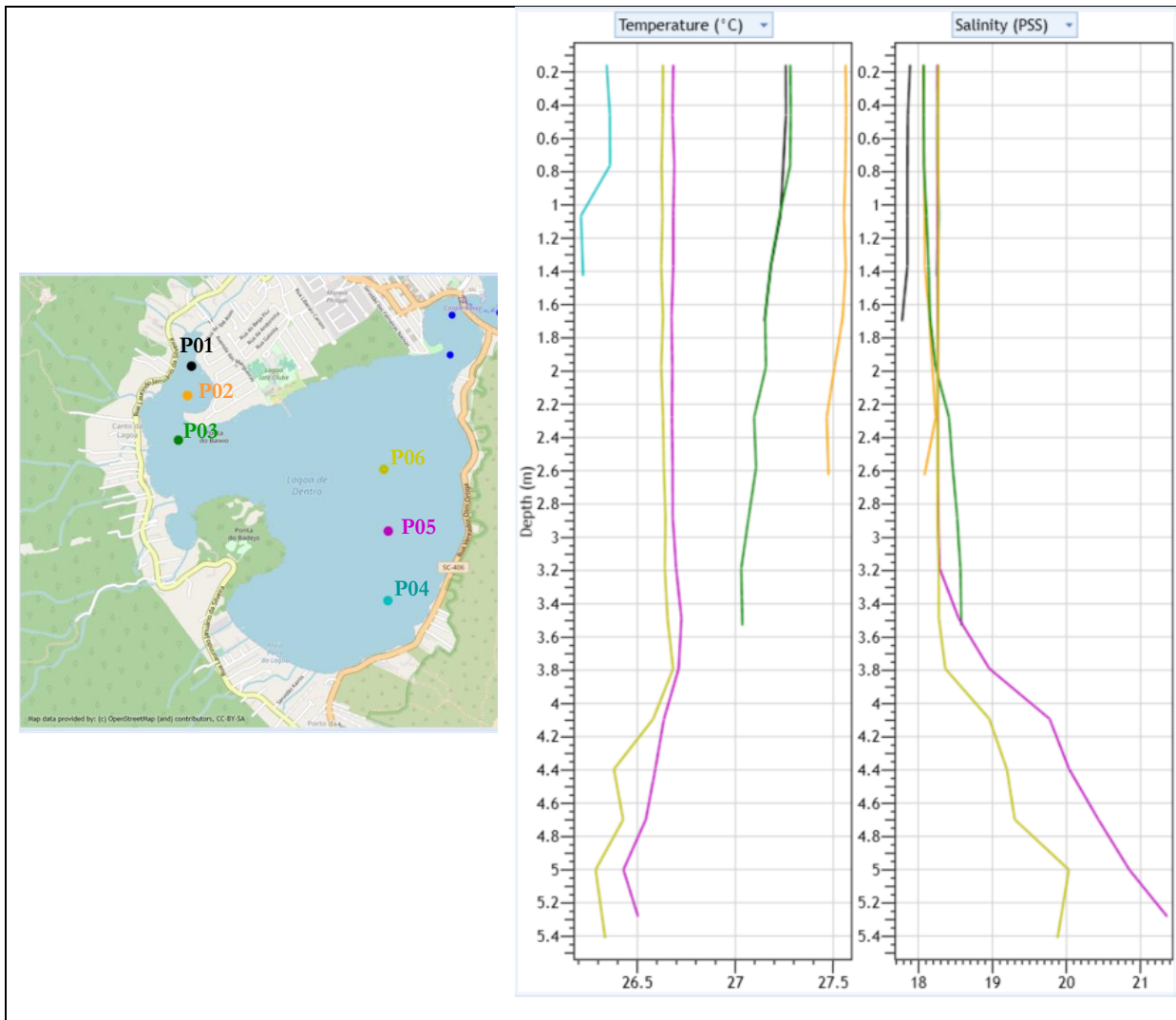
Figure 40: Temperature and Salinity vertical profile of the points in the South Lagoon (P01 to P06) during FC01 – 02/12/2021

For the points in the Central Lagoon (P10 to P15) consistent higher salinity was observed as expected due to the proximity to the channel that connects the Lagoon to the ocean. P10, P13, P14 and P15 are all located in shallower parts of the lagoon, with depths varying from 1.0 to 2.2 m, and presented uniform temperature and salinity profiles for all the FCs. For P11 and P12, which have depths of around 5.0 m, profiles with rather constant salinity up until 2.0 m depth followed by a steep increase up to values very close to seawater conditions (around 32 PSU) were observed (see example Figure 41), indicating that the bottom layer is likely dominated by water that comes from the ocean through Barra Channel. Comparing the temperature at the surface and the bottom there is also a strong negative thermal gradient, with cooler water at the bottom. This condition leads to a high density difference which hampers vertical mixing and has the potential to cause anoxic conditions in the deeper layers, as has been reported several times in this location (de Barros et al., 2017; Silva et al., 2017). An unexpected feature was observed in the vertical profile during FC02 and FC07 when the temperature had a slight increase with depth in the first layers before decreasing at higher depths (Figure 42).
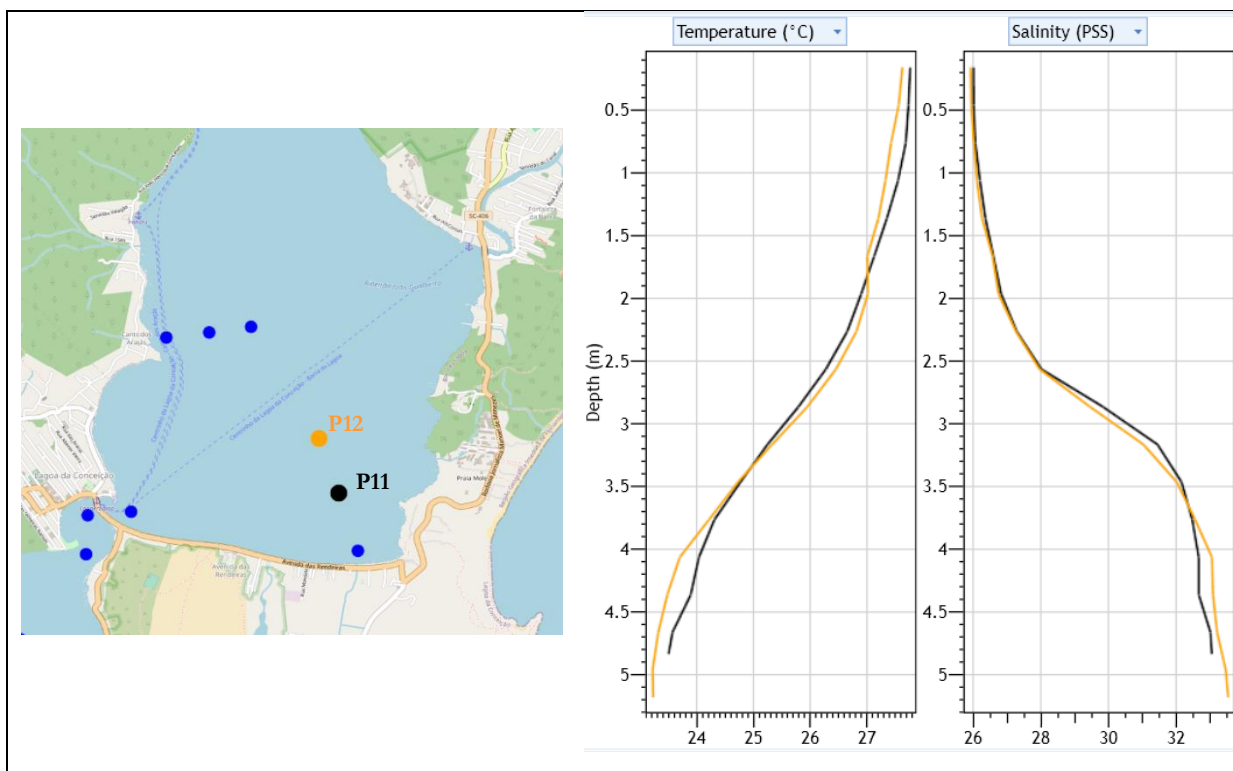
Figure 41: Temperature and Salinity vertical profile of P11 and P12 during FC07 – 28/12/2021
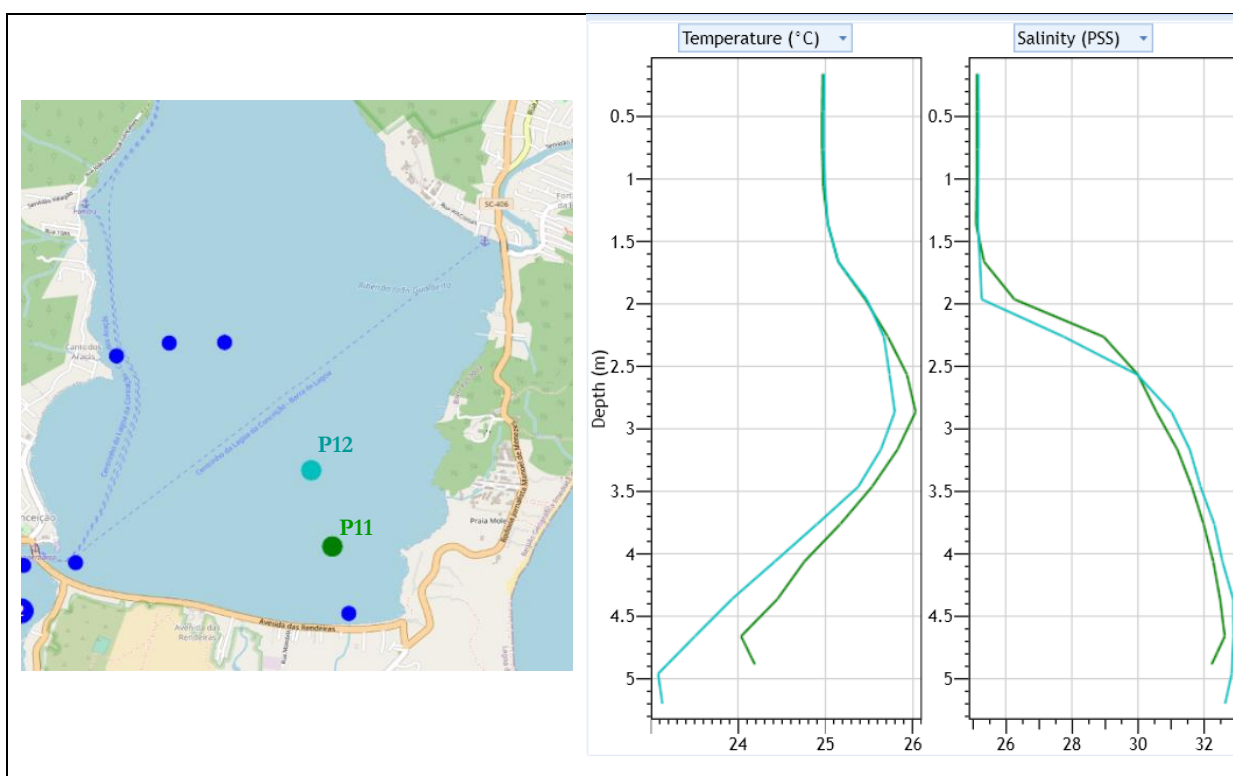
Figure 42: Temperature and Salinity vertical profile of P11 and P12 during FC02 – 03/12/2021

For the points in the transition between the South Lagoon and Central Lagoon (P07, P08 and P09), a very well-mixed column was seen for P07 and P08, which was expected as these points are right in the channel that connects the two parts of the lagoon, where stronger flux is observed. P09 already represents the conditions typical of the Central Lagoon, which receives more influence from the sea and therefore higher salinity overall and a bottom layer saltier and cooler. The profiles obtained for these points during FC07 are presented in Figure 43 as an example.
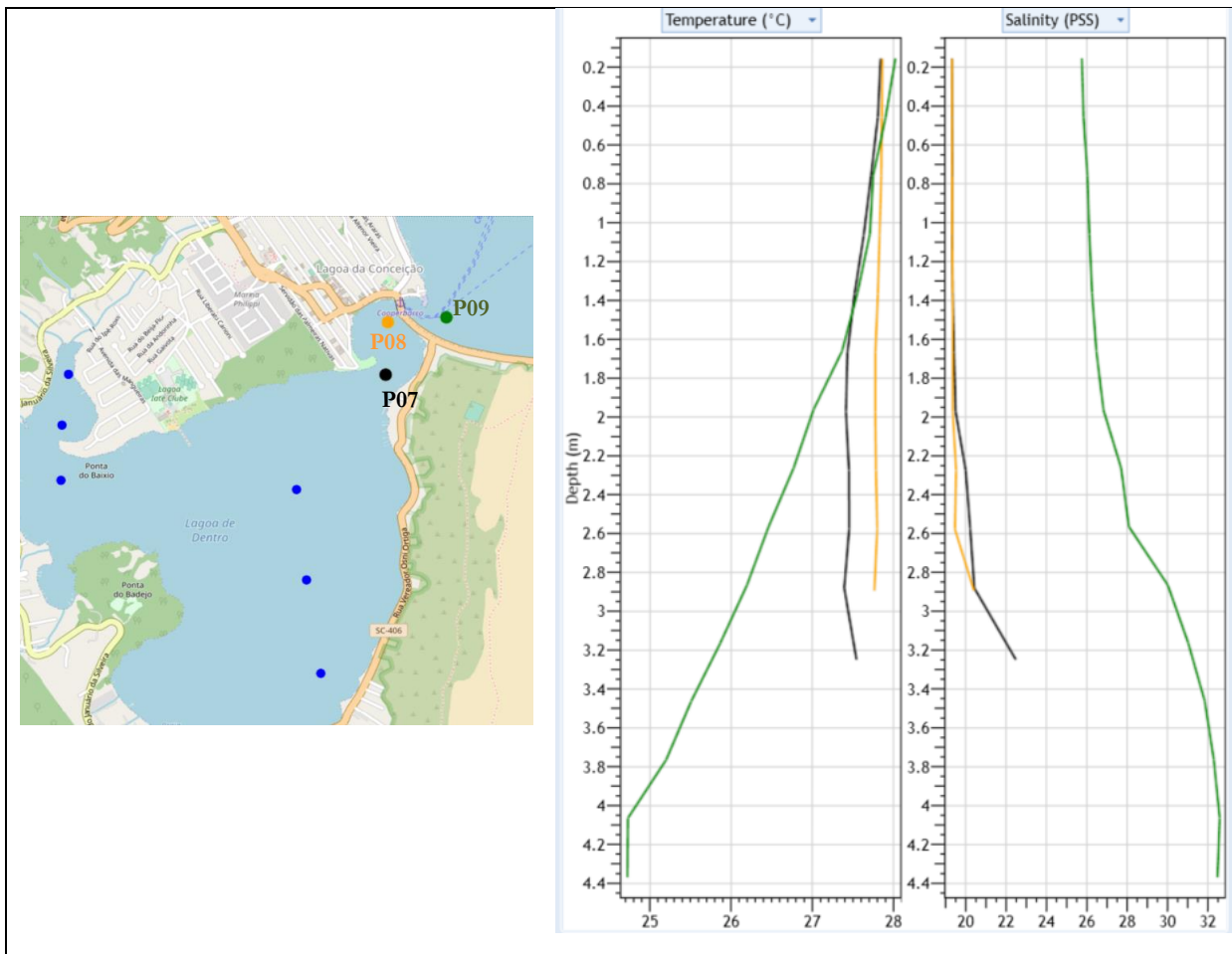
Figure 43: Temperature and Salinity vertical profile of the points in the transition between South and Central Lagoon (P07, P08 and P09) during FC07 – 28/12/2021

e) Thermotolerant Coliforms

Thermotolerant coliforms, also known as faecal coliforms, are common indicators of faecal contamination in waters. According to Brazilian legislation, water is considered inappropriate for bathing when in more than 20% of a set of samples collected over 5 weeks in the same place, there are more than 1,000 faecal coliforms (thermotolerant) in 100 mL. During the research Field Campaigns, the thermotolerant coliforms were always lower than 1,000 MPN[4]/100 mL, with the highest value (940 MPN/100mL) observed on P8, which is located close to the most occupied area of the watershed, during FC 01 (02/12/21). It should be noted that on the last campaign (FC 07), the laboratory that analysed the samples for this parameter used a different method, called enzyme substrate, and all the results were < 10 MPN/100mL (assumed as 0). For the other campaigns, the method used was multiple tube fermentation.
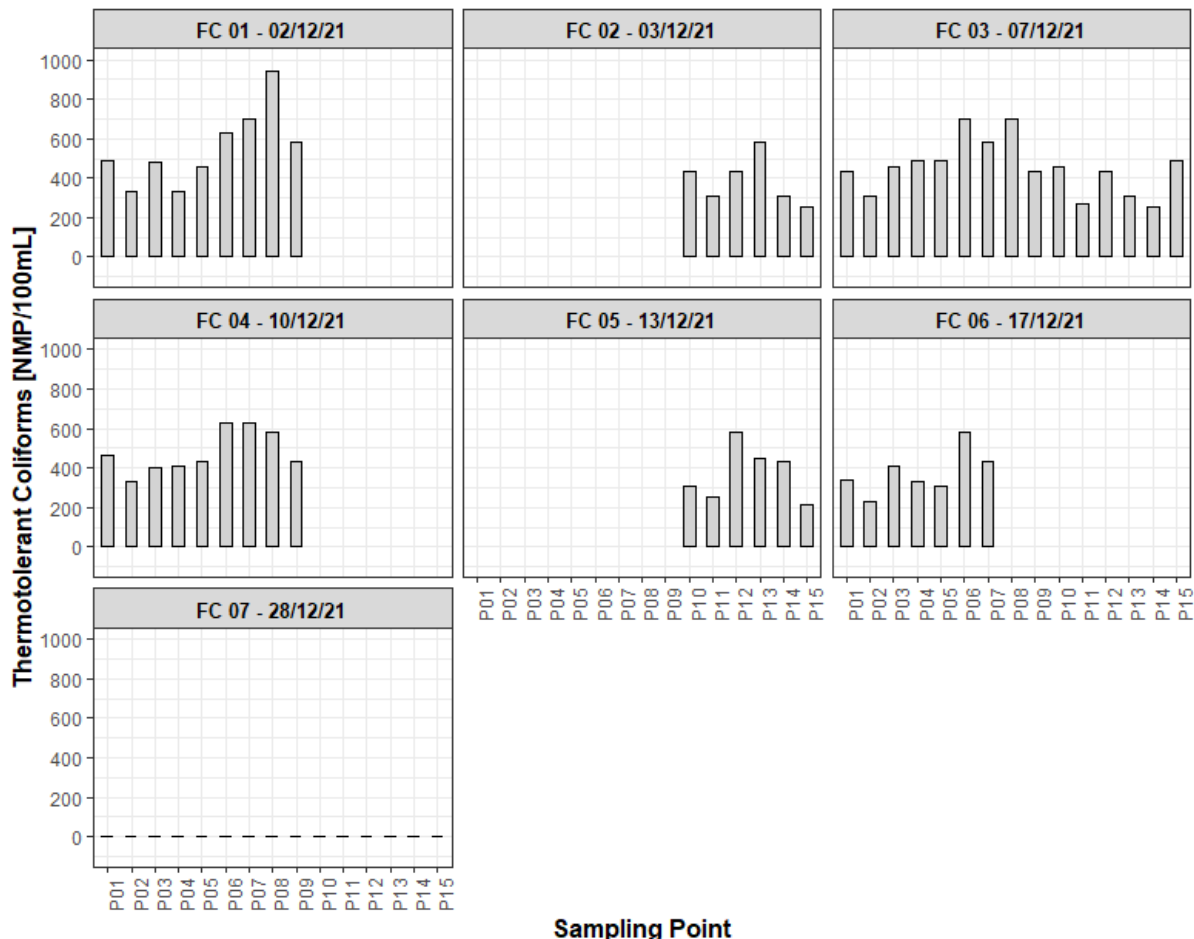
Figure 44: Thermotolerant coliforms measured for each sampling point across the different Field Campaigns (FC)

f) Coloured Dissolved Organic Matter – CDOM

Coloured Dissolved Organic Matter (CDOM) was measured in-situ on each of the Field campaigns at least 3 consecutive times per sampled point. During FC 01, all of the recorded values were below the detection limit of the instrument (0.25 µg/L), which meant they were invalid and therefore discarded. The same happened on FC 02 and FC 04 for the first sampling point of that day (P10 and P1 respectively).

---

[4] MPN means the Most Probable Number, a statistical procedure commonly used in microbiology for estimating the number of organisms in a sample.

The average CDOM concentration was calculated for each point per campaign considering the valid measurements.

Overall, the highest values of CDOM were observed at P1, close to the outlet of river Apa. The maximum value of CDOM was recorded at that point on FC 06 (17/12/21), reaching 58.64 µg/L. It was also possible to observe that CDOM values were consistently higher in the South Lagoon points (average 39.24 µg/L) in comparison to the Central Lagoon points (average 32.10 µg/L). This highlights the stronger influence of freshwater inputs in the South Lagoon in comparison to the Central Lagoon, as CDOM is considered a tracer of riverine inputs because of its negative linear correlation with salinity (IOCCG, 2000).
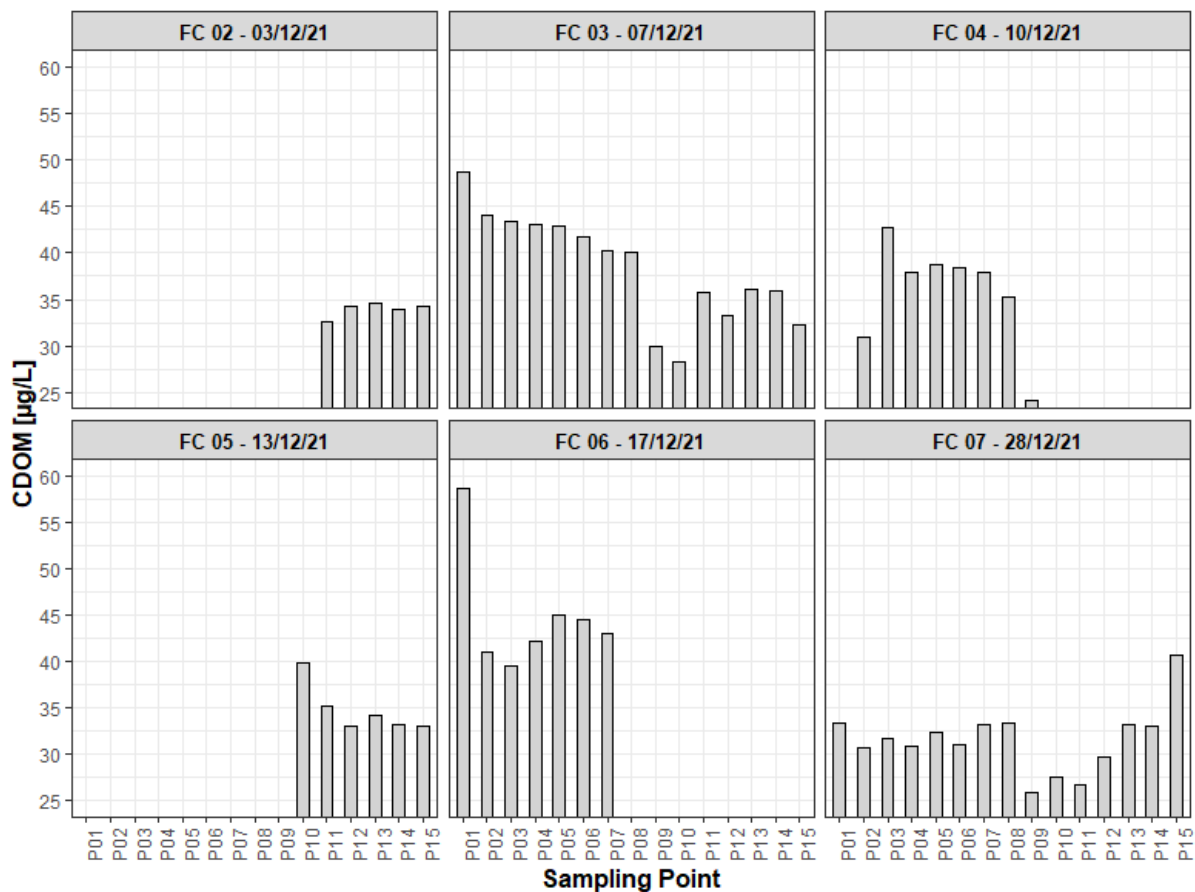
Figure 45: CDOM concentration measured for each sampling point across the different Field Campaigns (FC)

g) Suspended Particulate Matter – SPM

Suspended Particulate Matter (SPM) values ranged from 26 mg/L to 464 mg/L. It should be noted that the analysis from FC 07 was conducted by a different laboratory from the previous campaigns and the values were systematically larger, even though they used the same method (see discussion on APPENDIX D – FIELD DATA QUALITY CONTROL). No other obvious patterns were observed a priori.
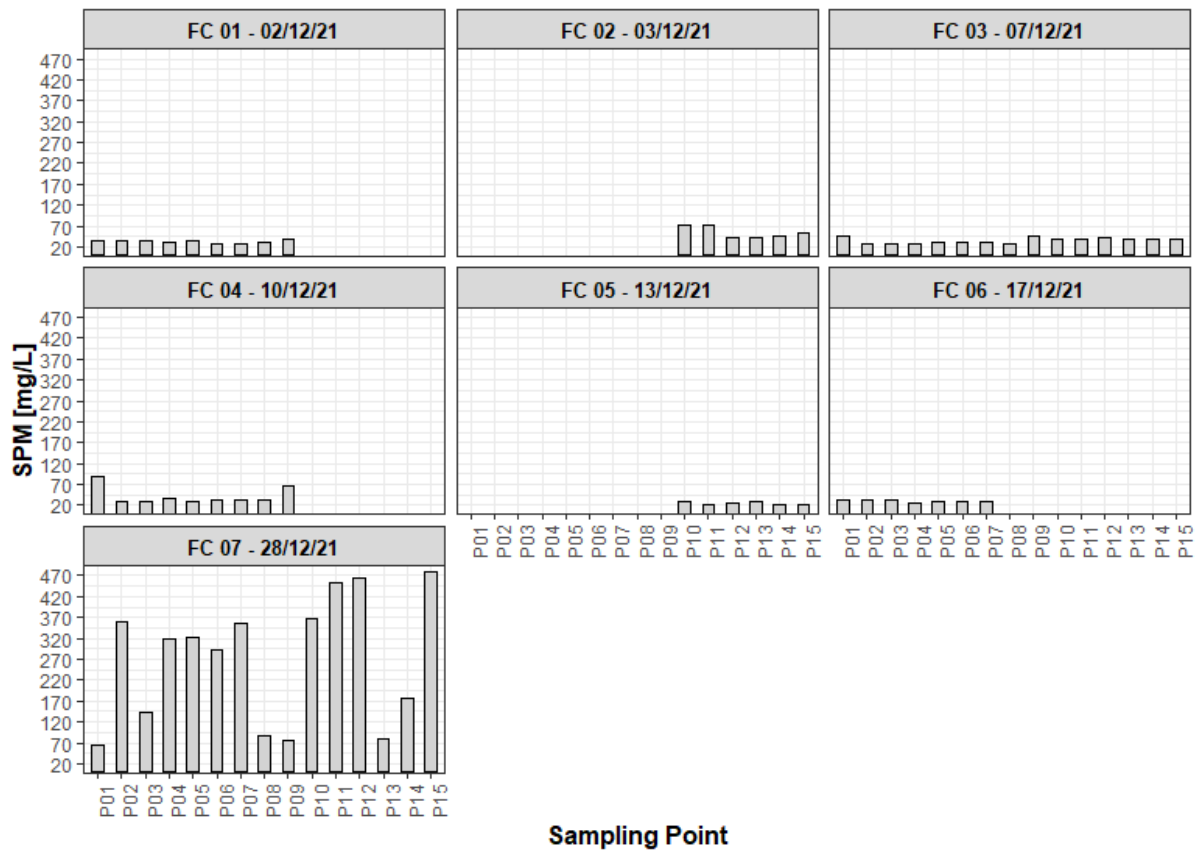
Figure 46: SPM concentration measured for each sampling point across the different Field Campaigns (FC)

h) Chlorophyll-a

Chlorophyll-a measurements ranged from 0 to 223.87 µg/L. The detection limit of the laboratory that analyzed the samples from FC 01 to FC 06 was 0.25 µg/L, so on several occasions when the result was < 0.25 µg/L, it was assumed to be 0. It should be noted that the analysis from FC 07 was conducted by a different laboratory from the previous campaigns (though the same method was applied) and the values were systematically an order of magnitude larger (see discussion on APPENDIX D – FIELD DATA QUALITY CONTROL). Disregarding FC 07, the highest chlorophyll-a measurement (7.12 µg/L) was observed on P3 during FC 03 (07/12/21), right after an algae bloom event that occurred between 04/12/21 and 06/12/21 (Figure 48). Nonetheless, most of the other points sampled on that day resulted in chlorophyll-a below the detection limit (<0.25 µg/L). Similarly, on P3 during FC 04 (10/12/21), when floating algae were observed on the field (Figure 49), the result was <0.25 µg/L. This could mean potential problems with the analysis from the laboratory or the conservation of the samples. Another hypothesis would be the predominance of other photosynthetic pigments due to the algae species (most probably brown algae *Fibrocapsa japonica*, already recorded in other bloom events in the Lagoon).
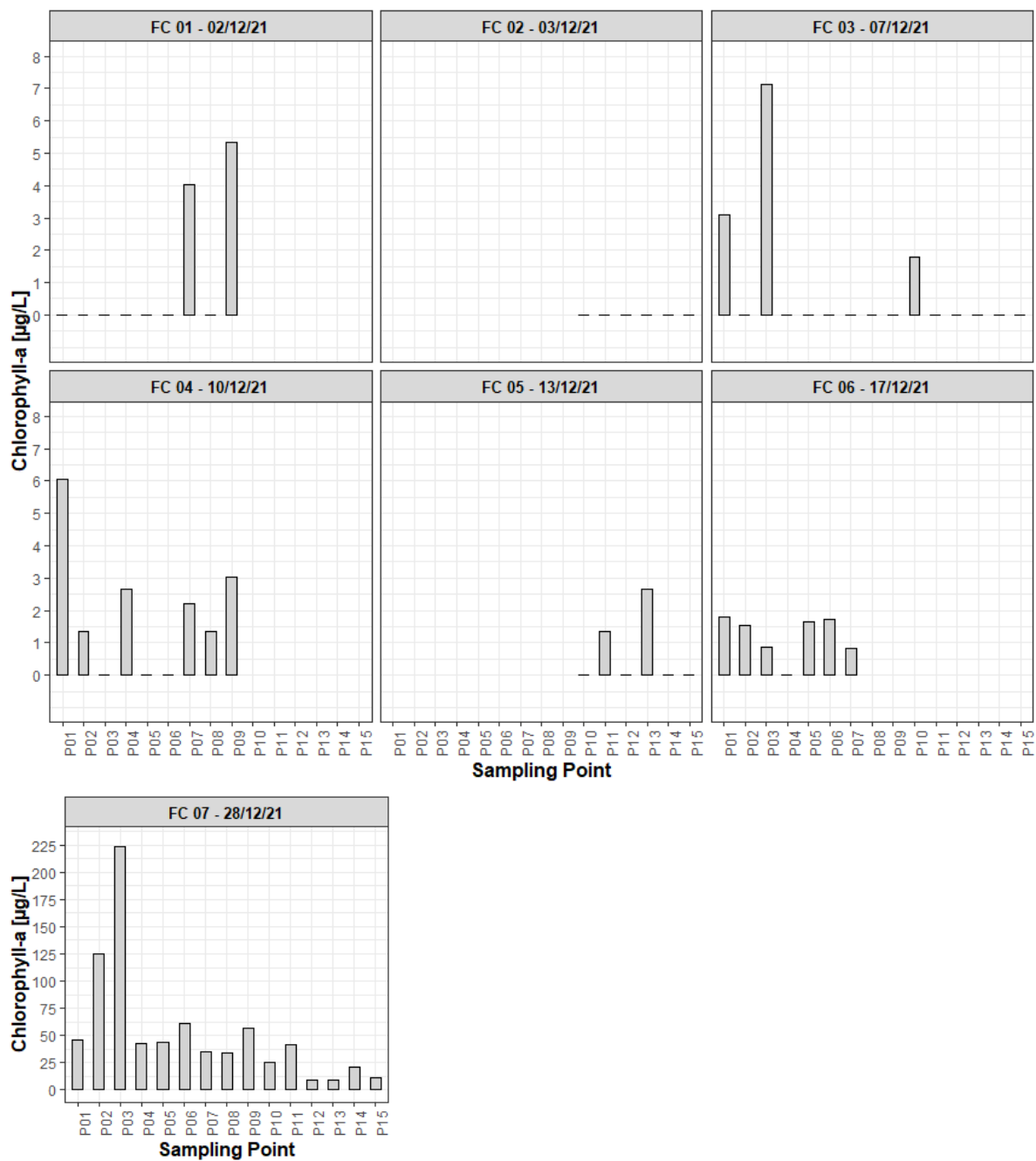
Figure 47: Chlorophyll-a concentration measured for each sampling point across the different Field Campaigns (FC)

Figure 48: Pictures of the algae bloom washing toward the margins of the lagoon on the 6th of December 2021

Figure 49: Pictures of the floating algae observed on P3 during FC 04 on the 10th of December 2021

i) Compilation of Water Qualilty Measurement Results

Date	Time	Point	Chlorophyll-a (μg/L)	CDOM (μg/L)	SPM (mg/L)	Faecal Coliforms (MPN/100ml)	Surface Temperature (°C)	Surface Salinity (PSU)
02-Dec	09:34	P01	<0.25	NA	34	490	27.25	17.88
02-Dec	09:45	P02	<0.25	NA	33	330	27.56	18.06
02-Dec	09:56	P03	<0.25	NA	33	480	27.28	18.07
02-Dec	10:09	P04	<0.25	NA	32	330	26.34	18.25
02-Dec	10:21	P05	<0.25	NA	33	460	26.68	18.25
02-Dec	10:31	P06	<0.25	NA	27	630	26.63	18.26
02-Dec	10:45	P07	4.01	NA	29	700	26.35	18.14
02-Dec	11:00	P08	<0.25	NA	30	940	26.07	18.20
02-Dec	11:08	P09	5.35	NA	38	580	26.48	24.23
03-Dec	09:39	P10	<0.25	NA	71	430	25.20	25.13
03-Dec	10:00	P11	<0.25	32.61	73	310	24.96	25.10
03-Dec	10:08	P12	<0.25	34.27	41	430	24.98	25.14
03-Dec	10:19	P13	<0.25	34.51	41	580	25.13	24.23
03-Dec	10:27	P14	<0.25	33.91	45	310	25.12	24.41
03-Dec	10:35	P15	<0.25	34.22	55	250	24.97	24.28
07-Dec	09:28	P01	3.11	48.74	46	430	25.22	16.21
07-Dec	09:42	P02	<0.25	44.14	29	310	25.71	17.84
07-Dec	09:52	P03	7.12	43.42	27	460	25.33	18.14
07-Dec	10:08	P04	<0.25	43.09	28	490	25.67	18.49
07-Dec	10:19	P05	<0.25	42.96	31	490	25.30	18.37
07-Dec	10:30	P06	<0.25	41.79	32	700	25.45	18.28
07-Dec	10:43	P07	<0.25	40.31	32	580	25.54	18.34
07-Dec	10:53	P08	<0.25	40.11	27	700	25.54	18.30
07-Dec	11:04	P09	<0.25	29.89	45	430	25.09	23.85

Date	Time	Point	Chlorophyll-a (µg/L)	CDOM (µg/L)	SPM (mg/L)	Faecal Coliforms (MPN/100ml)	Surface Temperature (°C)	Surface Salinity (PSU)
07-Dec	11:18	P10	1.77	28.25	39.5	460	25.13	25.22
07-Dec	11:34	P11	<0.25	35.77	40	270	25.11	23.78
07-Dec	11:42	P12	<0.25	33.22	41	430	25.04	24.03
07-Dec	11:55	P13	<0.25	36.01	37	310	25.24	23.07
07-Dec	12:05	P14	<0.25	35.97	37.5	250	25.42	23.44
07-Dec	12:14	P15	<0.25	32.22	40	490	25.36	24.51
10-Dec	09:18	P01	6.05	NA	89	460	26.07	17.85
10-Dec	09:28	P02	1.34	30.90	29	330	25.76	18.34
10-Dec	09:36	P03	<0.25	42.78	31	400	25.66	18.39
10-Dec	09:46	P04	2.67	37.92	37	410	25.65	18.61
10-Dec	09:55	P05	<0.25	38.75	31	430	25.30	18.61
10-Dec	10:03	P06	<0.25	38.49	32	630	25.32	18.49
10-Dec	10:12	P07	2.2	37.90	33	630	25.51	18.43
10-Dec	10:20	P08	1.34	35.27	34	580	25.59	18.57
10-Dec	10:29	P09	3.02	24.09	65	430	25.08	24.57
13-Dec	11:43	P10	<0.25	39.88	30.8	310	NA	NA
13-Dec	11:56	P11	1.34	35.29	20.5	250	NA	NA
13-Dec	12:08	P12	<0.25	33.02	25	580	NA	NA
13-Dec	12:20	P13	2.67	34.20	30	450	NA	NA
13-Dec	12:31	P14	<0.25	33.24	22.5	430	NA	NA
13-Dec	12:42	P15	<0.25	33.02	22	210	NA	NA
17-Dec	09:35	P01	1.8	58.64	32	340	28.08	15.34
17-Dec	09:37	P02	1.52	40.99	34	230	28.57	17.92
17-Dec	09:48	P03	0.87	39.51	33.3	410	28.04	18.25
17-Dec	10:00	P04	<0.25	42.20	26	330	27.46	18.50
17-Dec	10:13	P05	1.63	44.96	29.3	310	27.55	18.40
17-Dec	10:22	P06	1.72	44.44	28	580	27.60	18.40

Date	Time	Point	Chlorophyll-a (µg/L)	CDOM (µg/L)	SPM (mg/L)	Faecal Coliforms (MPN/100ml)	Surface Temperature (°C)	Surface Salinity (PSU)
17-Dec	10:35	P07	0.83	43.03	28	430	28.37	18.22
28-Dec	11:26	P01	46.4	33.44	64	<10	28.25	19.28
28-Dec	11:19	P02	124.94	30.71	360	<10	27.79	19.28
28-Dec	11:11	P03	223.87	31.73	142	<10	27.77	19.26
28-Dec	11:00	P04	43.14	30.93	318	<10	27.47	19.20
28-Dec	10:49	P05	43.25	32.42	324	<10	27.69	19.25
28-Dec	10:41	P06	61.32	31.06	294	<10	27.66	19.26
28-Dec	10:34	P07	35.17	33.15	356	<10	27.84	19.27
28-Dec	10:26	P08	34.22	33.33	88	<10	27.86	19.30
28-Dec	10:18	P09	57.15	25.91	74	<10	28.02	25.73
28-Dec	10:09	P10	25.61	27.63	368	<10	28.15	26.00
28-Dec	10:01	P11	41.87	26.70	452	<10	27.76	25.99
28-Dec	09:53	P12	9.51	29.76	464	<10	27.63	25.90
28-Dec	09:44	P13	8.86	33.16	78	<10	27.76	25.93
28-Dec	09:36	P14	21.36	33.10	178	<10	27.46	25.76
28-Dec	09:28	P15	11.3	40.76	478	<10	27.74	25.72

APPENDIX D – FIELD DATA QUALITY CONTROL

Quality control was performed on the data collected during fieldwork to certify it was fit for use in the following steps of the research. The next sections describe the procedures and analysis conducted for the quality assessment of the radiometric and water quality data collected in the field

RADIOMETRIC DATA

In the case of above-water radiometric field measurements, several factors may contribute to uncertainties of the measured reflectance, with glint contamination being considered the main challenge (IOCCG Protocol Series, 2019). Although there are recommendations for the viewing geometry in order to minimize its effects (viewing angle θ of 40° and azimuth ϕ of 135° relative to the sun (Mobley, 1999)), these are in practice difficult to follow precisely in the field, especially with smaller boats and hand-held instruments as was the case of this research fieldwork. With this limitation in mind, at least three consecutive radiance and irradiance paired measurements were taken within one to three minutes at each sampling location. This approach is recommended for further assessment of the quality of the data and identification of potential disturbances in the measurements (IOCCG Protocol Series, 2019).

The R_{rs} spectra calculated from raw data collected during fieldwork showed high variability within consecutive measurements taken under less than three minutes (see Figure 50). In addition, most of the measurements had considerably high reflectance at the NIR and UV parts of the spectrum. According to Kutser et al. (2013), high values in these regions can be associated with glint contamination.
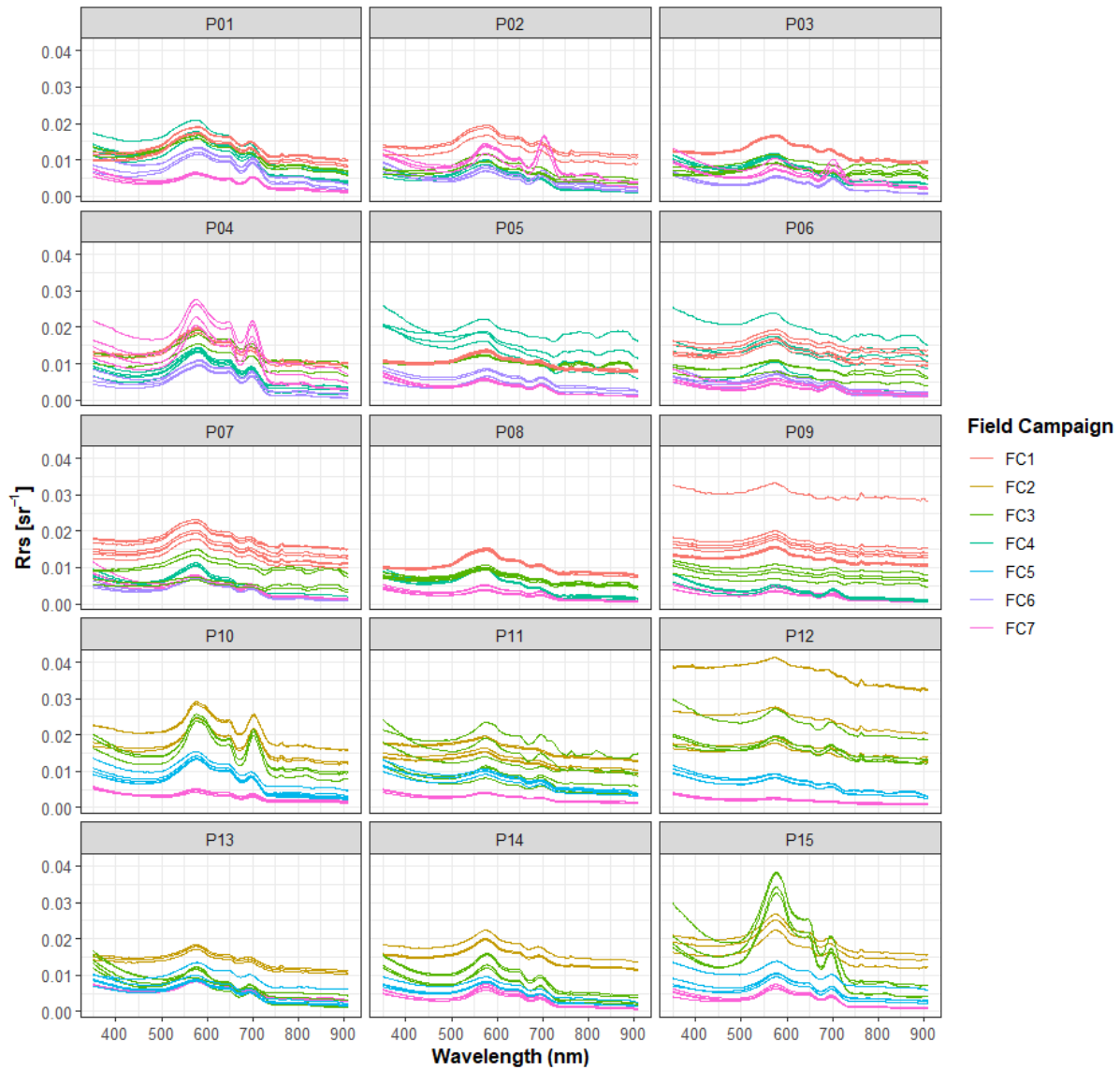
Figure 50: Rrs spectra calculated from raw consecutive Ed and Lw measurements

Bottom reflectance was discarded based on the Near-Infrared Bottom-Effect Index – NIBEI (Arabi et al., 2020), which is taken as the ratio of the reflectances at 900 nm and 750. For optically deep waters this ratio can be approximated as the ratio of pure water absorption at 750 and 900, equal to a constant value of 2.67. For all the spectra the NIBEI was lower than this value, varying from 1.01 to 2.27 (Figure 51), therefore the hypothesis of bottom reflectance contamination in the measured spectra was discarded.

The variability of the sky-sun downwelling irradiance (E_d) and the upwelling radiance (L_u) were therefore investigated, as well as their potential link to glint contamination and correction procedures.
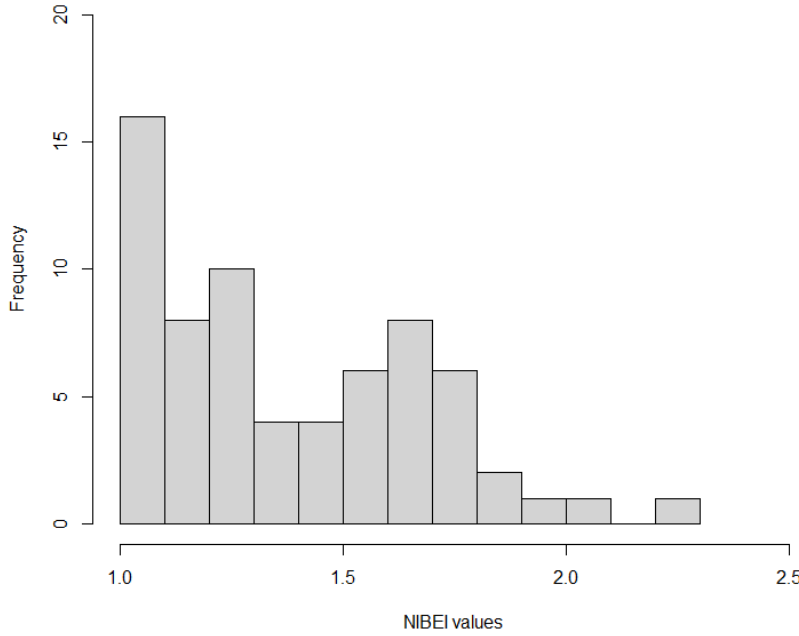
Figure 51: Histogram of the NIBEI calculated for the 67 measured reflectance spectra

a) Variability in Downwelling Irradiance (E_d) and Above-Water Upwelling Radiance (L_w)

The sky-sun downwelling irradiance (E_d) and above-water upwelling radiance (L_w) measurements were inspected to evaluate their variability and how this could affect the R_{rs} spectra.

During <u>overcast days</u> (FC01 and FC02), it was observed that E_d spectra were relatively low and presented a reduced range (see Table 10 in APPENDIX C – OVERALL CONDITIONS DURING FIELDWORK). Looking at consecutive E_d measurements (taken at the same point within less than three minutes) (Figure 52), the variability can be considered negligible (mean coefficient of variation equal to 0.9%). The L_w spectra, on the other hand, with a mean coefficient of variation equal to 16%, showed considerable variability within consecutive measurements for most points (Figure 53). This is likely associated with variation in the viewing geometry of the handheld sensor due to wobbling of the boat and/or water surface perturbations (i.e. from wind and waves), which may introduce specular reflection (glint) in the measurements. In these conditions it is possible, therefore, to assume that variability in R_{rs} spectra does not come from changes in E_d, but only from L_w and probably sun-glint contamination.

During mostly clear days with scattered clouds (FC03 to FC07), E_d spectra were higher and more variable (see Table 10 in APPENDIX C – OVERALL CONDITIONS DURING FIELDWORK), even for measurements at the same point taken within less than three minutes (Figure 52). Mean coefficients of variation equal to 5% for E_d and 13% for L_w measurements were observed.

In such unstable conditions, both E_d and L_w variability will influence the R_{rs} spectra and in theory they should be synchronized (i.e. higher E_d matching higher L_w and vice-versa). This was not always the case, as can be seen for P13 during FC03 (Figure 54), where the measurement taken at 12:02:04 had the highest L_w and the lowest E_d of the consecutive spectra, which will yield a discrepantly high spectrum for R_{rs}. This is likely to be a combined effect of changing illumination conditions and the introduction of specular reflection.

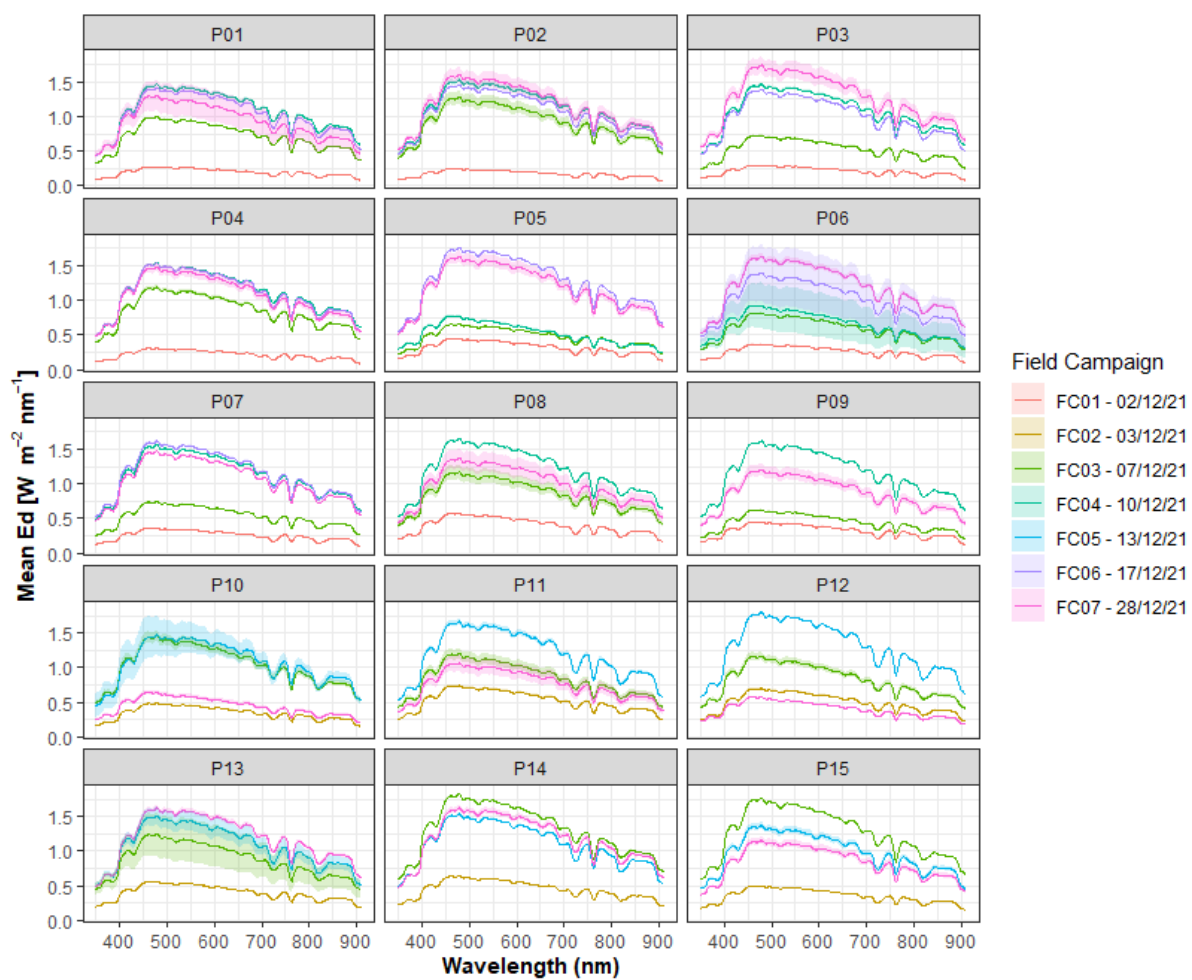Figure 52: Mean E_d (solid lines) and standard deviation (ribbon) of consecutive measurements at each point for all the Field Campaigns.

Figure 53: Mean L_w (solid lines) and standard deviation (ribbon) of consecutive measurements at each point for all the Field Campaigns.
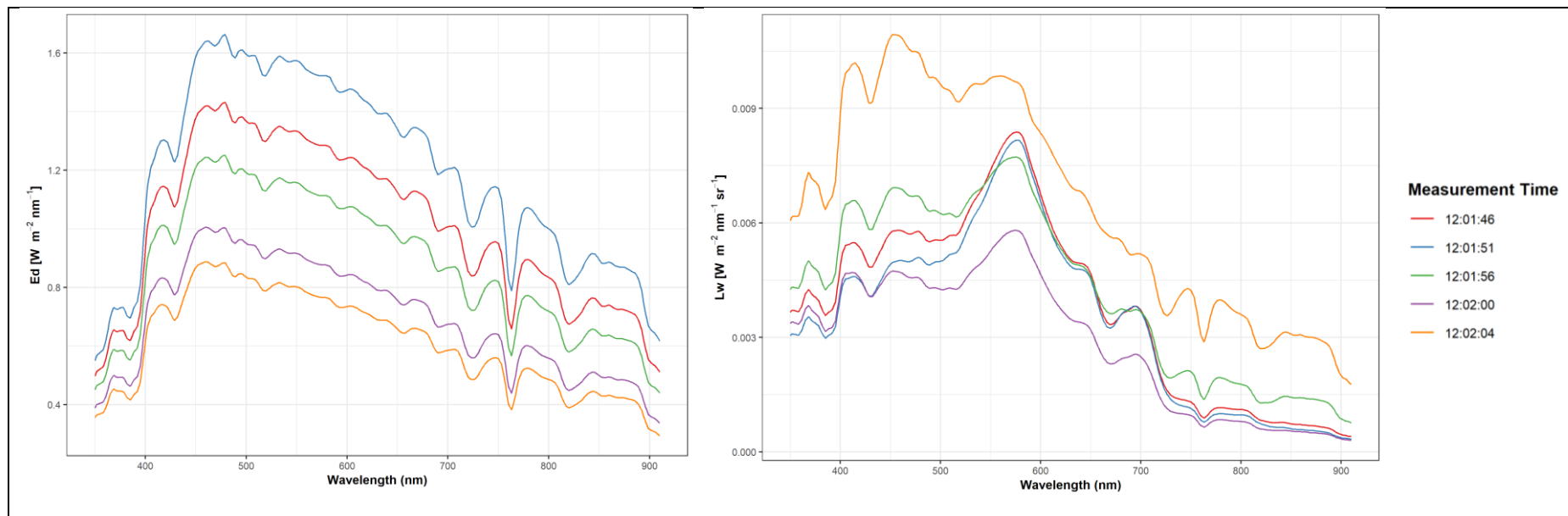
Figure 54: Consecutive E_d and L_w measurements taken at P13 during FC03 – 07/12/2021, with unstable sky conditions

b) Glint Contamination

Considering that the main source of instability in the measurements was likely glint, our first approach was to look into the days with stable E_d (overcast) and assume that the lowest L_w spectrum was glint-free and the difference between the lowest and highest spectra would represent the glint component. This analysis was performed for Field Campaigns (FC) 01 and 02, which took place on the 2nd and 3rd of December 2021. The illumination conditions on those two days were very similar, but the wind was much lighter on the FC 02 (~1 knot) when compared to FC 01 (~8 knots).

It was possible to observe that the normalized residual radiance (difference between the highest and lowest spectra, divided by the maximum value observed) was fairly stable on the day with no wind, with a spectral shape resembling the sky radiance in overcast conditions (Figure 55), which could be explained as sunlight reflected on the water surface due to the mirroring effect observed in such conditions (see picture on Figure 57). For FC 01, with stronger wind, the residuals were more variable, possibly associated with surface roughness and the effect of the capillary waves, but were still resembling the same pattern.
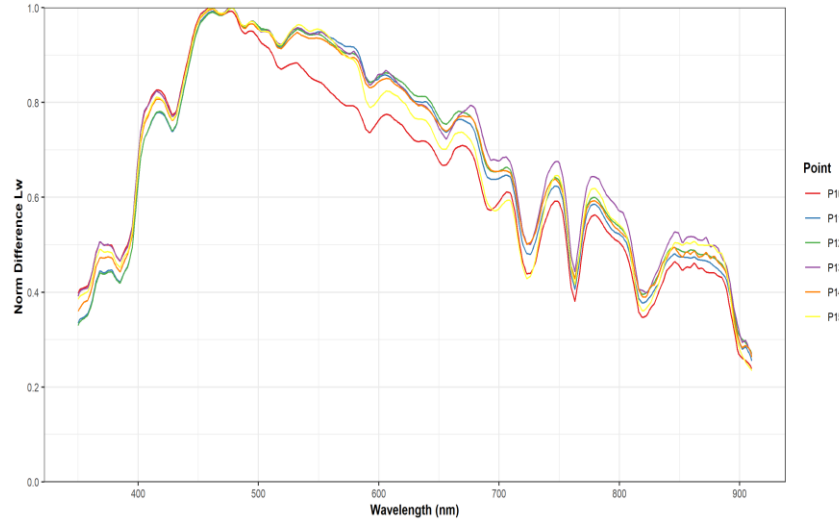
Figure 55: Normalized Lw residuals (difference between lowest and highest measured spectra) during FC02, with overcast conditions and no wind.
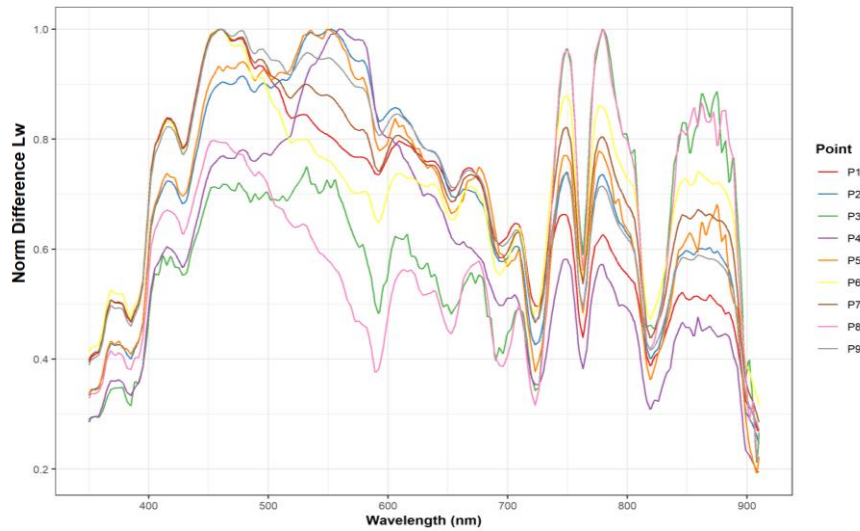
Figure 56: Normalized Lw residuals (difference between lowest and highest measured spectra) during FC01, with overcast conditions and moderate wind.

Figure 57: Pictures of the conditions observed during a) FC01, with an overcast sky and moderate wind that result in rough water surface; and b) FC02, with an overcast sky and no wind, resulting in a smooth water surface with an observable mirror effect

Based on this, it was opted for selecting the lowest reflectance (R_{rs}) spectra of the consecutive measurements at each point, assuming these would be the least glint contaminated ones. Nevertheless, some reflectance spectra were consistently high in the NIR (Figure 58), potentially still containing glint.
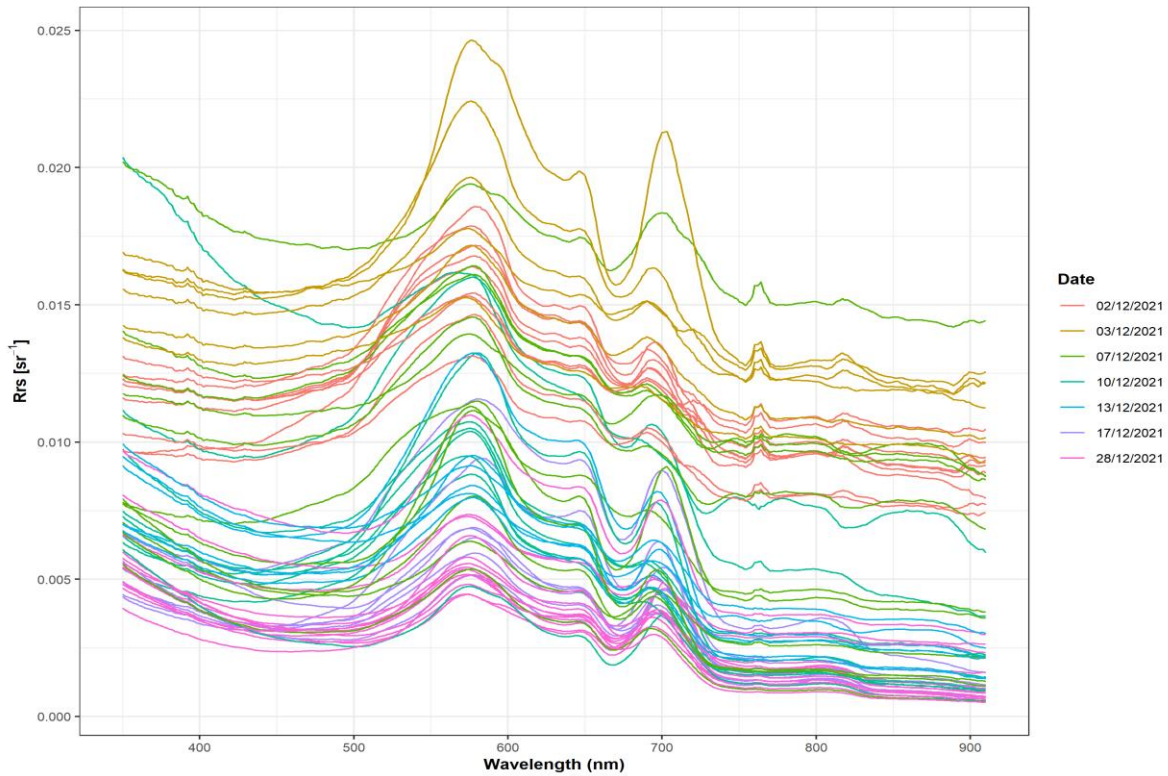
Figure 58: Lowest reflectance (R_{rs}) spectra of the consecutive measurements at each point for the different field campaigns

The method proposed by Kutser et al. (2013) to remove glint effects from in-situ radiometric data was then applied to the measurements. Their method is based on the assumption that the water reflectance near 900 nm is negligible (for optically deep waters) due to strong absorption by water molecules and that it is also commonly very close to zero in the UV part of the spectrum for optically complex waters. As such, R_{rs} spectra can be corrected by fitting a power function between reflectance values in the wavelengths range of 350-380 nm and 890-900 nm and subtracting it from the original spectrum. Groetsch et al. (2017) used an analytical model and matching above- and below-water radiometric measurements to show that indeed a correction factor that is wavelength dependent (instead of a constant value) represents well the glint component, which in most conditions resembles a power relation as proposed by Kutser et al. (2013). Nevertheless, the application of the method to this research's field data resulted in over-correction of the spectra, with even negative reflectance values in several cases (see an example of measurements from FC05 in Figure 59). This problem had been reported by the authors and was mostly seen in CDOM-rich waterbodies. Since the reflectance measurements were to be used as input to the 2SeaColor model, which is based on the curvature of the spectra to derive IOPs, the use of the spectra with negative (or ignored) values would hamper the results.
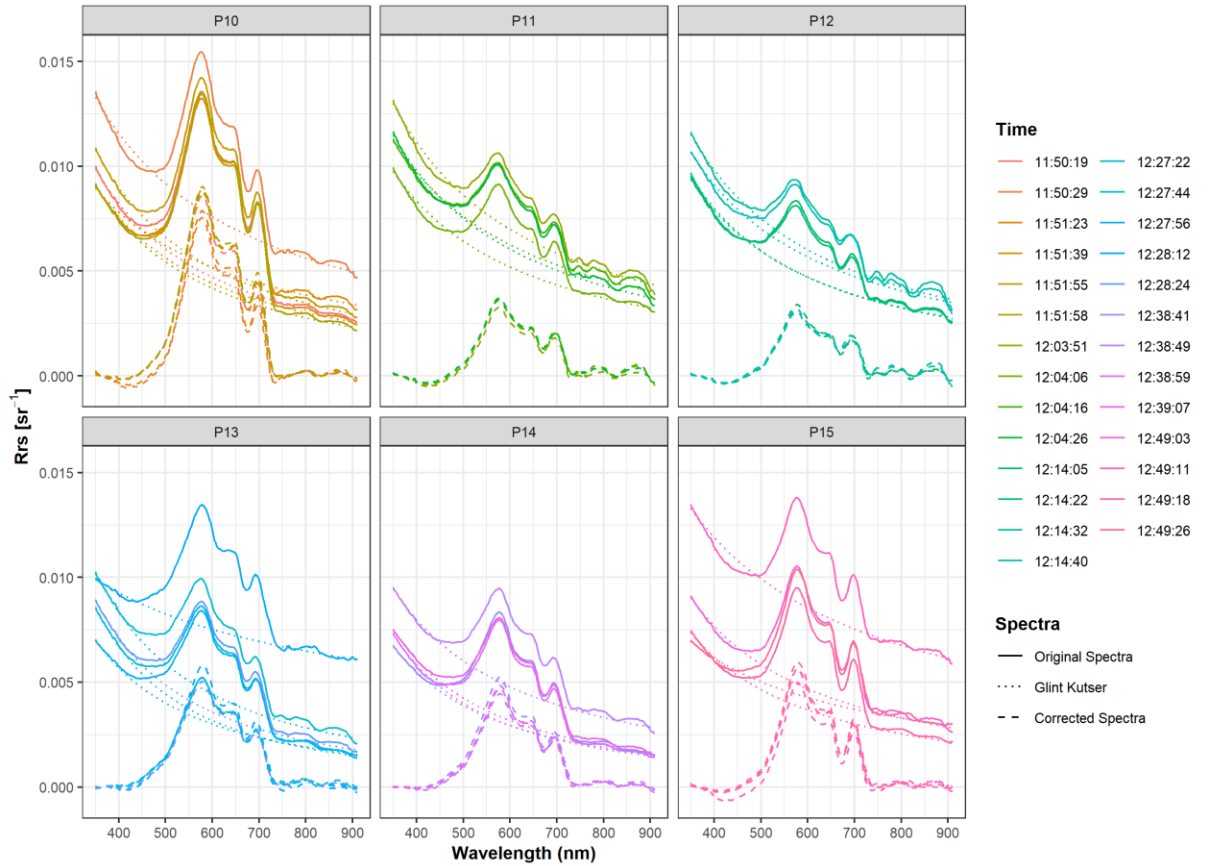
Figure 59: Visualization of the Kutser et al. (2013) correction method applied to the reflectance spectra measured during FC05. Solid lines are the original spectra, dotted lines are the fitted power function that represents the glint component and dashed lines are the corrected spectra calculated as the difference between original and glint spectra.

The presence of a feature at the oxygen absorption wavelength (near 760 nm) was then investigated, as it was indicated by other authors to be related to problems in the measurements, most likely glint (Kutser et al., 2009). According to the authors, a dip or a peak in that position would be only visible in case the downwelling irradiance and upwelling radiance signals are not proportional and therefore can be used as

an indicator of glint. In the collected data it was observed that the spectra which had a higher signal in the NIR also presented a peak around 760 nm (Figure 58). Similar to what was proposed by Kutser et al. (2009) for removing glint from hyperspectral imagery and later applied by Busch et al. (2013) in the case of field radiometric data, the height of the oxygen absorption feature was used to flag the spectra which were likely contaminated by glint. The height of the feature (H) is calculated as:

$$H = R_{rs}(760) - \frac{R_{rs}(750) + R_{rs}(775)}{2}$$ 22

Where $R_{rs}(\lambda)$ is the remote sensing reflectance at wavelength λ

This was applied to the already selected lowest spectra at each point. By manual tuning, a threshold of 5.00E-05 sr^{-1} was established for the flagging. Spectra with H higher than the threshold were assumed to have glint and therefore flagged and removed from further processes. From the 67 measured spectra, only 34 were not flagged.
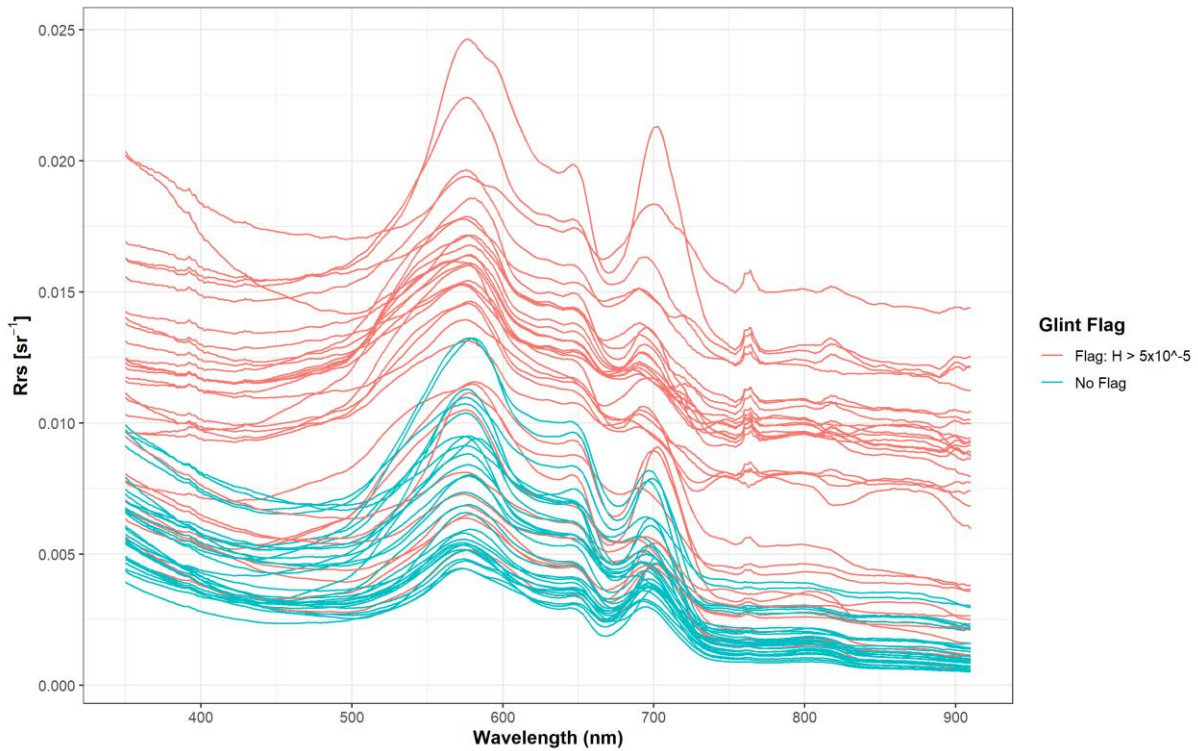
Figure 60: Remote sensing reflectance spectra after the application of the flagging procedure based on the height of the oxygen absorption feature (H), with flagged spectra when H > 5E-05.

c) Satellite Images' Surface Reflectance

During the Fieldwork, there were three occasions when measurements were taken with satellite overpass and mostly clear sky conditions: FC 04, FC 06 and FC 07.

During FC 04 (10/12/21) there was Sentinel-2A MSI sensor overpass and 9 points were sampled (P1 to P9) (Figure 61). On FC 06 (17/12/21) again there was Sentinel-2A MSI sensor overpass and 7 points were sampled (P1 to P7), but due to cloud cover only two points (P4 and P5) were visible in the image (Figure 62). On FC 07 (28/12/21) there was Landsat 8 OLI sensor overpass at the time of measurements and all the 15 points were sampled, but only P7 to P14 were potentially free from cloud contamination by visual inspection (Figure 63).
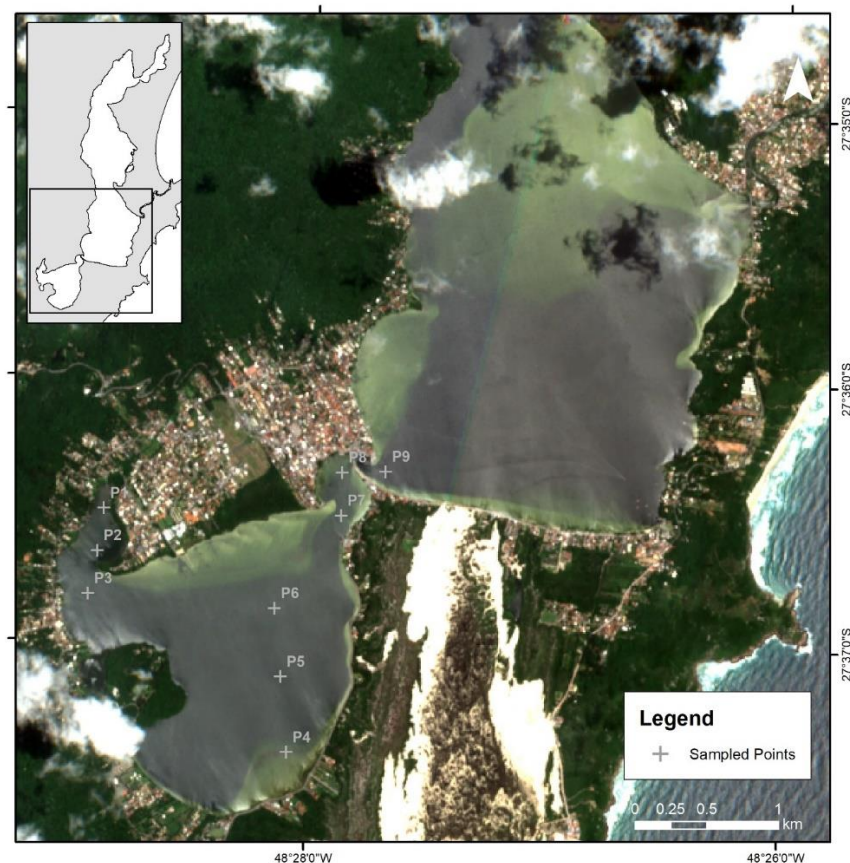
Figure 61: Sentinel-2A MSI RGB image from 10/12/2021 with the location of the points where in-situ radiometric measurements were taken
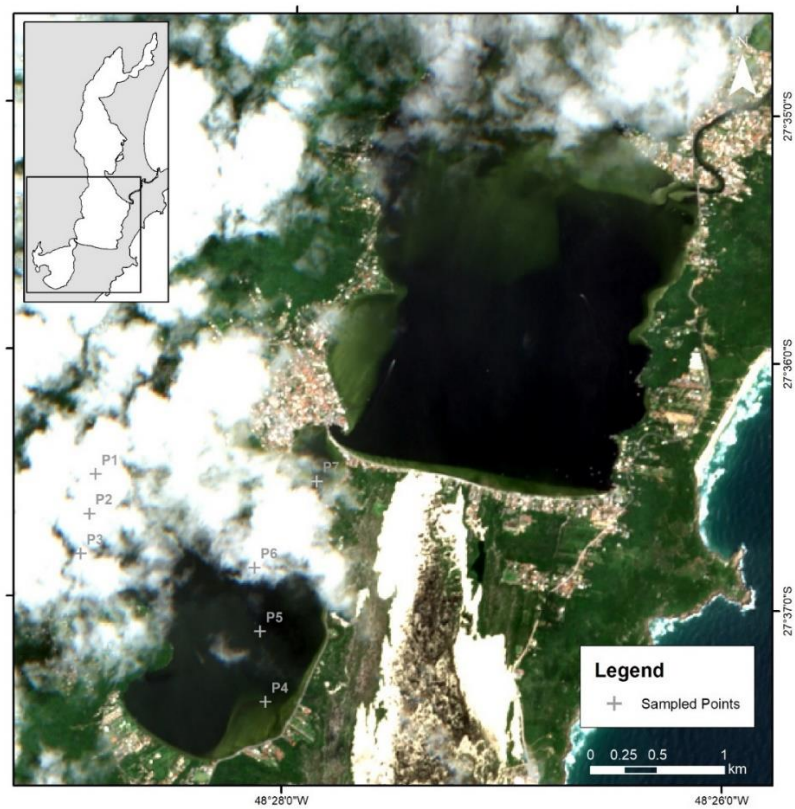
Figure 62: Sentinel-2A MSI RGB image from 17/12/2021 with the location of the points where in-situ radiometric measurements were taken
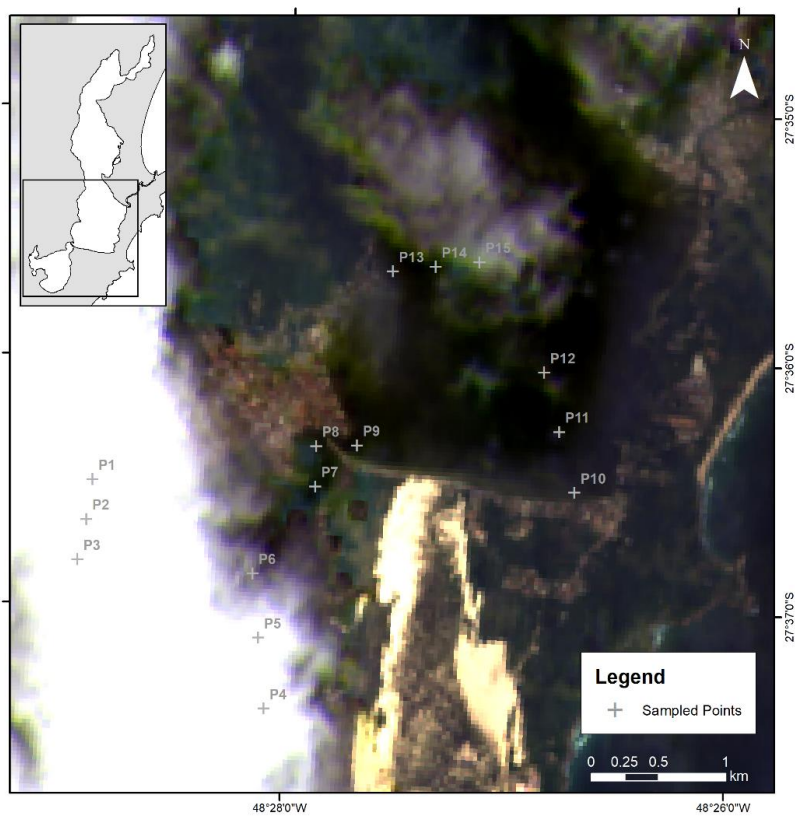
Figure 63: Landsat 8 OLI RGB image from 28/12/2021 with the location of the points where in-situ radiometric measurements were taken

The reflectance values corresponding to the sampling points were extracted from the atmospherically corrected satellite images in Google Earth Engine using the mean value of a 3x3 pixel window.

In order to compare the reflectance measured in-situ with the satellite-derived surface reflectance, it was necessary to convert the hyperspectral into multispectral radiometric data. Spectral convolution based on the satellite's spectral response function (SRF) is the procedure for that, which uses the following equation:

$$\bar{L}(B) = \frac{\int_{\lambda \in B} L(\lambda) S_B(\lambda) d\lambda}{\int_{\lambda \in B} S_B(\lambda) d\lambda} \qquad 23$$

Where $\bar{L}(B)$ is the convolved spectral value at band B, $L(\lambda)$ is the hyperspectral value at wavelength λ and $S_B(\lambda)$ is the SRF value at λ for the band B, with λ taking all the different wavelengths comprised in B.

Although many authors apply convolution directly to the reflectance spectra, Burggraaff (2020) shows that the correct way is to convolve the downwelling irradiance (E_d) and the water-leaving radiance (L_w) separately and then divide them to get the convolved reflectance spectra. As such, the convolution of remote sensing reflectance was calculated as follows:

$$\overline{R_{rs}}(B) = \frac{\bar{L}_w(B)}{\bar{E}_d(B)} = \frac{\int_{\lambda \in B} L_w(\lambda) S_B(\lambda) d\lambda}{\int_{\lambda \in B} E_d(\lambda) S_B(\lambda) d\lambda} \qquad 24$$

Another necessary step to allow comparison between both measurements is the conversion of the remote sensing reflectance (R_{rs}, in sr⁻¹) into water-leaving reflectance (ρ_w, unitless). Assuming an isotropic light field, we have:

$$\rho_w = \frac{\pi \, d^2 L_w}{E_{ext} \cos \theta_s \, t} \qquad 25$$

Where d is the Earth-Sun distance in Astronomic Units (AU), L_w is the water-leaving radiance, E_{ext} is the extraterrestrial solar irradiance at the mean Earth-Sun distance (1 AU), θ_s is the sun zenith angle and t is the atmospheric diffuse transmittance. Since R_{rs} is defined as:

$$R_{rs} = \frac{L_w}{E_d} \qquad 26$$

and the irradiance just above the water (E_d) can be described as:

$$E_d = \frac{E_{ext} \cos \theta_s \, t}{d^2} \qquad 27$$

Substituting 27 in 26 and comparing to 25 it follows that:

$$\rho_w = \pi \, R_{rs} \qquad 28$$

Figure 64 shows the comparison of in-situ measured convolved reflectance and Sentinel-2 A MSI Level 2A surface reflectance (atmospherically corrected using sen2cor) for the 9 points sampled on FC 04 (10/12/21). All of the sampled points had good pixel quality, classified as water in the Scene Classification Map of the product. Comparing both measurements it is possible to observe that they follow a very similar response, but the Sentinel-2 reflectance is systematically higher. It should be noted that in-situ reflectance spectra from points P01, P05 and P06 were flagged as likely glint contaminated in the previous quality control procedure (see Glint Contamination) and P01 and P05 were the measurements with the lowest difference from the S2-SR. For the other points, it is observed a relatively uniform ratio between in-situ and S2 reflectance (Figure 65), which could indicate glint contamination of the satellite imagery or a bias in the atmospheric correction procedure. To investigate the potential bias of the sen2cor algorithm for reflectance retrieval over water, ACOLITE algorithm was applied to the image of this date also, which was designed for water applications (Vanhellemont, 2019). The results show that, although ACOLITE

provides lower reflectance values in the VIS compared to sen2cor, both perform very similarly and have a considerable offset from the in-situ measurements (Figure 66).

Figure 64: Comparison of the Sentinel-2 MSI and in-situ water-leaving reflectance (ρ_w) measured at the sampling points P01 to P09 during FC04 10/12/2021
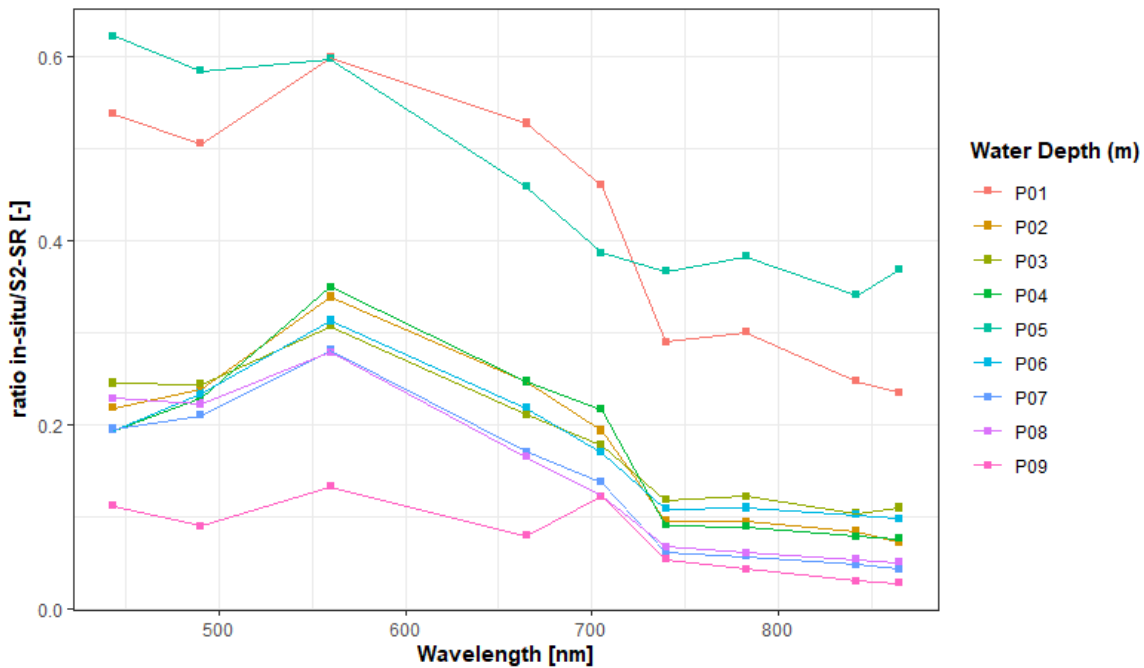
Figure 65: Ratio between in-situ convolved reflectance and Sentinel-2 surface reflectance during FC04 10/12/2021 for sampling points P01 to P09
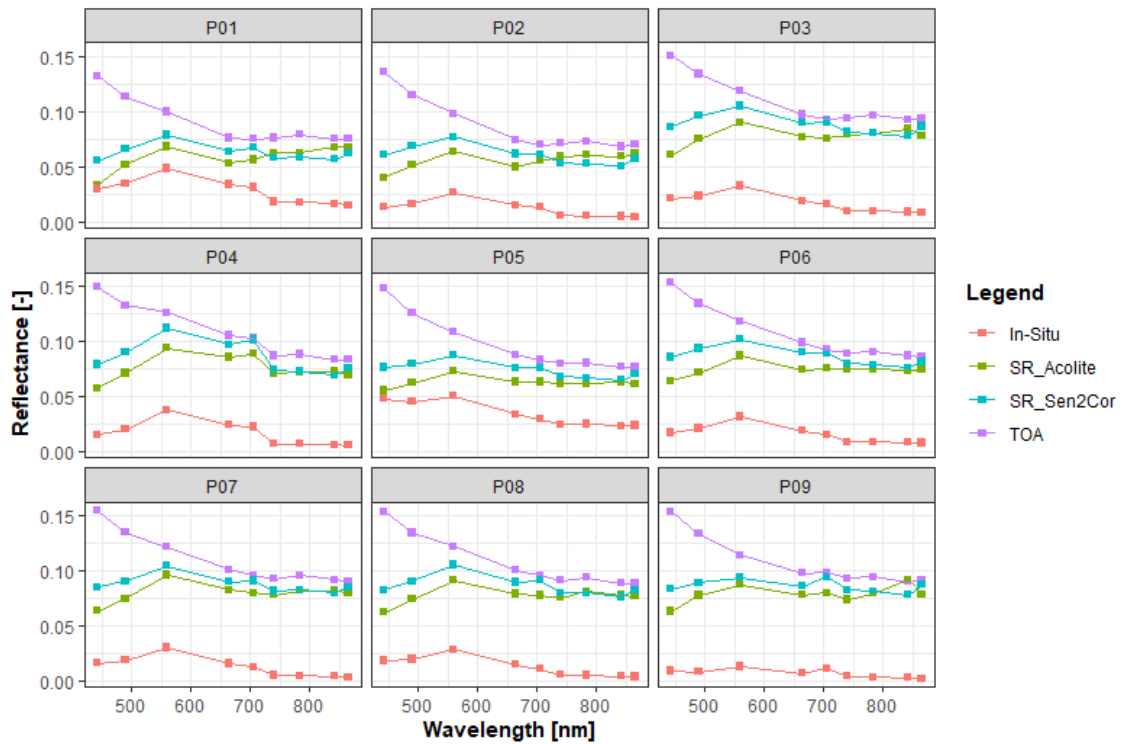
Figure 66: Comparison between in-situ derived reflectance, Sentinel-2 surface reflectance obtained via ACOLITE and sen2cor algorithms and TOA

Figure 67 shows the comparison of in-situ measured and Sentinel-2 A MSI reflectance for points P04 and P05 sampled on FC 06 (17/12/21). The image pixels were classified as of good quality in the product, but the in-situ spectrum from P05 was flagged as potentially glint contaminated. It is possible to observe that the difference between in-situ and satellite measurements is smaller when compared to the results of FC 04 (see the difference in y-axis values). In-situ and satellite reflectance show a very similar pattern, except for Band 1 (443 nm), where satellite data is peaked in comparison to in-situ measured. The satellite reflectance again is systematically higher than in-situ measurements, with the exception of P04 in the NIR, when satellite values are matching the in-situ ones.
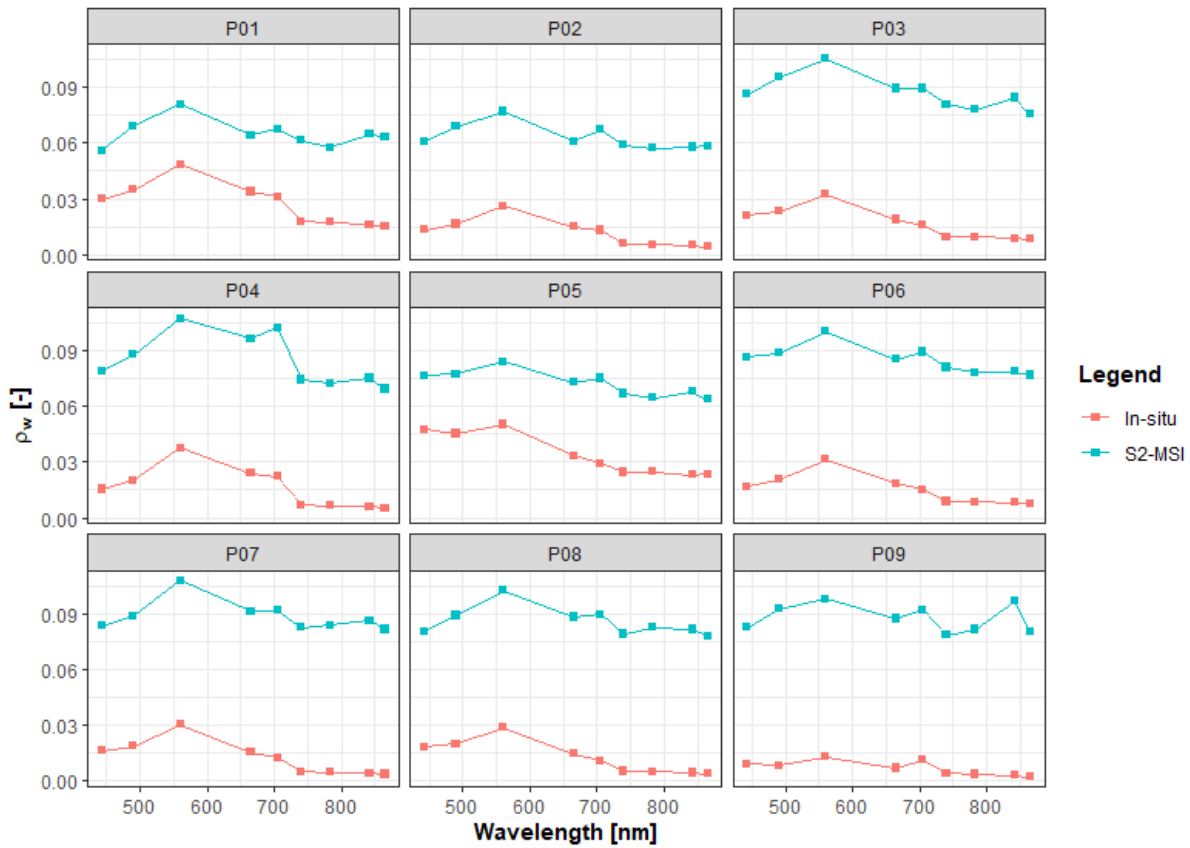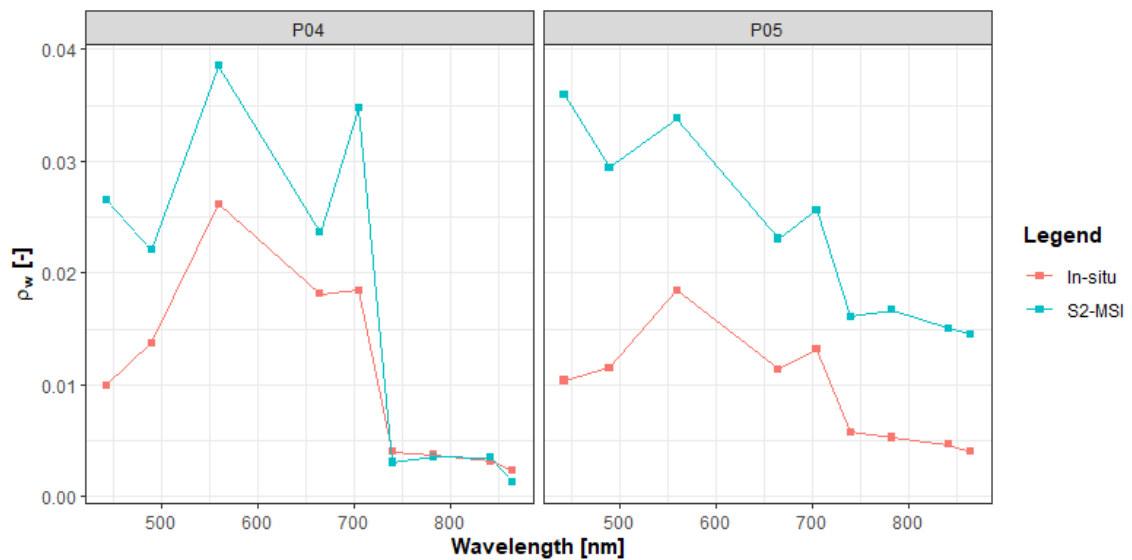

Figure 67: Comparison of the Sentinel-2 MSI and in-situ water-leaving reflectance (ρ_w) measured at the sampling points P04 and P05 on 17/12/2021

For FC 07 (28/12/21), the corresponding Landsat 8 OLI image acquired was not found fit to be compared with the in-situ measurements. The pixel quality band indicates cirrus, high clouds for points P07, P08, P09, P12 and P14, and a combination of dilated cloud and cloud shadow for P10, P11 and P13. The surface reflectance (from LaSRC atmospheric correction algorithm) extracted for the pixels showed negative values for almost all sampling points.

WATER QUALITY DATA

For the water quality data collected during fieldwork, errors could arise from problems in the instruments, their use, sample collection, conservation, or the laboratory analysis itself.

For the CTD measurements (Temperature, Salinity and Depth) the quality control procedure was based on the fieldwork notes. On some occasions, the anchor detached from the substrate and the boat was adrift during the deployment of the instrument. When this happened, a note was made as to the time and point of the erroneous record and it was discarded later. After resettlement, the measurement was repeated under appropriate conditions.

For the CDOM measurements, the range of the values recorded was analyzed to check potential errors. During FC 01, all of the recorded values were below the detection limit of the instrument (0.25 µg/L), which meant they were invalid and therefore discarded. The same happened on FC 02 and FC 04 for the first sampling point of that day (P10 and P1 respectively).

For the measurements that required laboratory analysis (Chlorophyll-a, SPM and Coliforms), uncertainties were added due to the use of two different laboratories. Laboratory QMC (hereby called Lab 1) did the analysis for the first 6 Field Campaigns (in total 52 points), while Aquaplant (Lab 2) analyzed the samples from the last Campaign (15 points). From the boxplots in Figure 68, it is possible to observe that there was a clear discrepancy between the results provided by the two labs, with Lab 2 giving much higher values of SPM and chlorophyll-a concentration. There was no observed change in conditions of the lagoon that could explain such a difference and both laboratories used the same methods for the analysis. Compared to other studies conducted in Conceição Lagoon (de Barros et al., 2017; Horn, 2021), the range of values of Lab 1 seems to represent better the typical conditions observed there. For thermotolerant coliforms, Lab 2 results were all under the detection limit < 10 MPN/100mL, while Lab 1 provided values in the range of 210 to 940 MPN/100mL. In this case, Lab 2 used the enzyme-substrate method, while Lab 1 used multiple tube fermentation. After request, Lab 2 double-checked their procedures and values, but confirmed the result that was provided. It was opted then to not use the data from Lab 2 in the research.
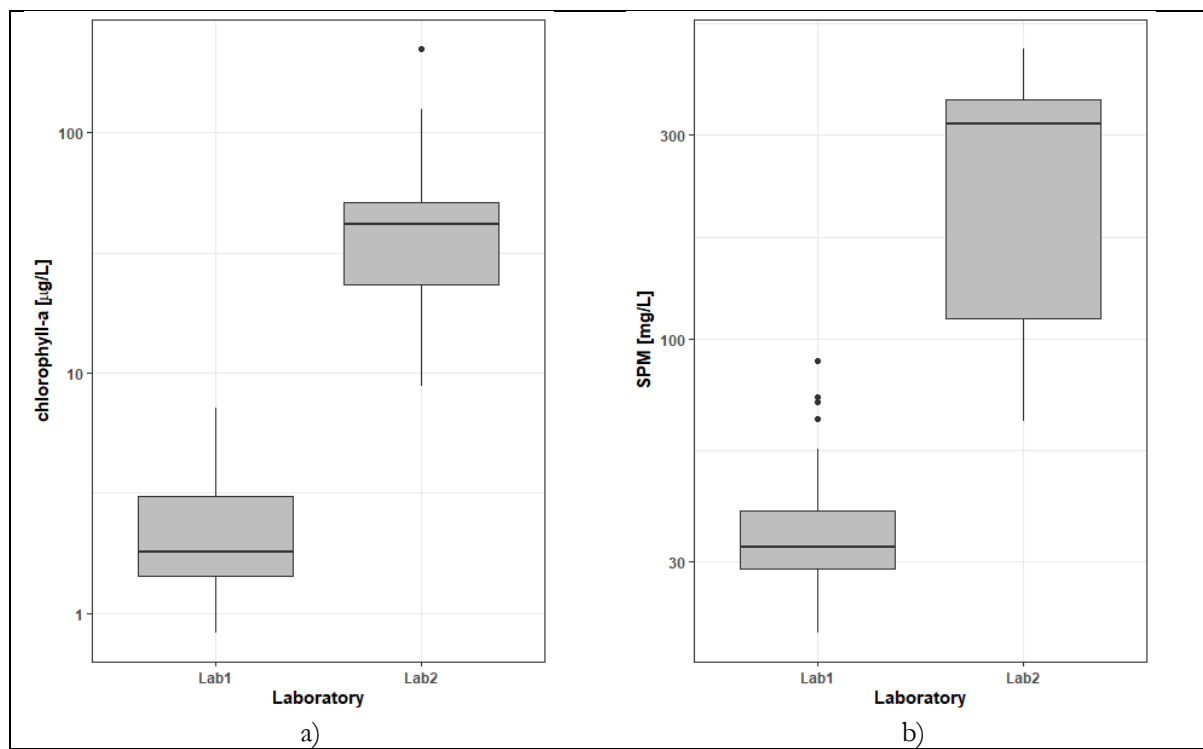
Figure 68: Boxplots of the concentration of a) chlorophyll-a and b) suspended particulate matter (SPM) provided by the different laboratories that conducted the analysis

APPENDIX E– COMPARISON 2SEACOLOR WITH EMPIRICAL INDICES

Due to the lack of correlation observed between the IOPs derived by the 2SeaColor and the water constituents concentration measured in-situ, it was decided to apply other empirical algorithms established in the literature and assess whether they could give better results. Empirical algorithms link apparent optical properties (AOPs) on the satellite level to the concentration of optically active constituents in the water using simultaneously acquired field data and statistical regression methods. Although such algorithms are regional-specific and need to be tuned with local data, the use of band ratios and/or spectral indices has the advantage of minimizing the effects of the atmospheric and illumination conditions (Mishra and Mishra, 2012). Analytical models, such as the 2SeaColor, have the forward model based on the exact solution of RTE and are more sensitive to noise and errors in the atmospheric correction (Sagan et al., 2020).

Considering the regional specificity, it was opted for trying a range of empirical indices for each water constituent, which is summarized in Table 11. Figure 69, Figure 70 and Figure 71 show the scatterplots of concentration measured in-situ against index values for chlorophyll-a, CDOM and SPM respectively. Very low correlation coefficients and high p-values are observed, indicating the lack of correlation. With log transformation (to assess non-linear relationship) still no correlation was found.

Another approach to evaluate the performance of the 2SeaColor was based on the method developed by Loisel et al. (2014) and also applied by Normandin et al. (2019). An inter-comparison is performed between the 2SeaColor-derived IOPs and the empirical indices to verify their agreement. This was conducted for both the in-situ reflectance spectra and for Sentinel-2 image of a day with matched up measurements (2021-12-10).

Figure 72 shows the scatterplot of the absorption by chlorophyll-a derived from 2SeaColor against empirical indices (both applied to the in-situ spectra) and it is possible to observe a high positive linear correlation (R > 0.73) for the indices MPH, NDCI, SLOPE and TwoB. The low p-values indicate that the correlation is statistically significant at a 99% confidence interval. Figure 73 compares the log-transformed values of absorption by CDOM from 2SeaColor against the empirical indices (both applied to the in-situ spectra) and a strong exponential relationship for indices Ficek[5], Mannino and Menken ($|R|>0.54$) are seen. For SPM it is also seen a very good correlation between the log-transformed backscattering from 2SeaColor and the Doxaran, Dsa and Gernez indices applied to the in-situ spectra (R>0.61) (Figure 74).

For the Sentinel-2 image inter-comparison, selected indices were applied considering the availability of bands. For chlorophyll-a, the indices FLH, HP, NDCI, SLOPE and TwoB were applied to the image and compared to the absorption derived from 2SeaColor for pixels that corresponded to the in-situ sampling points (Figure 75). No correlation was observed in this case, as p-values are higher than 0.05. This is influenced by the number of samples (n=9), which reduces statistical significance. Comparing the index values from the image with the chlorophyll-a concentration measured in-situ (Figure 78) it is observed high p-values, which also do not grant statistical significance to the correlation. It should be noted that the quality of the image of this day is not ideal, as clouds are largely present in the North Lagoon and glint contamination also seems to be occurring.

---

[5] Ficek's model suggests negative correlation between the index and absorption by CDOM (Ficek et al., 2011).

For CDOM an inter-comparison is conducted between absorption derived from 2SeaColor and the empirical models BR and Ficek, all applied to the Sentinel-2 image and extracted for the sampling points. As seen in Figure 76, no correlation was found in this case. The same applies to the comparison between CDOM concentration measured in-situ and index values derived from the image (Figure 79).

The comparison of backscattering of SPM derived from 2SeaColor and empirical indices Bernardo, Doxaran, Dsa and Nechad applied to the Sentinel-2 image and extracted for the sampling points is presented in Figure 77. It is possible to observe strong positive correlation between backscattering and the Dsa and Nechad indices in this case, with high coefficient of correlation and a confidence level above 99%. This suggests that the retrieval of $b_{b\,SPM}(440)$ by the 2SeaColor from Sentinel-2 image would be consistent in case of spectra offset caused by errors in the atmospheric correction, though probably would contain an offset as well. Comparing the index values applied to the image with in-situ measured concentration of SPM (Figure 80), no significant correlation is observed. Exception is Nechad index, which gives a significant negative correlation, but only positive correlation is expected for this model.

This procedure revealed no correlation between the in-situ measurements of water constituents concentration (from samples) and the empirical models (refer to Table 11) applied to in-situ spectra and Sentinel-2 image, which supports the hypothesis that the water quality in-situ measurements might not be consistent. A strong agreement between the 2SeaColor derived IOPs and indices from the literature applied to in-situ spectra gives more confidence that the model is working as expected in terms of deriving IOPs from reflectance spectra. The inter-comparison of 2SeaColor derived IOPs and indices applied to a Sentinel-2 image provided lower than expected agreement, but the analysis suggests that the utilized image had potential issues regarding cloud cover and glint contamination.

Table 11: Summary of empirical indices used in the research: their name, formulation, what it is used for and the reference

Index	Acronym	Index Formulation	Estimation of	Reference
Height Peak	HP	$R_{rs}(705) - \left[\dfrac{R_{rs}(665) + R_{rs}(740)}{2}\right]$	Chlorophyll-a	(Toming et al., 2016)
Two Bands	TwoB	$\dfrac{R_{rs}(705)}{R_{rs}(665)}$	Chlorophyll-a	(Dall'Olmo and Gitelson, 2005)
Normalized Difference Chlorophyll Index	NDCI	$\dfrac{R_{rs}(705) - R_{rs}(665)}{R_{rs}(705) + R_{rs}(665)}$	Chlorophyll-a	(Mishra and Mishra, 2012)
Slope	SLOPE	$\dfrac{R_{rs}(705) - R_{rs}(665}{705 - 665}$	Chlorophyll-a	(Mishra and Mishra, 2010)
Fluorescence Line Height	FLH	$R_{rs}(681) - \left[R_{rs}(709) + \dfrac{(709 - 681)}{(709 - 665)} * (R_{rs}(665) - R_{rs}(709)\right]$	Chlorophyll-a	(Letelier and Abbott, 1996)
Maximum Peak Height	MPH	$Max\big(R_{rs}(680 - 750)\big) - R_{rs}(664) - \left[\big((R_{rs}(885) - R_{rs}(664)\big) * \dfrac{\lambda_{max} - 664}{885 - 664}\right]$	Chlorophyll-a	(Matthews et al., 2012)
Blue-Red	BR	$\dfrac{R_{rs}(450)}{R_{rs}(650)}$	CDOM	(Harringmeyer et al., 2021)
Brezonik1	-	$\dfrac{R_{rs}(705)}{R_{rs}(910)}$	CDOM	(Brezonik et al., 2015)
Brezonik2	-	$\dfrac{R_{rs}(490)}{R_{rs}(740)}$	CDOM	(Brezonik et al., 2015)
Menken	-	$\dfrac{R_{rs}(670)}{R_{rs}(560)}$	CDOM	(Menken et al., 2009)
Mannino	-	$\dfrac{R_{rs}(490)}{R_{rs}(555)}$	CDOM	(Mannino et al., 2008)
Ficek	-	$\dfrac{R_{rs}(570)}{R_{rs}(655)}$	CDOM (neg corr.)	(Ficek et al., 2011)
Bernardo	-	$\dfrac{R_{rs}(561)}{R_{rs}(482)}$	SPM	(Bernardo et al., 2020)
Doxaran	-	$\dfrac{R_{rs}(865)}{R_{rs}(555)}$	SPM	(Doxaran et al., 2003)
Dsa	-	$\dfrac{R_{rs}(670)}{R_{rs}(555)}$	SPM	(D'Sa et al., 2007)
Gernez	-	$\dfrac{R_{rs}(865)}{R_{rs}(560)}$	SPM	(Gernez et al., 2014)
Nechad	-	$\dfrac{384.11\pi\, R_{rs}(655)}{1 - \dfrac{\pi\, R_{rs}(655)}{0.1747}} + 1.44$	SPM	(Nechad et al., 2010)

Figure 69: Scatterplots of the concentration of chlorophyll-a measured in-situ against empirical indices derived from in-situ reflectance spectra, with the regression line in black, the confidence interval in grey, the Pearson correlation (R) and the corresponding p-value (p)

Figure 70: Scatterplots of the concentration of CDOM measured in-situ against empirical indices derived from in-situ reflectance spectra, with the regression line in black, the confidence interval in grey, the Pearson correlation (R) and the corresponding p-value (p)
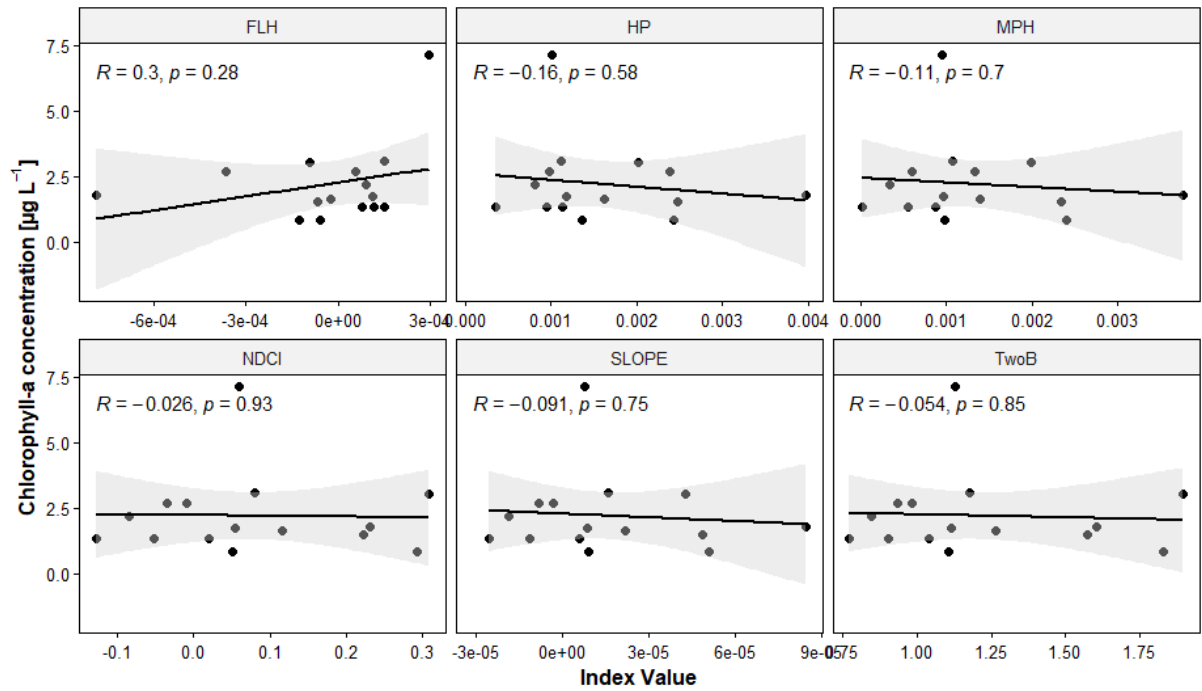
Figure 71: Scatterplots of the concentration of SPM measured in-situ against empirical indices derived from in-situ reflectance spectra, with the regression line in black, the confidence interval in grey, the Pearson correlation (R) and the corresponding p-value (p)
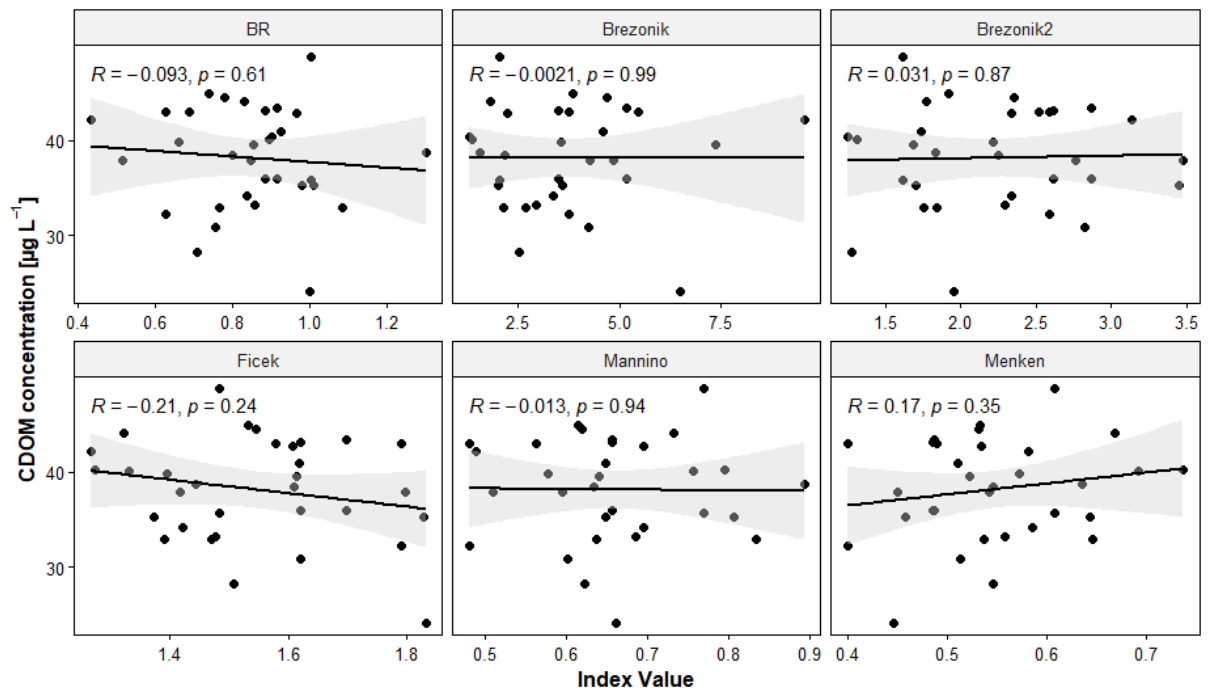

Figure 72: Scatterplots of the absorption by chlorophyll-a derived from 2SeaColor against empirical indices (both applied to the in-situ spectra), with the regression line in black, the confidence interval in grey, the Pearson correlation (R) and the corresponding p-value (p)

Figure 73: Scatterplots of the log of absorption by CDOM derived from 2SeaColor against empirical indices (both applied to the in-situ spectra), with the regression line in black, the confidence interval in grey, the Pearson correlation (R) and the corresponding p-value (p)

Figure 74: Scatterplots of the log of backscattering derived from 2SeaColor against empirical indices (both applied to the in-situ spectra), with the regression line in black, the confidence interval in grey, the Pearson correlation (R) and the corresponding p-value (p)

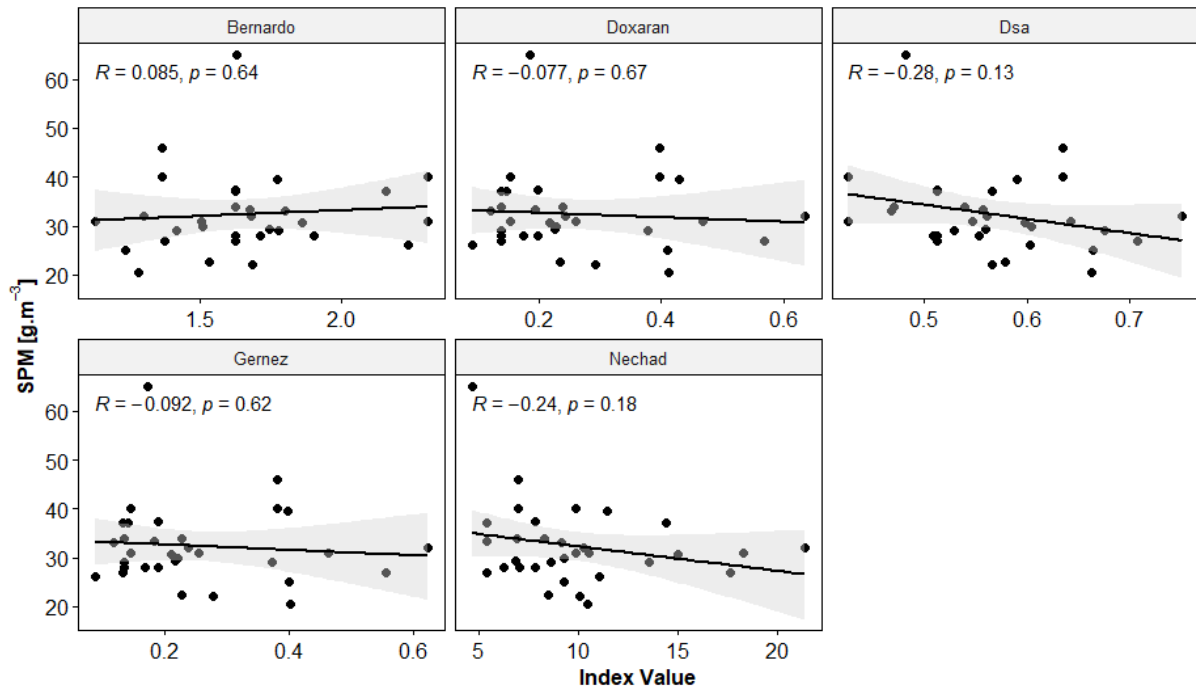Figure 75: Scatterplots of the absorption by chlorophyll-a derived from 2SeaColor against empirical indices (both applied to Sentinel-2 image of 2021-12-10 and extracted for the sampling points), with the regression line in black, the confidence interval in grey, the Pearson correlation (R) and the corresponding p-value (p)
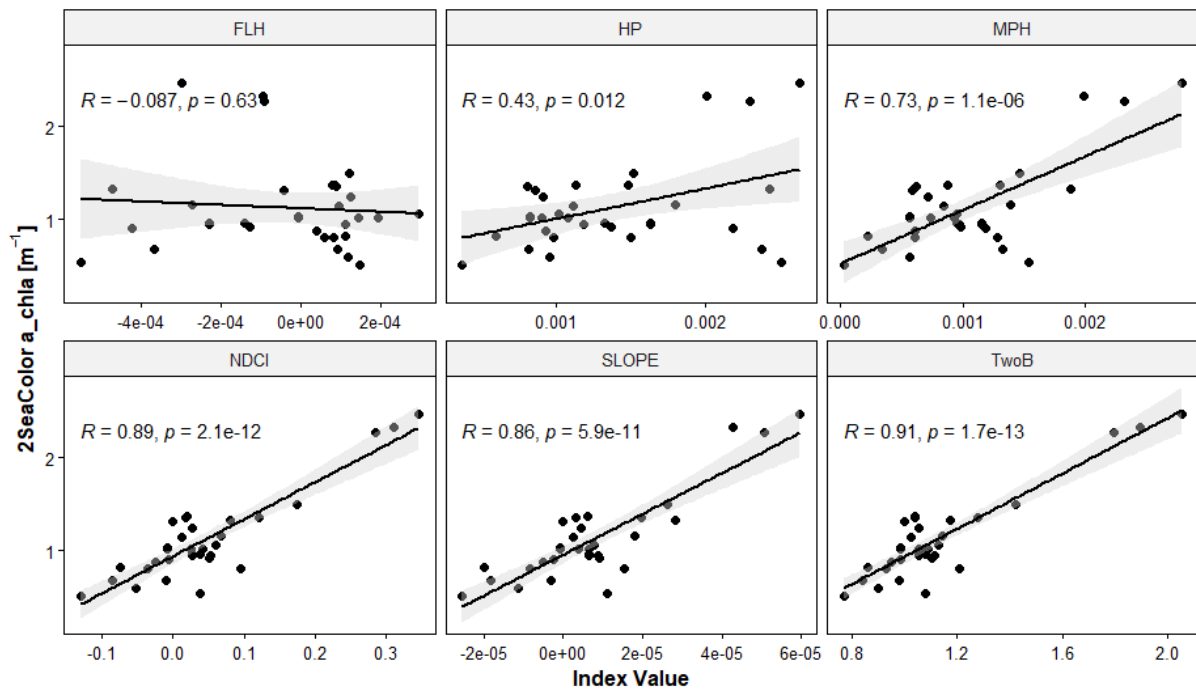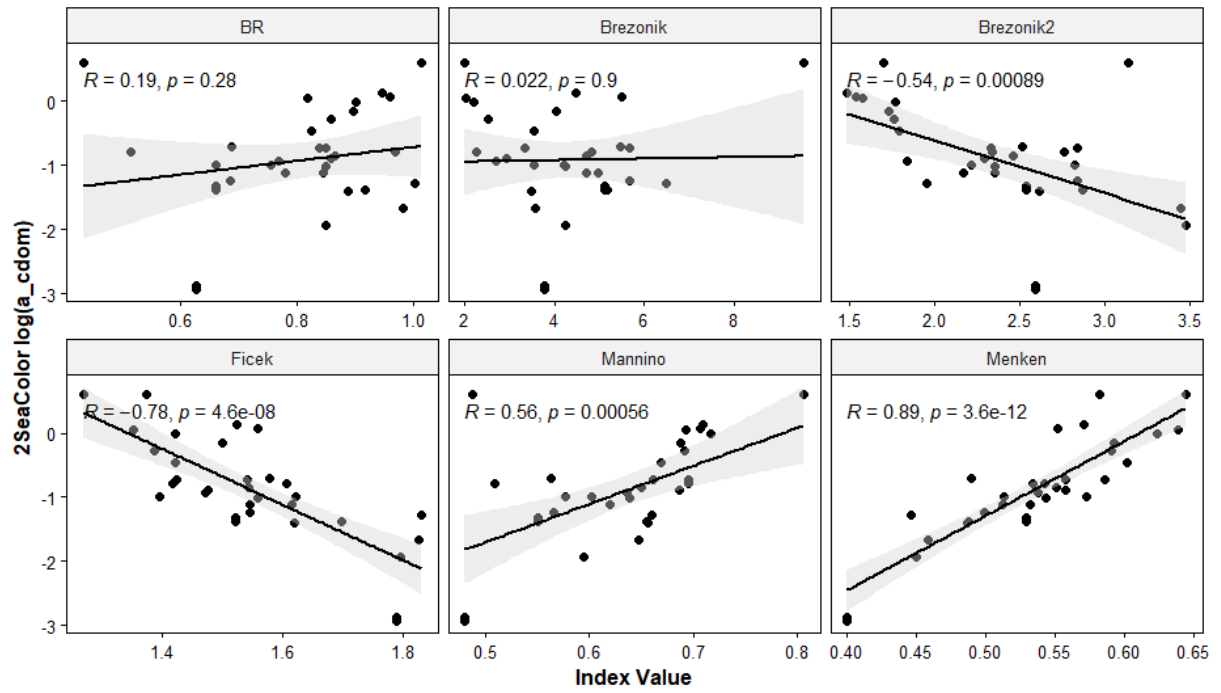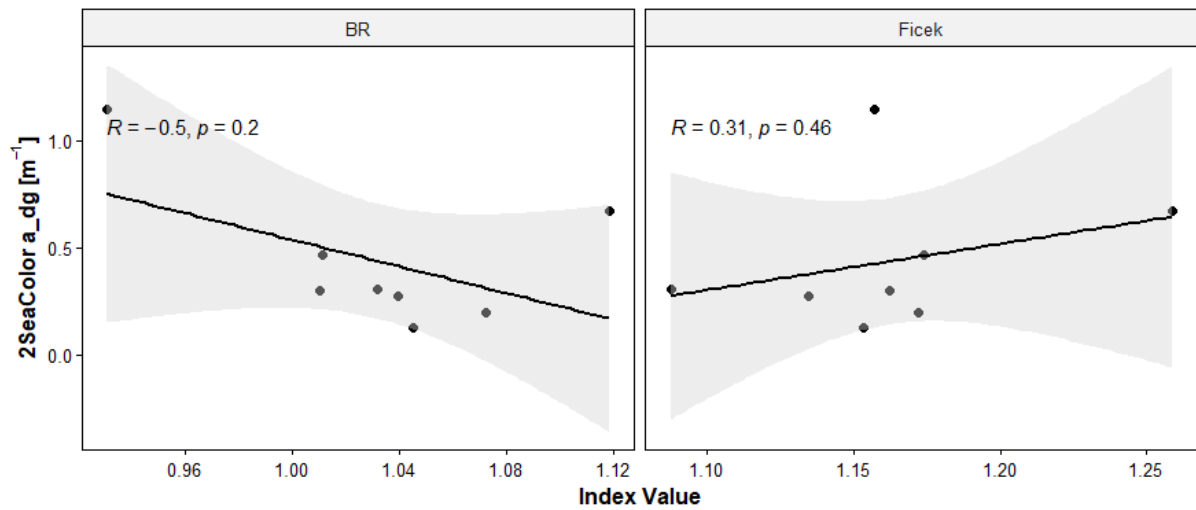

Figure 76: Scatterplots of the absorption by detritus and CDOM derived from 2SeaColor against empirical indices (both applied to Sentinel-2 image of 2021-12-10 and extracted for the sampling points), with the regression line in black, the confidence interval in grey, the Pearson correlation (R) and the corresponding p-value (p)
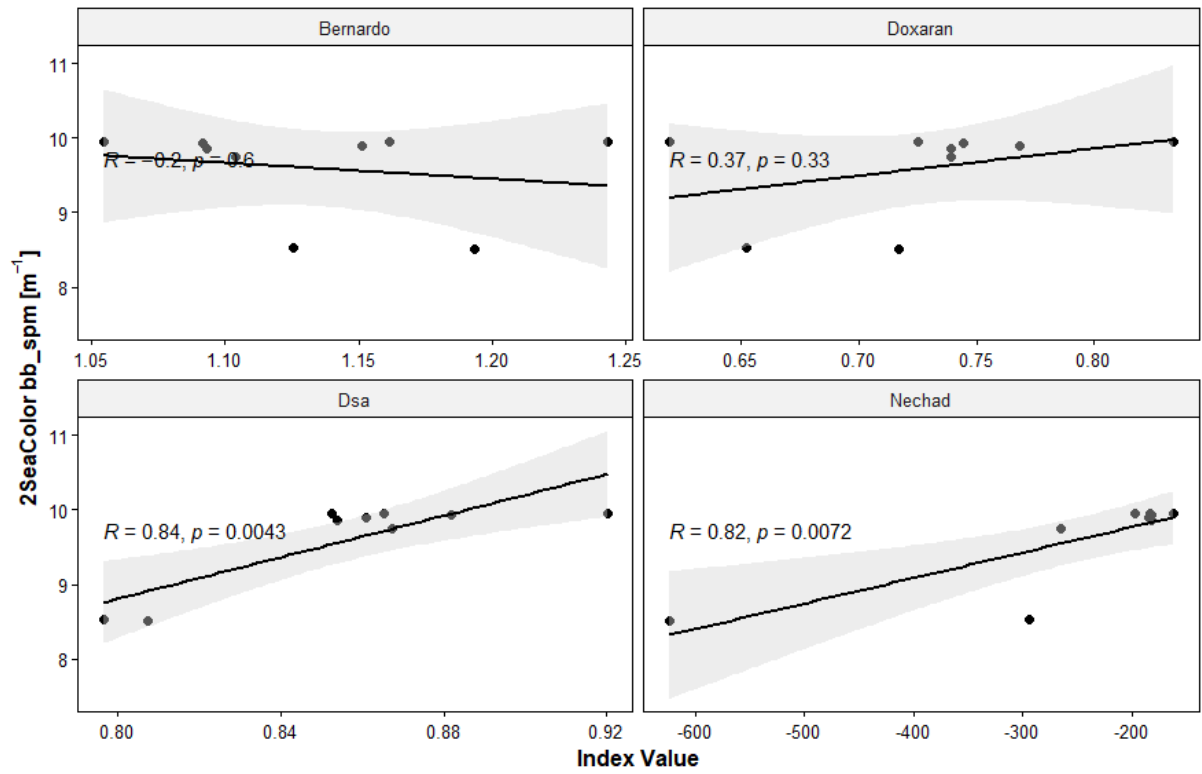
Figure 77: Scatterplots of the backscattering by SPM derived from 2SeaColor against empirical indices (both applied to Sentinel-2 image of 2021-12-10 and extracted for the sampling points), with the regression line in black, the confidence interval in grey, the Pearson correlation (R) and the corresponding p-value (p)
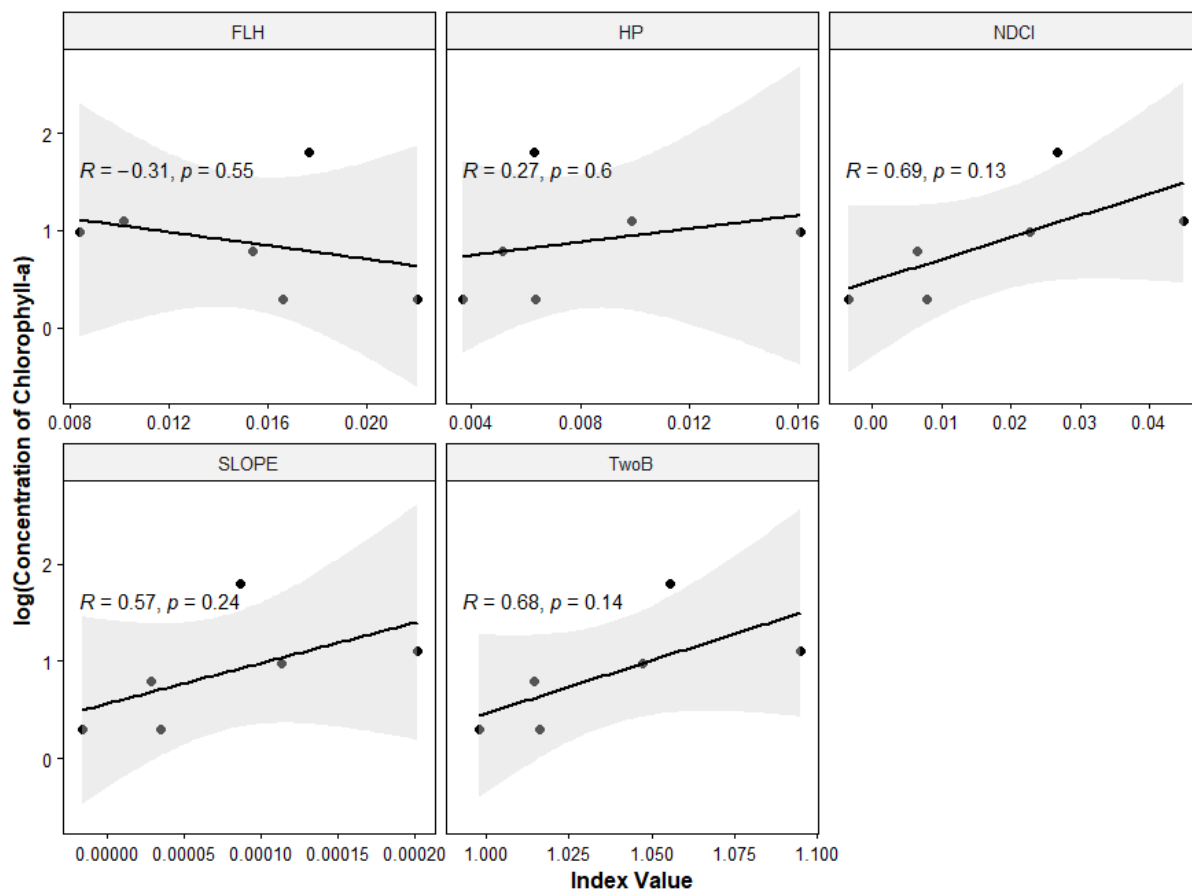
Figure 78: Scatterplots of the concentration of chlorophyll-a measured in-situ against empirical indices derived from Sentinel-2 Image, with the regression line in black, the confidence interval in grey, the Pearson correlation (R) and the corresponding p-value (p)
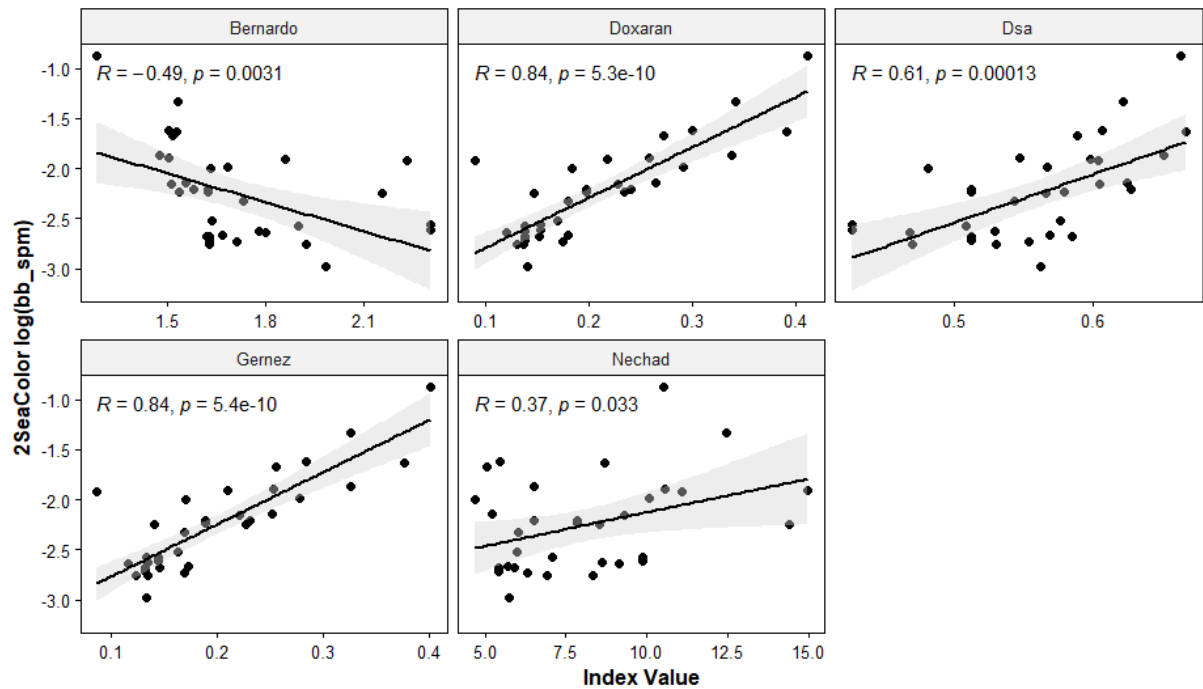

Figure 79: Scatterplots of the concentration of CDOM measured in-situ against empirical indices derived from Sentinel-2 Image, with the regression line in black, the confidence interval in grey, the Pearson correlation (R) and the corresponding p-value (p)
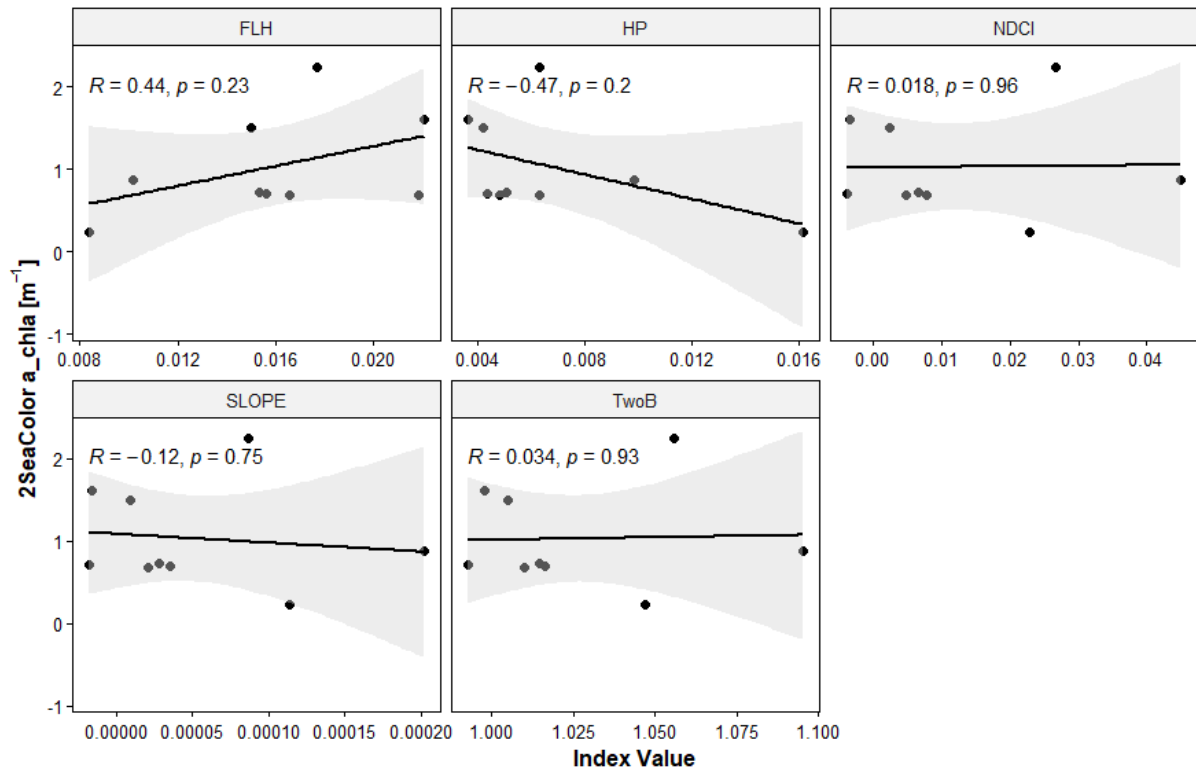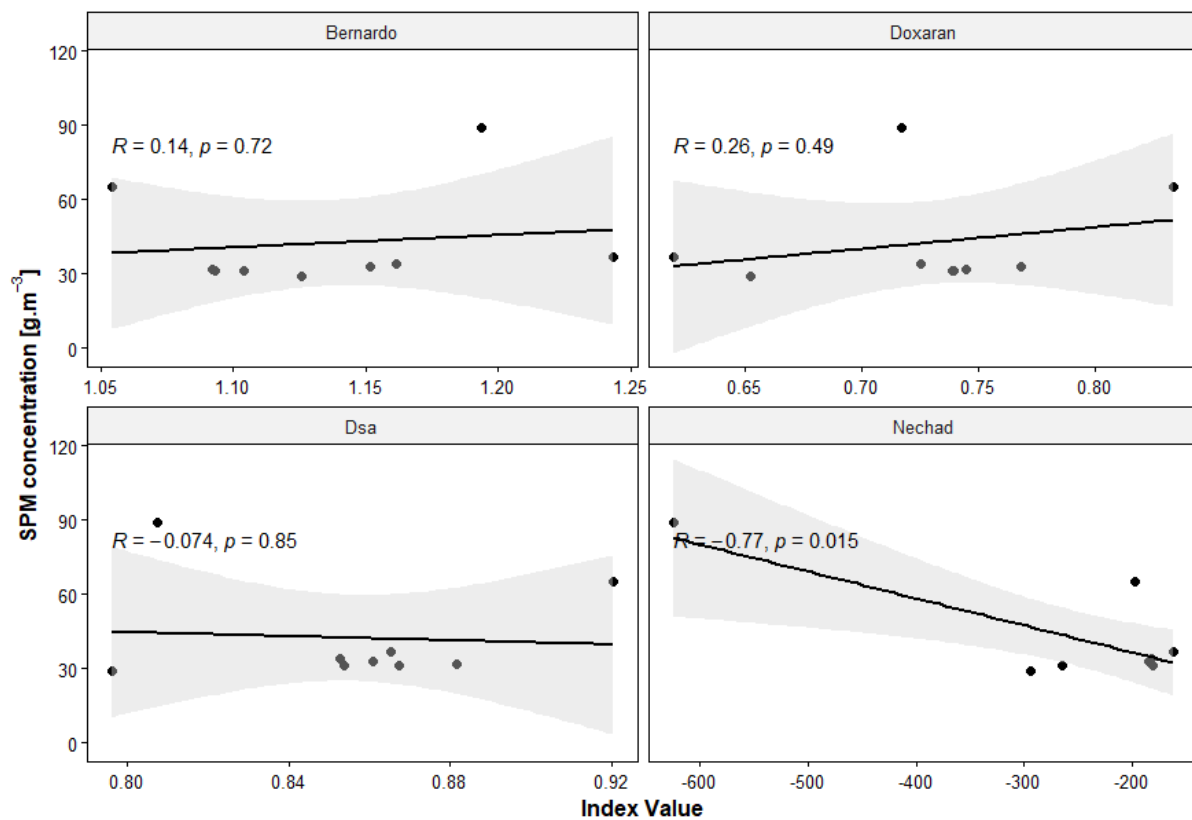
Figure 80: Scatterplots of the concentration of SPM measured in-situ against empirical indices derived from Sentinel-2 Image, with the regression line in black, the confidence interval in grey, the Pearson correlation (R) and the corresponding p-value (p)

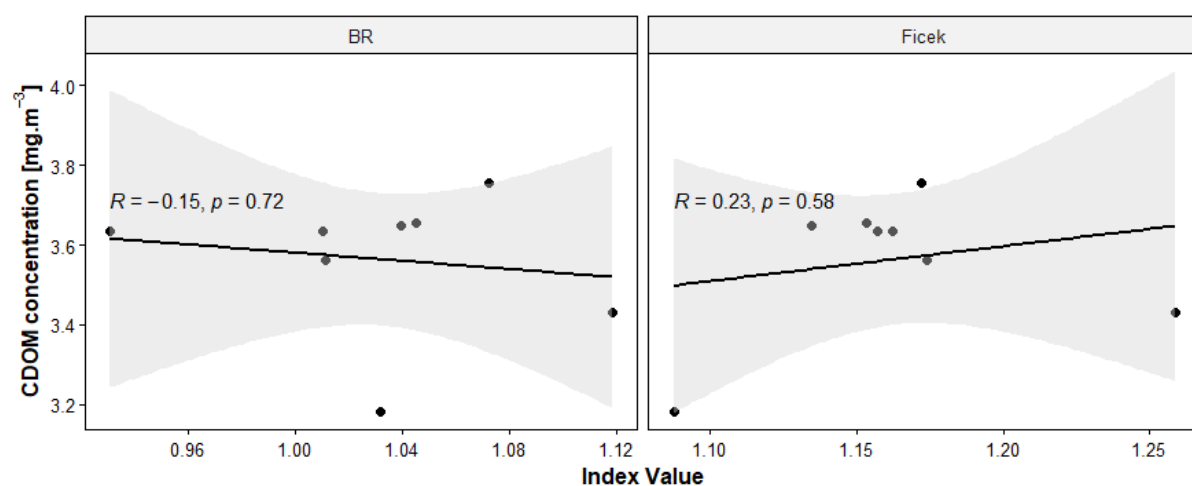## APPENDIX F– COMPILATION OF METEOROLOGICAL DATA

Meteorological data coinciding with dates of images in the time series.

Date	5-Days Accumulated Precipitation [mm]	Wind Direction* [deg]	Average Wind Speed* [m/s]
02/01/2019	0.4	348	3.2
10/01/2019	8	21	2.6
17/01/2019	54.6	147	1.3
30/01/2019	5	21	1.7
01/02/2019	0	92	0
09/02/2019	3.8	318	1.8
24/02/2019	5.2	40	1.8
01/03/2019	37.8	130	1.6
03/03/2019	3.2	134	1.5
06/03/2019	0.4	5	2.1
23/03/2019	11.2	291	2.4
12/04/2019	47.2	357	2.4
15/04/2019	1.2	143	1
17/04/2019	22.4	264	3.8
30/04/2019	9.2	334	2
02/05/2019	5.6	22	1.2
05/05/2019	0.2	349	2.5
04/06/2019	112.2	283	0.6
19/06/2019	0.4	23	1.6
21/06/2019	0.4	299	1.8
04/07/2019	19.8	181	2
06/07/2019	19.8	315	0.3
11/07/2019	0.4	134	0.4
16/07/2019	15.2	207	1.9
29/07/2019	6.6	8	1.6
03/08/2019	2.2	261	0.8
05/08/2019	2.2	256	0.7
13/08/2019	0	165	4.4
23/08/2019	11.6	16	1.3
30/08/2019	1.4	359	4.2
22/09/2019	35.2	137	1.3
27/09/2019	0	154	5.3
09/10/2019	10.4	146	1.7
22/10/2019	0.8	165	1.3
24/10/2019	0	358	2.2
16/11/2019	NA	121	2.1
18/11/2019	NA	32	2.5
03/12/2019	0.8	27	2.6
06/12/2019	38.2	147	1.9
08/12/2019	37.4	32	2.2

Date	5-Days Accumulated Precipitation [mm]	Wind Direction* [deg]	Average Wind Speed* [m/s]
26/12/2019	5	18	2.8
28/12/2019	0	32	3.1
15/01/2020	31	9	3.7
25/01/2020	50	49	1.3
01/02/2020	15.8	149	2.1
11/02/2020	83.2	163	2.7
24/02/2020	1.8	11	2.4
29/02/2020	29	156	1.9
10/03/2020	0	42	2
12/03/2020	0	320	2.6
15/03/2020	0.4	316	2.6
20/03/2020	6.8	149	4.3
22/03/2020	3.8	254	0.6
27/03/2020	6.4	205	0.6
21/04/2020	0	343	2.6
24/04/2020	0	343	2.5
26/04/2020	0.2	160	1.5
04/05/2020	0	317	1.8
09/05/2020	2.8	356	1.9
11/05/2020	2.2	359	3.4
16/05/2020	6.2	142	1
19/05/2020	3.6	165	0.3
24/05/2020	5	282	2.4
26/05/2020	4.8	175	0.9
29/05/2020	0	2	1.8
31/05/2020	0.2	115	1.1
03/06/2020	1.4	118	1.2
08/06/2020	66	147	1.2
20/06/2020	5.6	6	1.9
03/07/2020	23.2	208	0.9
10/07/2020	28.6	22	0.9
15/07/2020	34.6	168	1.1
20/07/2020	16.2	5	2.1
23/07/2020	0.2	15	0.4
02/08/2020	15.2	358	2
04/08/2020	1.2	4	2.1
07/08/2020	0.4	332	1.1
09/08/2020	0.4	43	1
22/08/2020	22.4	124	1.2
24/08/2020	5.4	112	1.6
27/08/2020	2	357	3.3
11/09/2020	101.2	11	2.3
18/09/2020	11	146	1.6
01/10/2020	23.4	29	1.6

Date	5-Days Accumulated Precipitation [mm]	Wind Direction* [deg]	Average Wind Speed* [m/s]
11/10/2020	9.2	13	1.4
21/10/2020	2	168	2.4
28/10/2020	47.4	144	1.6
07/11/2020	7.6	133	2
17/11/2020	20.6	156	4
20/11/2020	17	153	1.5
30/12/2020	51	32	2.1
04/01/2021	0.6	343	2.3
06/01/2021	1	2	2.6
09/01/2021	28.4	274	1.2
11/01/2021	31.4	5	2.9
31/01/2021	45.8	307	2.3
03/02/2021	66.8	25	2.5
05/02/2021	43.4	335	1.6
08/02/2021	8.6	147	2.5
27/03/2021	14.2	131	0.8
30/03/2021	12.8	137	1.1
04/04/2021	0.6	233	1.1
09/04/2021	23.4	346	2.6
24/04/2021	50.6	142	0.9
26/04/2021	40.6	130	1.1
29/04/2021	3.4	150	1
26/05/2021	21.8	110	0.9
29/05/2021	0.4	292	0
03/06/2021	25.8	166	0.9
13/06/2021	121.2	123	0.5
15/06/2021	44.6	146	0.9
25/06/2021	14	204	0.7
30/06/2021	15.4	42	0.5
03/07/2021	15.6	147	0.6
08/07/2021	10.2	170	1.4
10/07/2021	10	21	0.8
13/07/2021	0.2	13	1.5
18/07/2021	3.8	286	4.1
20/07/2021	3.8	203	0.4
23/07/2021	0	5	2.9
25/07/2021	0.2	11	2
28/07/2021	7.8	322	0.9
30/07/2021	7.6	185	0.6
02/08/2021	0.4	153	2.1
04/08/2021	1	200	1.3
17/08/2021	10.8	360	2.7
19/08/2021	8.8	3	1.8
24/08/2021	0.2	10	2.1

Date	5-Days Accumulated Precipitation [mm]	Wind Direction* [deg]	Average Wind Speed* [m/s]
26/09/2021	0.8	38	1.5
02/11/2021	99.6	37	1.7
22/11/2021	69	15	1.6
27/11/2021	17.2	147	1.5
30/11/2021	20.4	160	1.9
10/12/2021	42.8	131	2.3
17/12/2021	15	143	3.5
20/12/2021	10.6	352	2.6
22/12/2021	1.6	157	2.9
25/12/2021	0.4	26	2.3
27/12/2021	0.2	166	1.7

* Wind speed and direction values correspond to the time of satellite overpass (approx.. 1300 UTC)